



IntechOpen

Residual Stress Analysis on Welded Joints by Means of Numerical Simulation and Experiments

Edited by Paolo Ferro and Filippo Berto



RESIDUAL STRESS ANALYSIS ON WELDED JOINTS BY MEANS OF NUMERICAL SIMULATION AND EXPERIMENTS

Edited by **Paolo Ferro** and **Filippo Berto**

Residual Stress Analysis on Welded Joints by Means of Numerical Simulation and Experiments

<http://dx.doi.org/10.5772/intechopen.69093>

Edited by Paolo Ferro and Filippo Berto

Contributors

Jon Ander Esnaola, Ibai Ulacia, Arkaitz Lopez-Jauregi, Done Ugarte, Ayhan Ince, Lanqing Tang, Jing Zheng, Roberto Montanari, Giuseppe Barbieri, Alessandra Fava, Majid Farajian, Kimiya Hemmesi, Giovanni Meneghetti, Marco Colussi, Paolo Ferro, Filippo Berto, Shiyun Dong, Yong-Jian Li, Xiang-Yi Feng, Chao-Qun Song, Shi-Xing Yan, Caterina Casavola, Alberto Cazzato, Vincenzo Moramarco

© The Editor(s) and the Author(s) 2018

The rights of the editor(s) and the author(s) have been asserted in accordance with the Copyright, Designs and Patents Act 1988. All rights to the book as a whole are reserved by INTECHOPEN LIMITED. The book as a whole (compilation) cannot be reproduced, distributed or used for commercial or non-commercial purposes without INTECHOPEN LIMITED's written permission. Enquiries concerning the use of the book should be directed to INTECHOPEN LIMITED rights and permissions department (permissions@intechopen.com).

Violations are liable to prosecution under the governing Copyright Law.



Individual chapters of this publication are distributed under the terms of the Creative Commons Attribution 3.0 Unported License which permits commercial use, distribution and reproduction of the individual chapters, provided the original author(s) and source publication are appropriately acknowledged. If so indicated, certain images may not be included under the Creative Commons license. In such cases users will need to obtain permission from the license holder to reproduce the material. More details and guidelines concerning content reuse and adaptation can be found at <http://www.intechopen.com/copyright-policy.html>.

Notice

Statements and opinions expressed in the chapters are those of the individual contributors and not necessarily those of the editors or publisher. No responsibility is accepted for the accuracy of information contained in the published chapters. The publisher assumes no responsibility for any damage or injury to persons or property arising out of the use of any materials, instructions, methods or ideas contained in the book.

First published in London, United Kingdom, 2018 by IntechOpen

eBook (PDF) Published by IntechOpen, 2019

IntechOpen is the global imprint of INTECHOPEN LIMITED, registered in England and Wales, registration number: 11086078, The Shard, 25th floor, 32 London Bridge Street

London, SE19SG – United Kingdom

Printed in Croatia

British Library Cataloguing-in-Publication Data

A catalogue record for this book is available from the British Library

Additional hard and PDF copies can be obtained from orders@intechopen.com

Residual Stress Analysis on Welded Joints by Means of Numerical Simulation and Experiments

Edited by Paolo Ferro and Filippo Berto

p. cm.

Print ISBN 978-1-78923-106-9

Online ISBN 978-1-78923-107-6

eBook (PDF) ISBN 978-1-83881-373-4

We are IntechOpen, the first native scientific publisher of Open Access books

3,450+

Open access books available

110,000+

International authors and editors

115M+

Downloads

151

Countries delivered to

Our authors are among the
Top 1%

most cited scientists

12.2%

Contributors from top 500 universities



WEB OF SCIENCE™

Selection of our books indexed in the Book Citation Index
in Web of Science™ Core Collection (BKCI)

Interested in publishing with us?
Contact book.department@intechopen.com

Numbers displayed above are based on latest data collected.
For more information visit www.intechopen.com



Meet the editors



Dr. Paolo Ferro is an Associate Professor of Metallurgy and Materials Selection at the University of Padua (Italy). He was a scientific director of the research program 'Numerical and Experimental Determination of Residual Stresses in Welded Joints and their Influence on Fatigue Strength'. He won the prize for young researchers 'Aldo Daccò' in 2002. He is a member of the Centre for Mechanics of Biological Materials and the coordinator of the European project on Critical Raw Materials named DERMAT. His research is mainly focused on the analytical and numerical modelling of metallurgical processes. He is the author of more than 130 papers. In addition to his editorial role in different journals, he frequently serves as a reviewer to many other international journals and national as well as international funding agencies.



Dr. Filippo Berto is the Chair of Mechanics and Materials at the Norwegian University of Science and Technology, Trondheim. He is the author of more than 500 technical papers, mainly oriented to materials science engineering, the brittle failure of different materials, the notch effect, the application of the finite element method to the structural analysis, the mechanical behaviour of metallic materials, the fatigue performance of notched components as well as the reliability of welded, bolted and bonded joints. Since 2003, he has been working on different aspects of the structural integrity discipline, by mainly focusing his attention on problems related to the static and fatigue assessment of engineering materials and components. In particular, he has attempted to devise engineering methods suitable for designing components (experiencing different kinds of stress concentration phenomena) against fatigue as well as against static failures.

Contents

Preface XI

- Chapter 1 **Experimental Techniques to Investigate Residual Stress in Joints 1**
Roberto Montanari, Alessandra Fava and Giuseppe Barbieri
- Chapter 2 **Numerical Welding Simulation as a Basis for Structural Integrity Assessment of Structures: Microstructure and Residual Stresses 29**
Kimiya Hemmesi and Majid Farajian
- Chapter 3 **Residual Stress Analysis of Laser Remanufacturing 49**
Shi-yun Dong, Chao-qun Song, Xiang-yi Feng, Yong-jian Li and Shi-xing Yan
- Chapter 4 **Residual Stress in Friction Stir Welding and Laser-Assisted Friction Stir Welding by Numerical Simulation and Experiments 71**
Caterina Casavola, Alberto Cazzato and Vincenzo Moramarco
- Chapter 5 **Residual Stress Pattern Prediction in Spray Transfer Multipass Welding by Means of Numerical Simulation 91**
Jon Ander Esnaola, Ibai Ulacia, Arkaitz Lopez-Jauregi and Done Ugarte
- Chapter 6 **Numerical Simulation of Residual Stresses in Welding and Ultrasonic Impact Treatment Process 121**
Lanqing Tang, Ayhan Ince and Jing Zheng
- Chapter 7 **Rapid Calculation of Residual Notch Stress Intensity Factors (R-NSIFs) by Means of the Peak Stress Method 137**
Marco Colussi, Paolo Ferro, Filippo Berto and Giovanni Meneghetti

Preface

There is a need for designers and engineers to quantify the residual stresses induced by welding processes as it is the primary joining technique used in the fabrication of civil structures and mechanical engineering assemblies. Information on residual stresses is important because of the complexity of predicting distortions of welded structures during assembly, and in the context of a necessity to improve the efficiency and reliability of fatigue life assessment of structures and structural components. The ability to quantify residual stresses induced by welding processes through experimentation or numerical simulation has today become, more than ever, of strategic importance in the context of improved efficiency and more accurate design. This is an ongoing challenge that started many years ago and has benefited greatly in recent years from the development of high speed computing and advanced experimental techniques. Modern design criteria do, in fact, include the effect of residual stresses on the fatigue strength of welded joints, thus allowing a more efficient use of materials and a greater reliability of welded structures. The key issue, however, is accurate assessment of the residual stress field. This is the reason why extensive effort has been dedicated to improving experimental and numerical strategies used to assess residual stresses in structural components. Experimental techniques are highly valuable because they allow validation of numerical models. However, from the perspective of structural design, experimental techniques are of less relevance than numerical methods, because they are usually employed once a structure is welded, are expensive and provide limited information related to a discrete number of points in the joint. On the other hand, numerical models allow the complete residual stress field to be modelled and hot spot stresses to be assessed. The drawback in using numerical analysis is the complexity and time required because of the implicit transient and non-linear nature of welding processes. For this reason, their use is still scarce in industrial applications in which the design time is a strong limitation. The main challenge is then to develop new, reliable and less time-consuming numerical methods aimed at improving the quality and the efficiency in determining accurately the residual stress field in real structures and components.

In the light of this challenging and complex scenario, the present book aims to discuss, in the form of a collection of case-studies, recent developments and trends in standard and advanced experimental and numerical techniques that can be employed to capture the residual stress field in welded connections. After a comprehensive overview of the main experimental techniques that are usually employed nowadays, numerical methods are then considered in detail. In particular, methods for simulating welding processes with particular attention to the modelling of heat sources and reliable stress-strain constitutive laws in the weld zone are discussed and addressed. The case studies presented deal with different welding techniques including friction stir welding, laser assisted friction stir welding, laser remanufactur-

ing and multi-pass welding. Finally, numerical strategies to identify and quantify residual stress fields are presented and discussed. The overall aim of the book is to assist in providing the background and tools to an efficient and effective advanced design of welded joints.

As Guest Editors of this volume, we believe that the present book fulfils this role and hope that it will be useful to researchers, designers and colleagues who are involved in different aspects of design and investigation of weldments. We would like to thank all the authors for their valuable contributions to this special issue. In addition, we would like to thank the reviewers for their efforts for ensuring the high quality standards for each contribution.

Prof. Paolo Ferro
University of Padova
Vicenza, Italy

Prof. Filippo Berto
Norwegian University of Science and Technology
Trondheim, Norway

Experimental Techniques to Investigate Residual Stress in Joints

Roberto Montanari, Alessandra Fava and
Giuseppe Barbieri

Additional information is available at the end of the chapter

<http://dx.doi.org/10.5772/intechopen.71564>

Abstract

Residual stress arising from welding processes is matter of great concern in industrial practice since it can affect geometry, mechanical behavior and corrosion resistance of components. In order to evaluate residual stress in welded joints and optimize post-welding heat treatments, a lot of work has been devoted to the improvement of measurement methods with increasing sensitivity and accuracy. The chapter presents and discusses some of the experimental techniques commonly used today to determine residual stress in welds and describes recent results and advancements. Destructive (sectioning, contour, hole-drilling, instrumented indentation) and nondestructive (Barkhausen noise, ultrasonic, X-ray and neutron diffraction) methods are illustrated to highlight the specific characteristics, advantages and drawbacks.

Keywords: residual stress, welding, sectioning method, contour method, hole-drilling method, instrumented indentation method, Barkhausen noise method, ultrasonic method, X-ray and neutron diffraction

1. Introduction

In order to satisfy scientific and industrial needs, a lot of work has been devoted to investigate the state of residual stress in metallic materials and its effects on mechanical properties. A number of comprehensive reviews on the topic can be found in the literature (e.g. see [1–8]).

It is well known that residual stress superimposes to external applied stress and plays a crucial role in the failure of components and structures; therefore, it is taken into account in advanced design in the aerospace, automotive and nuclear fields. All manufacturing processes modify the state of stress with either positive or negative consequences; for instance, compressive surface stress increases the fatigue limit, whereas tensile residual stress may decrease the corrosion resistance.

Welding may produce huge effects on the metals: when two pieces of plates or pipes are joined together, temperature ranges from the melting point of the material to room temperature and localized high residual stress coupled with shrinkage is generated near the weld seam. After cooling to room temperature, the locked-in stress is retained leading to distortion and/or buckling. The quantitative measurement of residual stress in welded joints is of the utmost importance for the safe operation of power plants, petrochemical plants, storage tanks and transmission pipelines.

To control such effects, it is necessary to predict the macroscopic transient fields of temperature, strain and stress. In principle, this can be done by solving the equations of continuum mechanics; however, a rigorous analysis of welds is a challenging task. At the macroscopic level, a weld represents a thermo-mechanical problem of computing transient temperature, stress and strain, whereas at the microscopic level, it is a problem of physical metallurgy involving phase transformations, defect recovery, recrystallization and grain growth. Welds may consist of tens of passes, each of which contributes to the mechanical and metallurgical effects. Interactions between thermal, mechanical, metallurgical and, in the molten pool, chemical and fluid processes are quite complex, and experimental measurements are required to validate theoretical and modeling predictions.

Generally, three types of residual stress can be identified on the basis of the range over, which they are observed: the first type (σ^I) is termed macro-stress and influences thousands of crystalline grains; the second one (σ^{II}), the micro-stress, occurs between different phases or grains and covers a distance of about one grain; the third one (σ^{III}) ranges over few atomic distances. To study the microstructural behavior of the material, σ^{II} and σ^{III} are very important because allow for a better understanding the way in which lattice defects, in particular, dislocation arrangements, evolve. The σ^I stress is taken into consideration in designing engineering structures.

In many cases, the stress near the molten zone reaches the yield stress of the alloy and causes plastic deformation with microstructural changes, namely increase of point defect and dislocation density and decrease of grain size. The stresses σ^{II} and σ^{III} are strictly correlated to these microstructural features and are studied by X-ray and neutron diffraction. The techniques for analyzing σ^{II} and σ^{III} stresses involve the study of diffraction peak profiles and are not treated here because the topic goes beyond the scope of the chapter.

Several qualitative and quantitative techniques have been developed to measure residual stress. In fact, they measure strain rather than stress, and residual stress is then determined using the specific elastic constants of the material such as Young's modulus and Poisson's ratio. The wide range of available methods makes it impossible to include all of them in this chapter. In the following, some techniques, divided into two groups, namely destructive and nondestructive, will be reviewed.

The techniques of the first group are based on the destruction of the state of equilibrium of the residual stress in a mechanical component so residual stress is measured by its relaxing. The procedure used can be described as follows: (i) creation of a new stress state by machining or

layer removal; (ii) detection of the local change in stress by measuring the strain and (iii) calculation of the residual stress as a function of the measured strain through either an analytical approach or finite element (FE) calculations. The methods described here are: (i) sectioning; (ii) contour; (iii) hole-drilling and (iv) instrumented indentation.

The second group of techniques consists of nondestructive methods based on the relationship between residual stress and physical or crystallographic parameters of the material. Here, the attention has been focused on: (i) Barkhausen noise; (ii) ultrasonic; (iii) X-ray and neutron diffraction.

2. Destructive techniques

2.1. Sectioning method

The sectioning method is a destructive technique used for decades from lots of researchers to measure residual stress in structural parts and welded components. The method was developed for the first time in 1888 by Kalakoutsky to determine longitudinal stresses in a bar by slitting longitudinal strips from the bar and measuring their change in length [9, 10]. The stress analysis is simplified by assuming that transverse stress is negligible and the cutting process alone does not produce appreciable strains [8].

The slitting process is delicate since it should not introduce plasticity or heat in the cut samples maintaining the original residual stress without the influence of external factors [6]. The strains released during the cutting process are generally measured using electrical or mechanical strain gauges [6]. To determine residual stress in a plate, some attentions about sample preparation have to be done; in particular, the number of the longitudinal strips to be cut depends on the residual stress gradient [10].

The use of mechanical strain gauges have been found to be particularly suitable for the sectioning method since the device is not attached to the specimen, is not damaged during the sectioning and can be used in repeated measurements. The stress distribution over a cross section can be determined by measuring the change in length of each strip and by applying the Hooke's law [10].

The main sources of error result from temperature changes and may be practically eliminated using a reference bar of the same material.

Sectioning method has been extensively used to analyze residual stresses in welded joints, for instance, in A36 steel with fillet welds [11], high strength steel Q460 box sections [12] and thin Al-5456 panels [13]. Strips sliced at regions of high stress gradients can be considerably curved; thus, the change in length measured by the strain gauge is the change in the chord length rather than the change in arc length, which represents the actual strain [10].

In conclusion, the sectioning method is an adequate, accurate and economical technique for residual stress measurement in structural members thanks to its versatility and reliability [8, 10].

2.2. Contour method

The contour method (CM) was first proposed by Prime in 2000 [14]. CM is based on the superposition principle assuming that the material behaves elastically during the relaxation of residual stress and that the material removal introduces negligible stress [7, 14].

As shown in **Figure 1**, the displacements due to the relaxation of the internal stress are compared to an assumed flat surface contour, and the longitudinal residual stress is recreated using a FE model. The forces required to ensure that the measured deformed surface is returned to its original position are directly correlated to the residual stress. The method provides a 2D map having a regular resolution of the residual stress normal to the cut surface [14, 15].

The application of CM involves four steps: (i) cutting, (ii) measurement of surface contour, (iii) data handling and (iv) stress calculation [16].

- i. *Cutting.* The cut of the sample is a crucial step since it must be precise and straight without causing plastic deformation [16, 17]; owing to its suitable characteristics, wire electric discharge machining (wire EDM) is commonly used for the purpose [18]. Special attention is required for an adequate cutting process (single flat cut, proper constraint of the specimen to avoid its movement during cutting, a constant width of cut). Moreover, the type of cutting wire, the material, the geometry of the specimen and the EDM operating parameters are extremely important to realize an optimal cut. Finally, the cutting wire should be as thin as possible to remove the minimum material, particularly in the cases where there is a high stress gradient [19].
- ii. *Measuring the surface contour.* The contours of the cut surfaces can be measured using a coordinate measuring machine (CMM) [20]; typically, each surface contour is defined by about 10,000 points and the operation takes several hours.

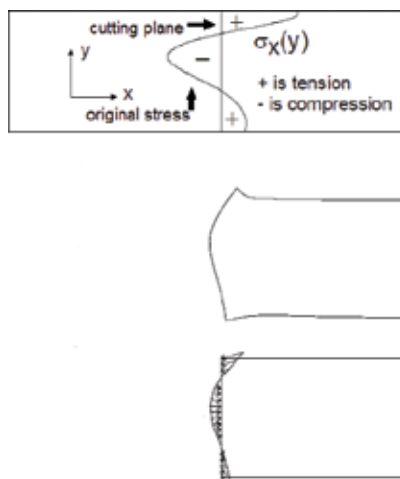


Figure 1. Schematic principles of the contour method [14].

In 2003, Prime et al. [21] developed a laser measuring system that works by moving one or more precision laser ranging probes over the entire surface with two orthogonal axes of motion, acquiring precision x, y and z spatial coordinates to submicron precision and resolution. A typical scan may take 30 min to an hour to complete with a resolution of 10 microns along the probe direction and 100 microns between scan lines. Noncontact laser surface contouring improves the capability of CM by allowing higher resolution measurement of a surface contour [21].

- iii. *Data handling.* Data from the two measured surfaces are aligned. Such procedure generally requires flipping, translation and rotation of one data set to match the other. To smooth out noise in the measured surface data and to enable evaluation at arbitrary locations, the data are fitted to bivariate Fourier series. Finally, since the contour must be defined everywhere for calculating the stress, any missing area of the surface is filled in by extrapolating constant values from the defined region [16].
- iv. *Stress calculation.* The residual stress is calculated from the measured surface contours using a FE model [22].

The multiaxial CM is a variation of the standard CM and its principles have been discussed by DeWald et al. [23]. This method uses displacements to calculate the eigenstrain distribution within the body; then from eigenstrain, the residual stress is determined by means of FE. The motivation for using eigenstrain to determine residual stress in CM is that eigenstrain remains constant upon residual stress redistribution. Hence, multiple cuts can be made without changing the eigenstrain distribution [20, 23]. Implementation of the multi-axial CM involves making multiple cuts along different orientations of a continuously processed prismatic specimen. Initially, the specimen is cut into two halves as in the conventional CM. The new cut surfaces are measured, and the results are averaged. Then, the two halves are cut along their diagonal. The displacements normal to the cut surfaces are contoured and averaged. After all the measurements are completed, the eigenstrain components are obtained from these three different measured and averaged surfaces [20]. The multi-axial CM technique was successfully applied to measure residual stress in variable polarity plasma arc (VPPA)-welded plates of 2024-T35 aluminum alloy [20], thin sheets of Ti-6Al-4 V and thick laser peened plates of 316 L stainless steel [23].

The validity of CM measurements has been assessed by comparing its results with those from neutron diffraction, X-ray (lab and synchrotron) diffraction and hole drilling [15, 18, 24–26].

Recently, Pagliaro et al. [27] suggested to use superposition to determine internal residual stresses by sectioning with CM and then measuring remaining stress with other methods. This approach allows measurements in parts where the internal stress were previously difficult to access and opens up possibilities to combine the advantages of different techniques [27].

CM has found a number of applications; some of them are of particular relevance such as butt joints of S355 structural steel [28], 80-mm thick ferritic steel welds [24], 70-mm thick dissimilar metal (ferritic to austenitic) welds [15] and ferritic steel plates welded using low and very high heat input processes [25], friction stir welds between 25.4-mm thick plates of

aluminum alloys 7050-T7451 and 2024-T351 [29], 2024-T351 aluminum alloy VPPA welds [19], welded Tee-joints [22], welds of 13% Cr–4% Ni steel [30, 31], 316L stainless steel bead-on-plate specimens [32] and AA6061-T6 aluminum alloy friction stir butt welds [33].

While the sectioning technique is easier to determine residual stress over weld cross sections since almost no calculations are needed, CM provides a higher spatial resolution (1 mm spacing) [15].

CM can only be used to obtain high-resolution maps of the stress normal to the cut surface [6], but it is quite insensitive to inhomogeneities in the specimen as long as they do not significantly affect the elastic constants [29]. CM is cheap and powerful and can be used to choose appropriate measurement lines in welded structures for more detailed study, for example using neutron diffraction [7]. A further advantage of CM, compared to the few other methods that can measure a comparable stress map, is that it is relatively simple and inexpensive to perform and the equipment required is widely available [21].

2.3. Hole-drilling method

The hole-drilling method (HDM) is versatile, easy, cheap, quick and standardized [4–6, 34] and is one of the techniques most used today for measuring residual stress. The principle, proposed more than 80 years ago [35], is based on the fact that relaxation occurs if some material is removed from a part with internal residual stress and it can be evaluated through the induced local deformation. In practical terms, an hole is drilled in the component at the center of a rosette strain gauge and a suitable model is used to determine the internal stress from strain data.

HDM equipment can be laboratory-based or portable, and the technique is applicable to a wide range of materials and components.

Drill speed and feed, centering of rosette and perpendicularity to the analysis surface are the main parameters affecting the measures of internal stress; operator skill and drilling equipment also play a significant role. Today, a modern integrate measure device consists of an automatic system including an high speed turbine (up to 400,000 rpm) with tungsten carbide tools and an electric stepping motor for the vertical cutter advancement with controlled drilling speed (0.1 mm/min); a microscope endowed of two orthogonal centesimal movements for drilling the hole at the center of rosette.

The other crucial aspect is the measure of the strain through rosette strain gauges. The ASTM E837-08 standard of reference for HDM residual stress evaluation [36] prescribes three kinds of rosette (Type A, B and C) as shown in **Figure 2**.

The ASTM E837-08 standard considers both uniform and nonuniform residual stress.

The evaluation of residual stress by HDM can be done in alternative ways. Since 1988, Schajer [37] introduced the *incremental method* for evaluating the nonuniform residual stress that allows to decide the number of step and the step depth. In the cases of coating or surface

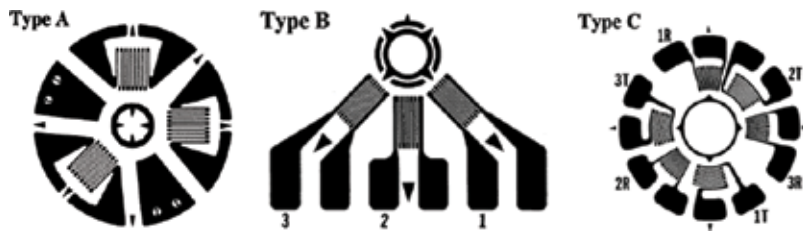


Figure 2. ASTM E837-08 standard: rosette types A, B and C.

treatment processes, for example shot peening, where more interesting is the evaluation of the residual stress in the first layer of the surface, the method permits to increase the resolution by reducing the step depth near the surface.

The *incremental deformation method*, proposed by Schwarz and Kockelmann [38], is based on the measure of the incremental deformation during drilling. In addition to the standard hole obtained by high speed milling, Kockelmann proposed also a new hole shape to be obtained by electrochemical erosion. Improvements of the mentioned methods are available in literature in terms of evaluation of relaxation strain and models. One of them, proposed by Beghini et al. [39], takes in consideration the compensation of the principal parameters affecting the accuracy in the evaluation of residual stress.

In general, for the HDM, the following experimental factors play a crucial role:

Rosette strain gauge installation: The installation needs to be performed by qualified person in compliance with the instructions of rosette and glue producer. Moreover, special attention should be paid to the cleaning of the surface where the strain gauge is bonded to avoid an alteration of the original state of residual stress.

Centering: The eccentricity between the center of the hole and the center of the rosette could introduce large error in the evaluation of residual stress.

Orthogonality and zeroing: A not accurate orthogonality between hole axis and surface could induce difference in the right measure of the depth of the hole and difficulty in zeroing.

Hole bottom fillet radius: The error in evaluating residual stress increases with the fillet radius and decreases with the depth of the hole [40].

One of the most common fields of HDM application is the evaluation of residual stress induced by welding processes. In fact, residual stress could affect the operative strength of the part, fatigue life and stress corrosion strength. In as-welded conditions, often residual stress is close to yield stress and thermal or mechanical treatments are necessary to reduce it. So, a lot of research work was done for the evaluation of residual stress in different kinds of welding processes and materials [30, 31, 40–45] with the final target to find the correct welding parameters and post processing conditions to minimize the residual stress. Some of these works use HDM as validation of nondestructive techniques such as ultrasonic [41–46], XRD [30] and neutron diffraction [31].

Pappalettere et al. [47–52] applied an electronic speckle pattern interferometry (ESPI) method to avoid the use of conventional rosette strain gauges. The ESPI is based on the correlation between two speckle patterns, each one created by the interference between a reference beam and the image of an object illuminated by a laser. Typically, the two images are of an object before and after some deformation and the technique measures the 3D displacement by evaluating the phase difference of two recorded speckle interferograms. The apparatus consists of a diode-pumped solid state laser source that generates a radiation split into two beams and focused into two monomode optical fibers. One beam is collimated through a biconvex lens and illuminates the sample, whereas the second one passes through a phase shifting piezoelectric system and then it goes to the CCD camera where interferes with the light diffused by the optically rough surface of the specimen. The camera is equipped with an optical imaging system allowing fine focusing of the image. Initial phase and final phase are evaluated by the four-step phase shifting technique. Once the initial and the final phases are determined, it is possible to calculate the amount of displacement of each point into the analysis area. **Figure 3** shows the experimental ESPI set-up [47]. In fact, rosette strain gauges introduce a not negligible cost particularly in the case where a relevant number of measurements are required. Moreover, some sources of experimental errors, such as surface preparation, bonding and positioning, are irrelevant using the not contact ESPI.

These investigators were also able to evaluate how drilling speed affects error in HDM and HDM/ESPI and concluded that higher speed helps to increase accuracy and reduce data scattering. For instance, standard deviation in residual stress evaluation in titanium samples changes from less than 3% to about 19% if drilling speed is reduced from 50,000 to 5000 rpm.

HDM was used to validate the results of the ultrasonic technique in investigations on FSW joints of 5086 plates [42], AISI 304 pipes [43] and plates [44]. The example in **Figure 4** shows the good correspondence between ultrasonic and HDM residual stress evaluation.

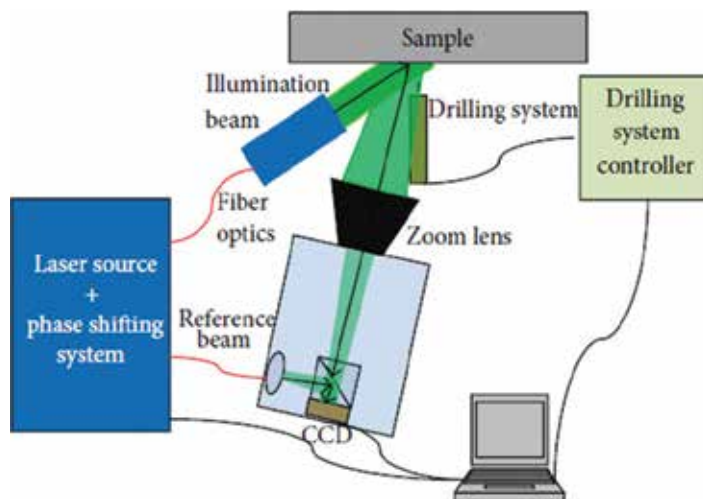


Figure 3. ESPI strain measurement set-up [47].

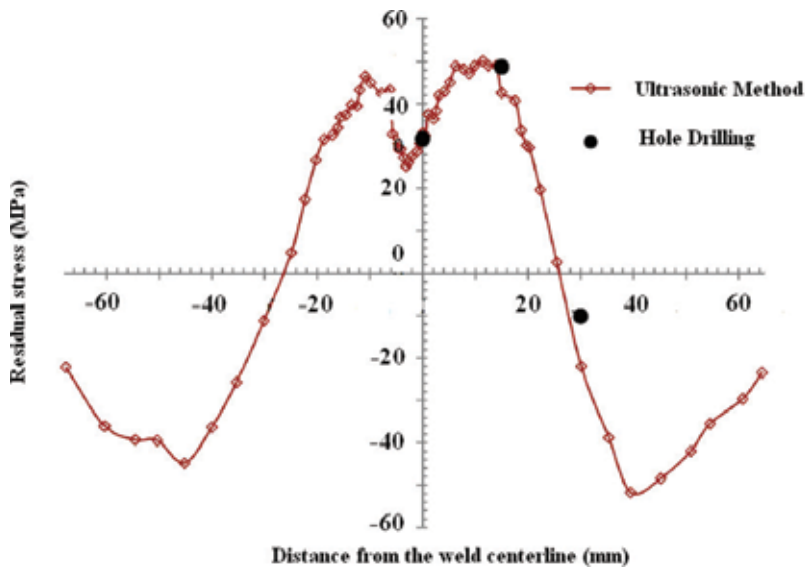


Figure 4. HDM validation of residual stress measurements performed through ultrasonic method. Redrawn from Ref. [42].

2.4. Instrumented indentation method

In the last decade, the instrumented indentation has received increasing attention for characterizing the mechanical properties of materials on a local scale. Indenters with different geometry (tetragonal Vickers pyramid, trigonal Berkovich pyramid, sphere, cone and cylinder) have been used; the following considerations refer to a sharp conical indenter (with a half apex angle α). It penetrates normally into a solid where the applied load P and penetration depth h are continuously recorded during one complete cycle of loading and unloading (Figure 5a and b).

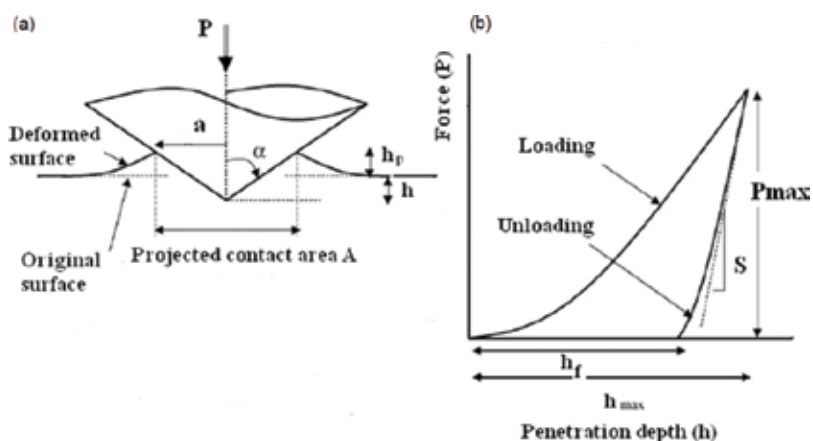


Figure 5. (a) Sketch of a sharp indentation on a homogeneous and isotropic material and (b) typical force-penetration depth curve obtained from an indentation experiment.

The contact stiffness $S = dP/dh$ is obtained from the slope of initial part of the unloading curve (**Figure 5b**).

As the indenter, a rigid cone with $\alpha = 70.3^\circ$, penetrates the materials, either plastic pile-up at the crater rim (when the ratio between yield stress σ_y and Young's modulus E , σ_y/E , is small) or elastic sink-in (when σ_y/E is large) is observed. The amount of pile-up/sink-in is denoted as h_p (**Figure 5a**). For conical indenters, the projected contact area A is given by:

$$A = \pi a^2 = \pi (\tan \alpha)^2 h_c^2 = 24.5 h_c^2 \quad (1)$$

where the contact depth, $h_c = h + h_p$, contains the contributions of both plastic pile-up around the indenter and elastic sink-in, which is counted negative. The pile-up and contact area can be measured experimentally or determined from numerical analysis (e.g. FE method). Once the contact area A is known, hardness H and Young's modulus E are usually obtained from the indentation curve.

Hardness H is the ratio between applied load P and contact area A ($H = P/A$).

The indentation modulus M is determined from indentation curve through the equation:

$$M = \frac{S}{2\gamma\beta\sqrt{A}} \sqrt{\pi} \quad (2)$$

where β is a shape factor ($\beta = 1$ for axisymmetric indenters and $\beta = 1.03$ – 1.05 for indenters with square or rectangular cross-sections) and γ is a correction factor depending on indenter geometry. In the case of the conical indenter, γ can be written as:

$$\gamma = \pi \frac{\pi/4 + 0.155 \cot \alpha \left[\frac{1-2\nu}{4(1-\nu)} \right]}{\left[\pi/2 - 0.831 \cot \alpha \left[\frac{1-2\nu}{4(1-\nu)} \right] \right]^2} \quad (3)$$

where ν is the Poisson's ratio.

For isotropic materials, the indentation modulus M corresponds to the plane-strain modulus E^*

$$M = E^* = \left(\frac{1-\nu^2}{E} + \frac{1-\nu_I^2}{E_I} \right) \quad (4)$$

where E_I and ν_I are the Young's modulus and Poisson's ratio of the indenter, respectively. Therefore, E can be easily calculated from M through Eq. (4).

How to correctly determine residual stresses from instrumented indentation test has been debated for some years. Initially, indentation hardness was used as a parameter of the residual stress; however, successive studies [53, 54] reported that the intrinsic hardness is invariant, regardless of the residual stress. Therefore, the change in contact morphologies with residual stress was modeled for constant maximum indentation depth assuming the independence of intrinsic hardness and residual stress [54].

The presence of residual stresses modify the indentation curve: with respect the stress-free state the same penetration depth h_t is reached at smaller load P in the case of tensile stress while compressive stress induces the opposite effect [53–55]. As shown in **Figure 6**, at the common penetration depth h_t , it is observed that P_A (with tensile stress) $<$ P_B (stress free) $<$ P_C (with compressive stress).

The direct comparison of the indentation curve recorded in the investigated zone with that obtained in a zone of the same material without any residual stress allows to understand the nature of the stress (tensile or compressive).

To determine the value of residual stress, we will examine in the following the case of a material with residual tensile stress; a similar analysis can be made for compressive stress.

Since the average contact pressure due to indentation, P_{ave} (equivalently, the hardness), is unaffected by any pre-existing tensile or compressive elastic stress [53], the relationship

$$P_{ave} = \frac{P}{A} = \frac{P_0}{A_0} \tag{5}$$

relates the indentation loads P and P_0 directly to the real contact areas A and A_0 of the material with and without residual stress, respectively. An equibiaxial tensile residual stress at the material surface can be considered equivalent to a tensile hydrostatic stress plus a uniaxial compressive stress component, $-\sigma_H$ (see **Figure 6**). This compressive stress component induces a differential indentation force $\sigma_H A$ acting in the same direction as the indentation load P . On these grounds, a tensile residual stress aids indentation by lowering the indentation load needed to penetrate the material to a given depth, as compared to the virgin material.

From the initial part of the unloading curve, the real contact area A at maximum load P_{max} for the material with the residual stress is

$$A = \left(\frac{dP}{dh} \frac{1}{cE^*} \right)^2 \tag{6}$$

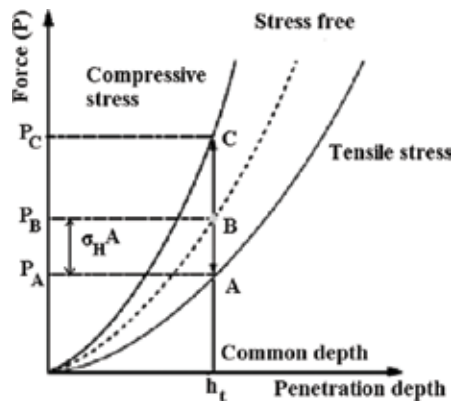


Figure 6. Effect of stress states on the indentation loading curve.

where c is a constant depending on the indenter geometry ($c = 1.167$ for Berkovich indenter, $c = 1.142$ for the Vickers indenter). An analogous relationship is found for the unstressed material; thus, it can be easily demonstrated that

$$\frac{A}{A_0} = \left(\frac{dP}{dh}\right)^2 \left(\frac{dP_0}{dh_0}\right)^{-2} = \left(1 + \frac{\sigma_H}{P_{ave}}\right)^{-1} \quad (7)$$

where P_{ave} is the average pressure.

The ratio A/A_0 is determined from the initial slopes of the unloading parts of the P - h curves. The value of A is calculated through Eq. (6), and at $P = P_{max}$ the average pressure $P_{ave} = P_{max}/A$. The residual stress magnitude σ_H is found by introducing the calculated values of A/A_0 and P_{ave} into Eq. (7).

The stress determined in this way is that of a layer of depth h_{max} corresponding to P_{max} and represents an average value over the layer. With the availability of macro-, micro- and nanoindenters, instrumented indentation can be used to probe local properties at different size scales.

The technique has been successfully used for determining residual stresses in different metallic alloys and recently also in tissues and other soft biological materials (e.g. see [56]).

Owing to its specific characteristics, indentation is quite useful for investigating welded mechanical parts because it allows to determine the residual stress on local scale, namely in the melted and heat affected zones of the joints. Instrumented indentation was applied by Jang et al. [57] for evaluating residual stress in A335 P12 steel welds in electric power plant facilities before and after stress-relaxation annealing. Comparison with the results of conventional saw-cutting tests showed the efficiency of indentation tests. The method was employed by Ullner et al. [58] to determine the local stresses in resistance-spot welded joints of advanced high strength steels.

3. Nondestructive techniques

3.1. Barkhausen noise method

Magnetic methods rely on the interaction between magnetization and elastic strain in ferromagnetic materials; they are sensitive to all three types of residual stress, but cannot distinguish between them. Here, only the Barkhausen noise (BN) method, based on the analysis of magnetic domain wall motion, will be presented and discussed.

Ferromagnetic materials consist of magnetically ordered regions called domains; each domain is magnetized along a certain direction and is separated from the others by walls where the direction of magnetization abruptly turns. The net magnetization of a material is the average of the magnetizations within all domains.

Under the action of an external magnetic field, the domain walls move and the resulting change in magnetization is detected as electrical pulses in a coil placed near the material

surface. The process is not continuous but consists of small steps generated by domains jumping from one position to another. Pulses are random in amplitude, duration and temporal separation and give rise to a noise-like signal called Barkhausen noise.

BN is exponentially damped as a function of the traveled distance inside the material and the extent of damping determines the depth from which information can be obtained. Such depth mainly depends on the signal frequency together with conductivity and magnetic permeability of the tested material. Measurement depths in steels range from 0.01 to 3.0 mm; since this value is much higher than that of X-ray diffraction (some tens of microns), the BN method allows to quantify subsurface stress without need of removing the surface layer.

The intensity of BN depends on both stress and microstructure of the material; thus, a suitable calibration is of the utmost importance to properly determine uniaxial and biaxial surface stresses. Grain size, texture and dislocation structures play an important role in BN response; therefore, it is necessary to separate the contribution of stress from that of microstructure through a suitable calibration procedure. Calibration involves measurement of the BN signal on a representative section of the sample material using a known applied stress. A typical uniaxial calibration curve, taken from Kesavan et al. [9], is shown in **Figure 7**. The handbook [3] reports more details of uniaxial and biaxial stress calibration procedures and related results for isotropic and anisotropic materials.

As a result of magnetoelastic interaction, in materials with positive magnetic anisotropy (most steels and cobalt alloys), compressive stresses decrease the BN intensity, whereas tensile stresses increase it. Therefore, the measurement of BN intensity allows to determine the amount of residual stress and also defines the direction of principal stresses.

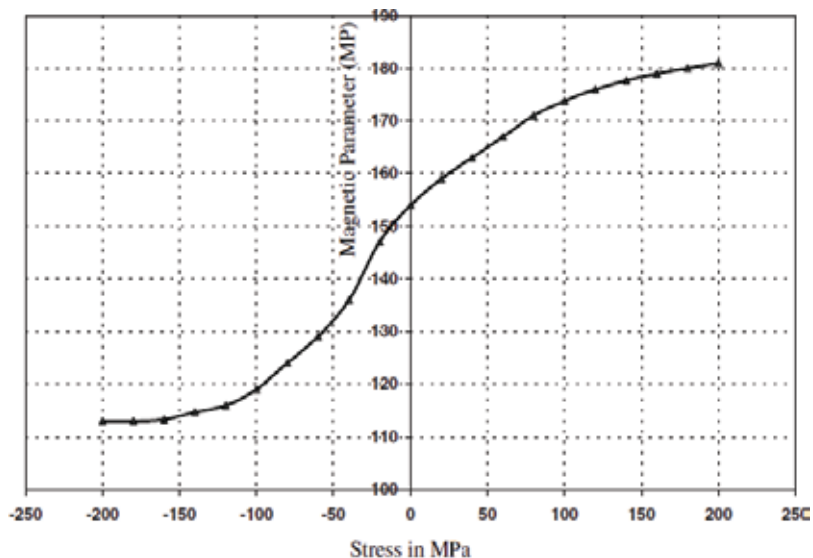


Figure 7. Typical uniaxial calibration curve taken from Ref. [9].

The advantages of the BN method for stress measurements in welds are that it is fast, reliable and requires no specific surface preparation. Moreover, it can be used for continuous monitoring of stress in industrial processes. A significant example is reported in **Figure 8** showing the effect of furnace stress relieving on a welded “T” section [3]; it is noteworthy that the stress profiles of the two seams before stress relieving are asymmetric because the left seam was welded first, being then subjected to a strong heating during the realization of the right seam.

Vourna et al. [59–61] examined through the BN method joints of an electrical steel (Si 2.18 wt%) welded by means of three different techniques, namely Tungsten Inert Gas (TIG), Plasma and Electron Beam, determining maps of residual stress across melted zone, heat affected zone and base material. The comparison of results with those from X-ray diffraction showed a good agreement. Similar good results were achieved by measurements performed on other types of steels such as API X65 [62], API 5 L X70 [63], AS1548–7-460R [64], structural steel [65] and Cr-Mo steel [66]. As pointed out by many investigators who examined welds of different steels, BN technique requires a precise calibration procedure in all zones, which have a noticeably different microstructure, namely each zone should be separately considered for calibration [59, 60, 61, 63].

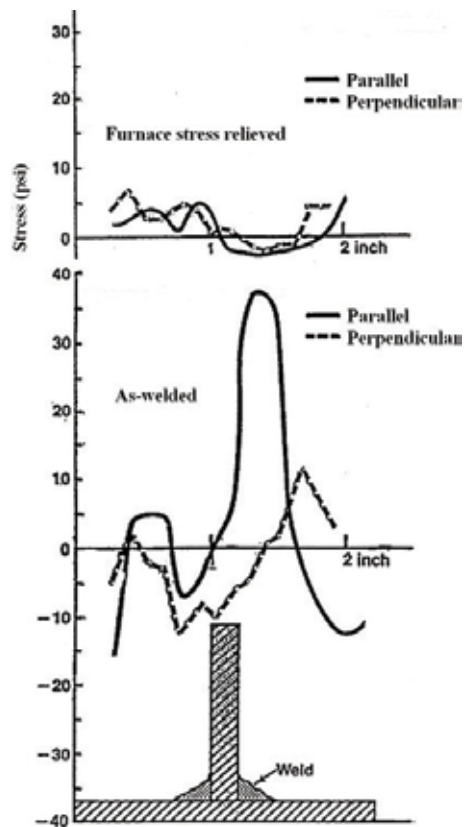


Figure 8. Stress relieving on a welded “T” section measured through BN; redrawn from Ref. [3].

The potential of BN technique for directly assessing fatigue processes and progressive residual stress relaxation in cyclically loaded welds has been shown by Lachmann et al. [67].

Beside the aforesaid advantages of the BN technique, some drawbacks place a severe restriction on its general applicability: (i) the material must be ferromagnetic; (ii) the total range of stress sensitivity (~ 6 MPa) is low; (iii) the measurement depth is limited to the surface layers and (iv) BN signal saturation may occur when tests are carried out on martensitic steels with very fine and complex microstructural features.

3.2. Ultrasonic method

The ultrasonic techniques are based on variations in the velocity of ultrasonic waves, which can be related to the residual stress state through the elastic constants of the material [34, 44]. Like the magnetic methods, the ultrasonic techniques are sensitive to all three kinds of residual stress, but are not able to distinguish between them.

Ultrasonic stress measurement is founded on the linear relation between velocity of the ultrasonic wave and the material stress. This correlation, known as the acoustoelastic effect, establishes the following relationship between the velocity V and the stress σ :

$$V = V_0 + K\sigma \quad (8)$$

where K is the acoustoelastic constant (AEC) depending on the material and V_0 and V are the velocities in stress-free and stressed material, respectively [3].

In 1967, Crecraft showed that the acoustoelastic law can be employed for stress measurement of engineering materials [35, 42, 45]. Changes in ultrasonic speed can be observed when a material is subjected to a stress, the changes providing a measure of the stress averaged along the wave path. The acoustoelastic coefficients necessary for the analysis are usually calculated using calibration tests. Different types of wave can be employed but the commonly used technique is the longitudinal critically refracted (Lcr) wave method [4]. The Lcr wave is an acoustical wave that is excited when the angle of incidence is slightly smaller than the first critical angle, which is calculated from the Snell's law [44, 68, 69]. It is a bulk longitudinal wave, traveling just below the surface of the specimen. This wave is more sensitive to stress and less sensitive to localized material texture changes [69]. Different ultrasonic configurations can be employed for residual stresses measurements by Lcr technique. As a common experimental setup, longitudinal waves are propagated at the first critical angle by a transmitter transducer and then travel parallel the tested material surface and finally are detected by a receiver transducer. The residual stress in a subsurface layer is measurable while the depth of layer is related to the ultrasonic wavelength, often exceeding a few millimeters [43]. The relation between measured travel-time change of Lcr wave and the corresponding uniaxial stress was derived by Egle and Bray [70]; with knowledge of the weld induced change in travel time and the measured acoustoelastic constant, the stress produced by the weld may be calculated [43]. The principal steps to be followed in the measurement of residual stress by ultrasonic methods are: (i) selection of weld joint or component; (ii) determination of the acoustoelastic constant (AEC) of the material using standard tensile specimen by applying

varying loads; (iii) ultrasonic velocity measurements in the weld joint or component of interest and (iv) determination of residual stress using AEC [68].

Javadi et al. [41–43] carried out a series of interesting studies on the ultrasonic method. They compared contact and immersion ultrasonic measurements of welding residual stress in dissimilar joints. A combination of FE welding simulation and Lcr ultrasonic waves was employed to reach the goal, and on the basis of experimental results, they concluded that both of the methods can measure the residual stress with an acceptable accuracy and the selection between them depends on geometry and dimensions of tested structure and also on the available experimental devices [41].

The same investigators developed a method (TLcr) that is the combination of Taguchi method (a technique to optimize welding parameters) and the Lcr ultrasonic method in order to study which process parameter has the highest effect on the longitudinal residual stresses in aluminum plates joined by the FSW process [42]. Finally, Javadi et al. [43] studied the combination of FE and Lcr method (known as FELCR) confirming its ability to evaluate the pipe residual stresses through the thickness.

The ultrasonic technique was also successfully used in the study of residual stress in dissimilar joints [41]; residual stress through the thickness of stainless steel plates with 10 mm thickness [44]; longitudinal residual stress through the thickness of aluminum plates with 8 mm thickness [45]; for assessment of surface/subsurface longitudinal residual stresses in AISI type 316LN stainless steel weld joints made by ATIG and TIG welding processes [68]; welding residual stress through the thickness of stainless steel pipe [43] and prediction of total residual stress and fusion boundary in three pass welded stainless steel plates [71].

In conclusion, the ultrasonic technique is nondestructive, sensitive to microstructures and defects, has sufficiently good spatial resolution (5 mm) for longitudinal residual stresses across welded joints and is easy and simple to use and cost effective [8, 69, 72]. Additionally, the instrumentation is portable and quick to implement [34] and it is well suited for routine inspection procedures and industrial studies of large components, such as steam turbine discs [4]. On the other hand, this method has some difficulties in separating the effects of multiaxial stresses and in measuring the stress in an exact depth; since the penetration depths of the ultrasonic transducers are limited to a few millimeters, measurement of thick materials on both sides is recommended.

3.3. X-ray and neutron diffraction method

X-ray and neutron diffraction methods are based on the measurement of lattice strains by studying the variations of lattice spacings of the polycrystalline material. In other words, these techniques allow to determine the variations of lattice spacings induced by compressive or tensile stresses and to calculate the stresses from the strains, known the elastic constants of the material under investigation. Neutron and X-ray wavelengths used in diffraction experiments are about of the same magnitude; however, neutron diffraction differs from X-ray diffraction in several ways. Two aspects are of particular relevance to the present discussion:

1. The penetration depth in a material of a neutron beam is of the order of some centimeters and that of X-rays is of tens of microns. Therefore, X-ray diffraction measures the residual strain on the surface of the material, whereas neutron diffraction measures the residual strain within a volume of the sample. Owing to its unique deep penetration, neutron diffraction has been used to measure stresses in welds of 50-mm thick steel plates [73]. High energy X-rays from synchrotron sources have the penetration depth in between and are used to investigate subsurface stresses.
2. The intensities of X-ray diffraction lines depend on the atomic scattering factor f , which is directly proportional to the atomic number Z ; thus, in a polyphasic material, the phases rich of light elements will exhibit diffraction patterns of lower intensity with respect to those rich of heavy elements. For instance, in a steel with perlitic structure (ferrite plus cementite), only the diffraction lines of ferrite are revealed, whereas those of cementite have a negligible intensity, comparable with background.

In the case of neutrons, scattering intensity varies quite irregularly with the atomic number Z ; therefore, elements with quite different values of Z may scatter neutrons equally well. Furthermore, some light elements, such as carbon, scatter neutrons more intensely than some heavy elements. It follows that structure analyses can be carried out with neutron diffraction that are impossible, or possible only with great difficulty, with X-ray.

Both neutron and X-ray diffraction techniques can be used to study all three kinds of stresses. The peak shift method is sensitive to σ^I , whereas line broadening is sensitive to σ^{II} and σ^{III} .

Residual stresses in polycrystalline materials change the lattice spacings, which vary according to the orientation of planes relatively to the stress direction. In fact, the crystal lattice is used as a strain gauge. The elastic strain can be calculated from the variation of lattice spacing d : d_0 , determined by the position of the Bragg peak of stressed (θ) and stress-free (θ_0) material:

$$\varepsilon = \frac{d - d_0}{d_0} = -\Delta\theta \cot \theta \quad (9)$$

The strain measured from shift of peak position is the elastic strain along the normal direction to diffracting planes, i.e. those parallel to the surface of the examined sample.

The $\sin^2\psi$ method allows to determine the stress along any direction Φ in the plane XY (**Figure 9**).

The direction Φ is the projection on the plane XY of the direction OO' forming an angle ψ with the axis Z. The stress σ_Φ is given by:

$$\sigma_\Phi = \frac{d_\psi - d_z}{d_z} \cdot \frac{E}{(1 + \nu)\sin^2\psi} \quad (10)$$

and is determined by measuring d_ψ and d_z , known E and ν . Through X-ray and neutron diffraction, it is possible to measure uniaxial, biaxial and triaxial stress states, an exhaustive treatment of the topic can be found in Ref. [3].

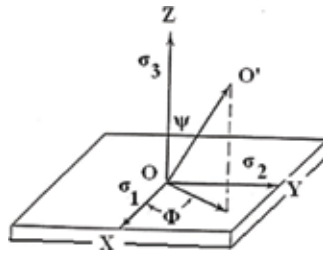


Figure 9. The direction Φ is the projection on the plane XY of the direction forming an angle ψ with the axis Z .

Since the Warren Averbach method [74] appeared in the 1950s, diffraction line broadening analysis is used to study the microstructural evolution of crystalline materials. Two factors contribute to line broadening: (i) the size of coherently diffracting domains (grains, sub-grains or cells) and (ii) micro-strains related to the density of dislocations, stacking faults and twins. Of course, line broadening is related to σ^{II} and σ^{III} and a lot of specific literature does exist on the matter; thus, we will not treat here the details of analysis.

X-ray and neutron diffraction has been extensively used to investigate stress state in welds realized with different techniques and materials (steels [73, 75–81], aluminum alloys [82–87], titanium alloys [88, 89] and other alloys). Remarkable results have been achieved; for instance, neutron and synchrotron X-ray diffraction has been successfully used for mapping residual stresses in welded parts (e.g. see [90]).

Woo et al. [86] were able to determine the evolution of temperature and thermal stresses during friction stir welding of Al6061-T6 through in situ, time-resolved neutron diffraction technique. The method allows to deconvolute the temperature and stress from the lattice spacing changes measured by neutron diffraction.

Two case studies taken from the research activity of the authors are now presented to illustrate the application of the technique.

3.3.1. Case study 1

Electron beam (EB) welding has been used to realize seams on 2-mm thick plates of directionally solidified IN792 superalloy [91–93]. The experiments evidenced the importance of pre-heating the workpieces to avoid the formation of long cracks in the seam and X-ray diffraction (XRD) was used to identify the better pre-heating temperature (PHT). The samples were mounted on a micrometric translating table that allowed to move the samples and irradiate the desired zone.

XRD spectra were collected by focusing the beam on melted zone and **Figure 10** compares the $\{220\}$ peak profiles of samples welded with PHT of 200 and 300°C at the same pass speed (1.5 m/min).

The vertical line indicates the peak position of stress-free base material. The peak position of the sample welded with PHT = 300°C almost corresponds to that of stress-free material (vertical line), whereas the peak position of sample welded with PHT = 200°C is shifted to lower angles

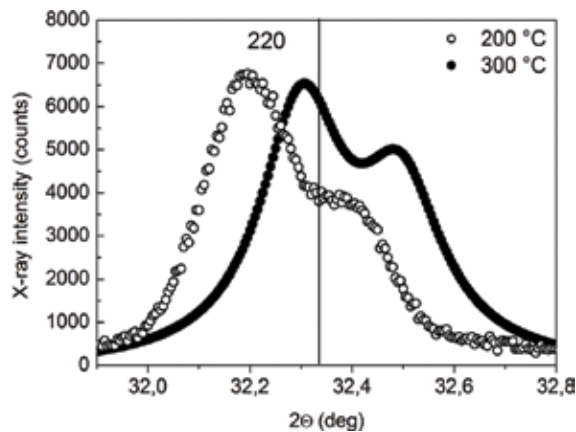


Figure 10. {220} peak profiles collected from melted zone of samples welded at the same pass speed of 1.5 m/min with PHT of 200 and 300°C. The vertical line indicates the peak position of base material free from the stresses arising from welding [93].

indicating the presence of tensile stresses. On the basis of these results, the pre-heating of the plates at 300°C was identified as the optimal condition to realize EB joints of IN792 DS superalloy.

3.3.2. Case study 2

Case study 2 presents a study on a joint with a very complex structure. Because of its high melting point and good thermal conductivity, W is a promising armor material for protecting the components of International Thermonuclear Experimental Reactor (ITER) from plasma damage. However, the joining of W to other metals is challenging for the lower thermal expansion of W, its high elastic modulus and brittleness. An experimental campaign has been carried out by authors for realizing thick W-coatings on different metals, and Plasma Spraying was used as deposition technique for its simplicity, the possibility to cover complex and extended surfaces and the relatively low cost. The reported example regards 5-mm thick W coatings deposited on CuCrZr alloy. An appropriate interlayer was optimized to increase the adhesion of W on the metallic substrate and to provide a soft interface with intermediate thermal expansion coefficient for better thermo-mechanical compatibility. The bonding interface with thickness of ~800 μm was realized through successive deposition steps. It consists of a layer of pure Ni (thickness ~200 μm) directly on the CuCrZr substrate followed by a stratification of thinner layers (thickness ~30 μm) obtained by spraying grading mixtures of Al-12% Si, Ni-20% Al, Ni-20% Al and W powders. A detailed description is given in [94, 95].

To verify the quality of joints, high temperature X-ray diffraction (HT-XRD) has been employed at increasing temperatures up to 425°C and XRD spectra are shown in **Figure 11**. The vertical lines indicate the peak positions of the strain-free metals at room temperature.

The positions of Cu and W peaks at 25°C correspond to those of the stress-free condition, whereas Al and Ni peaks exhibit significant shifts. This means that residual strains are present in the interlayer but not in coating and substrate. At 425°C, all the peaks move towards lower

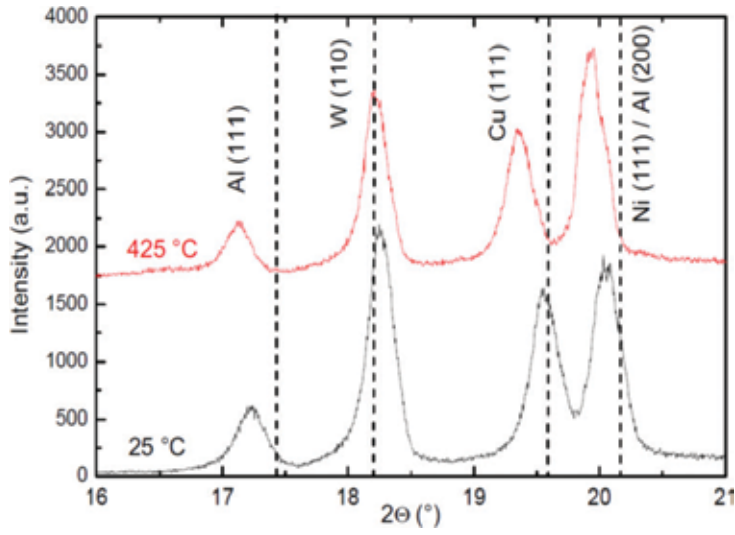


Figure 11. XRD spectra collected from W-CuCrZr system. The markers indicate the peak positions of stress-free metals (JCPDS-ICDD database).

angles, in part due to thermal expansion. **Table 1** shows the strains, corrected from the effect of thermal expansion, which are quite different in the metals of the system W-CuCrZr. Among them, W exhibits the lowest strain level ($\sim 5 \times 10^{-4}$) both at 25 and 425°C; thus, strain substantially does not change as temperature increases. At room temperature, also the strain of Cu is low ($\sim 1 \times 10^{-3}$) but it increases at 425°C. In the interlayer, a different behavior between Ni and Al is observed: the strain level in Al is about one order of magnitude higher than that of Ni.

Such results are very interesting if one considers that cracks form in W near the interlayer and then propagate by a brittle and transgranular fracture mechanism towards the substrate. In fact, they demonstrate that interlayer properly works by accumulating stress and protecting the coating. On this basis, HT-XRD permits to evaluate the quality of the deposition and can be used to orientate the work for optimizing structure and composition of the interlayer and to find the right parameters of deposition process.

Metal.	$\epsilon \times 10^3$	
	25°C	425°C
Al	13.30	10.20
W	0.51	0.54
Cu	0.94	4.42
Ni	1.25	1.92

Table 1. Strains at 25 and 425°C.

Author details

Roberto Montanari^{1*}, Alessandra Fava¹ and Giuseppe Barbieri²

*Address all correspondence to: roberto.montanari@uniroma2.it

1 Department of Industrial Engineering, University of Rome Tor Vergata, Rome, Italy

2 Department of Sustainability, ENEA Centro Ricerche Casaccia, Santa Maria di Galeria, Italy

References

- [1] Coyle RA. The measurement of residual stress. *Non-Destructive Testing*. 1984;**21**:6-9
- [2] Finch DN. *A Review of Non-destructive Residual Stress Measurement Techniques*. Leatherhead, Surrey, UK: ERA Technology Ltd; 1994
- [3] Lu J. *Handbook of Measurement of Residual Stresses*. USA: Society for Experimental Mechanics. The Fairmont Press Inc.; 1996. ISBN: 0-88173-229-X
- [4] Withers PJ, Bhadeshia HKDH. Residual stress Part 1 – Measurement techniques. *Materials Science and Technology*. 2001;**17**:355-365. DOI: 10.1179/026708301101509980
- [5] Withers PJ, Bhadeshia HKDH. Residual stress Part 2 – Nature and origins. *Materials Science and Technology*. 2001;**17**:366-375. DOI: 10.1179/026708301101510087
- [6] Rossini NS, Dassisti M, Benyounis KY, Olabi AG. Methods of measuring residual stresses in components. *Materials & Design*. 2012;**35**:572-588. DOI: 10.1016/j.matdes.2011.08.022
- [7] Withers PJ, Turski M, Edwards L, Bouchard PJ, Buttle DJ. Recent advances in residual stress measurement. *International Journal of Pressure Vessels and Piping*. 2008;**85**:118-127. DOI: 10.1016/j.ijpvp.2007.10.007
- [8] Huang X, Liu Z, Xie H. Recent progress in residual stress measurement techniques. *Acta Mechanica Solida Sinica*. 2013;**26**:570-583. DOI: 10.1016/S0894-9166(14)60002-1
- [9] Kesavan K, Ravisankar K, Parivallal S, Sreeshylam P. Non destructive evaluation of residual stresses in welded plates using the Barkhausen noise technique. *Experimental Techniques*. 2005;**29**:17-21. DOI: 10.1111/j.1747-1567.2005.tb00234.x
- [10] Tebedge N, Alpsten G, Tall L. Residual-stress measurement by the sectioning method – A procedure for residual-stress measurements by the sectioning method is described. Two different hole-drilling methods were performed and the results are compared. *Experimental Mechanics*. 1973;**13**:88-96. DOI: 10.1007/BF02322389
- [11] Alpsten GA, Tall L. Residual stresses in heavy welded shapes. *Welding Research Supplement*. 1970;**49**:93s-105s

- [12] Wang Y-B, Li G-Q, Chen S-W. The assessment of residual stresses in welded high strength steel box sections. *Journal of Constructional Steel Research*. 2012;**76**:93-99. DOI: 10.1016/j.jcsr.2012.03.025
- [13] Tsai CL, Park SC, Cheng WT. Welding distortion of a thin-plate panel structure. *Welding Journal*. 1999;**78**:156s-165s
- [14] Prime MB. Cross-sectional mapping of residual stresses by measuring the surface contour after a cut. *Journal of Engineering Materials and Technology*. 2000;**123**:162-168. DOI: 10.1115/1.1345526
- [15] Woo W, An GB, Truman CE, Jiang W, Hill MR. Two-dimensional mapping of residual stresses in a thick dissimilar weld using contour method, deep hole drilling, and neutron diffraction. *Journal of Materials Science*. 2016;**51**:10620-10631. DOI: 10.1007/s10853-016-0283-z
- [16] Prime MB, Hill MR, DeWald AT, Sebring RJ, Dave VR, Cola MJ. Residual stress mapping in welds using the contour method. In: *Proceedings of the 6th International Conference; 15–19 April 2002; Pine Mountain, Georgia*: ASM International; 2003. p. 891-896
- [17] Shin SH. FEM analysis of plasticity-induced error on measurement of welding residual stress by the contour method. *Journal of Mechanical Science and Technology*. 2005;**19**:1885-1890. DOI: 10.1007/BF02984267
- [18] Brown DW, Holden TM, Clausen B, Prime MB, Sisneros TA, Swenson H, Vaja J. Critical comparison of two independent measurements of residual stress in an electron-beam welded uranium cylinder: Neutron diffraction and the contour method. *Acta Materialia*. 2011;**59**:864-873. DOI: 10.1016/j.actamat.2010.09.022
- [19] Zhang Y, Ganguly S, Edwards L, Fitzpatrick ME. Cross-sectional mapping of residual stresses in a VPPA weld using the contour method. *Acta Materialia*. 2004;**52**:5225-5232. DOI: 10.1016/j.actamat.2004.07.045
- [20] Kartal ME, Liljedahl CDM, Gungor S, Edwards L, Fitzpatrick ME. Determination of the profile of the complete residual stress tensor in a VPPA weld using the multi-axial contour method. 2008;**56**:4417-4428. DOI: 10.1016/j.actamat.2008.05.007
- [21] Prime MB, Sebring RJ, Edwards JM, Hughes DJ, Webster PJ. Laser surface-contouring and spline data-smoothing for residual stress measurement. *Experimental Mechanics*. 2004;**44**:176-184. DOI: 10.1177/00144851039762
- [22] Murugan N, Narayanan R. Finite element simulation of residual stresses and their measurement by contour method. *Materials and Design*. 2009;**30**:2067-2071. DOI: 10.1016/j.matdes.2008.08.041
- [23] DeWald AT, Hill MR. Multi-axial contour method for mapping residual stresses in continuously processed bodies. *Experimental Mechanics*. 2006;**46**:473-490. DOI: 10.1007/s11340-006-8446-5

- [24] Woo W, An GB, Em VT, De Wald AT, Hill MR. Through-thickness distributions of residual stresses in an 80 mm thick weld using neutron diffraction and contour method. *Journal of Materials Science* 2015;**50**:784-793. DOI: 10.1007/s10853-014-8638-9
- [25] Woo W, An GB, Kingston EJ, DeWald AT, Smith DJ, Hill MR. Through-thickness distributions of residual stresses in two extreme heat-input thick welds: A neutron diffraction, contour method and deep hole drilling study. *Acta Materialia*. 2013;**61**:3564-3574. DOI: 10.1016/j.actamat.2013.02.034
- [26] Woo W, Feng Z, Wang XL, David SA. Neutron diffraction measurements of residual stresses in friction stir welding: A review. *Science and Technology of Welding & Joining*. 2011;**16**:23-32. DOI: 10.1179/136217110X12731414739916
- [27] Pagliaro P, Prime MB, Robinson JS, Clausen B, Swenson H, Steinzig M, Zuccarello B. Measuring inaccessible residual stresses using multiple methods and superposition. *Experimental Mechanics*. 2011;**51**:1123-1134. DOI: 10.1007/s11340-010-9424-5
- [28] Braga DFO, Coules HE, Pirling T, Richter-Trummer V, Colegrove P, de Castro PMST. Assessment of residual stress of welded structural steel plates with or without post weld rolling using the contour method and neutron diffraction. *Journal of Materials Processing Technology*. 2013;**213**:2323-2328. DOI: 10.1016/j.jmatprotec.2013.07.004
- [29] Prime MB, Gnäupel-Herold T, Baumann JA, Lederich RJ, Bowden DM, Sebring RJ. Residual stress measurements in a thick, dissimilar aluminum alloy friction stir weld. *Acta Materialia*. 2006;**54**:4013-4021. DOI: 10.1016/j.actamat.2006.04.034
- [30] Thibault D, Bocher P, Thomas M. Residual stress and microstructure in welds of 13% Cr–4% Ni martensitic stainless steel. *Journal of Materials Processing Technology*. 2009;**209**: 2195-2202. DOI: 10.1016/j.jmatprotec.2008.05.005
- [31] Thibault D, Bocher P, Thomas M, Gharghoury M, Côté M. Residual stress characterization in low transformation temperature 13% Cr–4% Ni stainless steel weld by neutron diffraction and the contour method. *Materials Science and Engineering A*. 2010;**527**:6205-6210. DOI: 10.1016/j.msea.2010.06.035
- [32] Turski M, Edwards L. Residual stress measurement of a 316l stainless steel bead-on-plate specimen utilising the contour method. *International Journal of Pressure Vessels and Piping*. 2009;**86**:126-131. DOI: 10.1016/j.ijpvp.2008.11.020
- [33] Liu C, Yi X. Residual stress measurement on AA6061-T6 aluminum alloy friction stir butt welds using contour method. *Materials and Design*. 2013;**46**:366-371. DOI: 10.1016/j.matdes.2012.10.030
- [34] Kandil FA, Lord JD, Fry AT, Grant PV. Review of Residual Stress Measurement Methods – A Guide to Technique Selection. NPL Report MATC(A)04. National Physical Laboratory, Teddington, Middlesex, UK; 2001
- [35] Ruud CO. A review of selected non-destructive methods for residual stress measurement. *NDT International*. 1982;**15**:15-23. DOI: 10.1016/0308-9126(82)90083-9

- [36] ASTM E837-08. Standard Test Method for Determining Residual Stresses by the Hole-Drilling Strain Gage Method. West Conshohocken, PA: ASTM International; 2009. DOI: 10.1520/E0837-08E02
- [37] Schajer GS. Application of finite element calculations to residual stress measurements. *Journal of Engineering Materials and Technology*. 1981;**103**:157-163. DOI: 10.1115/1.3224988
- [38] Schwarz T, Kockelmann H. The hole drilling method – The best technique for the experimental determination of residual stresses in many fields of application. *Messtechnische Briefe*. 1993;**29**:33-38
- [39] Beghini M, Bertini L, Mori LF. Evaluating non-uniform residual stress by the hole-drilling method with concentric and eccentric holes. Part II: Application of the influence functions to the inverse problem. *Strain*. 2010;**46**:337-346. DOI: 10.1111/j.1475-1305.2009.00684.x
- [40] Scafidi M, Valentini E, Zuccarello B. Effect of the hole-bottom fillet radius on the residual stress analysis by the hole drilling method. ICRS-8 – The 8th International Conference on Residual Stress; 6-8 August 2008; Denver, CO (USA). Newtown Square: JCPDS – International Centre for Diffraction Data; 2009. p. 263-270
- [41] Javadi Y, Najafabadi MA. Comparison between contact and immersion ultrasonic method to evaluate welding residual stresses of dissimilar joints. *Materials and Design*. 2013;**47**:473-482. DOI: 10.1016/j.matdes.2012.12.069
- [42] Javadi Y, Sadeghi S, Najafabadi MA. Taguchi optimization and ultrasonic measurement of residual stresses in the friction stir welding. *Materials and Design*. 2014;**55**:27-34. DOI: 10.1016/j.matdes.2013.10.021
- [43] Javadi Y, Pirzaman HS, Raeisi MH, Najafabadi MA. Ultrasonic inspection of a welded stainless steel pipe to evaluate residual stresses through thickness. *Materials and Design*. 2013;**49**:591-601. DOI: 10.1016/j.matdes.2013.02.050
- [44] Javadi Y, Akhlaghi M, Najafabadi MA. Using finite element and ultrasonic method to evaluate welding longitudinal residual stress through the thickness in austenitic stainless steel plates. *Materials and Design*. 2013;**45**:628-642. DOI: 10.1016/j.matdes.2012.09.038
- [45] Sadeghi S, Najafabadi MA, Javadi Y, Mohammadisefat M. Using ultrasonic waves and finite element method to evaluate through-thickness residual stresses distribution in the friction stir welding of aluminum plates. *Materials and Design*. 2013;**52**:870-880. DOI: 10.1016/j.matdes.2013.06.032
- [46] Ya M, Marquette P, Belahcene F, Lu J. Residual stresses in laser welded aluminium plate by use of ultrasonic and optical methods. *Materials Science and Engineering A*. 2004;**382**:257-264. DOI: 10.1016/j.msea.2004.05.020
- [47] Barile C, Casavola C, Pappalettera G, Pappalettere C. Analysis of the effects of process parameters in residual stress measurements on titanium plates by HDM/ESPI. *Measurement*. 2014;**48**:220-227. DOI: 10.1016/j.measurement.2013.11.014

- [48] Casavola C, Pappalettere C, Tursi F. Analytical study of strain's random error on residual stresses calculated by hole drilling method. 10th Youth Symposium on Experimental Solid Mechanics; 25–28 May 2011; Chemnitz, Germany. New York: Curran Associates, Inc.; 2014. p. 111-113
- [49] Barile C, Casavola C, Pappalettera G, Pappalettere C. Consideration on temperature fields and internal radius of analysis in hdm+espi residual stress measurements. XIIIth Youth Symposium on Experimental Solid Mechanics; 29 June–02 July 2014; Děčín, Czech Republic. New York: Curran Associates, Inc.; 2015. p. 11-14
- [50] Barile C, Casavola C, Pappalettera G, Pappalettere C. Considerations on the choice of experimental parameters in residual stress measurements by hole-drilling and ESPI. *Frattura ed Integrità Strutturale*. 2014;**30**:211-219. DOI: 10.3221/IGF-ESIS.30.27
- [51] Casavola C, Campanelli SL, Pappalettere C. Experimental analysis of residual stresses in the selective laser melting process. In: Proceedings of the XIth International Congress and Exposition; 2–5 June 2008; Orlando, Florida, USA: Society for Experimental Mechanics Inc.; 2008
- [52] Barile C, Casavola C, Pappalettera G, Pappalettere C. Remarks on residual stress measurement by hole-drilling and electronic speckle pattern interferometry. *The Scientific World Journal*. 2014;**2014**:1-7. DOI: 10.1155/2014/487149
- [53] Suresh S, Giannakopoulos AE. New method for estimating residual stresses by instrumented sharp indentation. *Acta Materialia*. 1998;**46**:5755-5767. DOI: 10.1016/S1359-6454(98)00226-2
- [54] Tsui TY, Oliver WC, Pharr GM. Influences of stress on the measurement of mechanical properties using nanoindentation: Part I. Experimental studies in an aluminum alloy. *Journal of Materials Research*. 1996;**11**:752-759. DOI: <https://doi.org/10.1557/JMR.1996.0091>
- [55] Lee Y-H, Kwon D. Residual stresses in DLC/Si and au/Si systems: Application of a stress-relaxation model to the nanoindentation technique. *Journal of Materials Research*. 2002; **17**:901-906. DOI: <https://doi.org/10.1557/JMR.2002.0131>
- [56] Boccaccio A, Papi M, De Spirito M, Lamberti L, Pappalettere C. Effect of the residual stress on soft sample nanoindentation. *Applied Physics Letters* 2013;**102**. DOI: 10.1063/1.4801428
- [57] J-I J, Son D, Lee Y-H, Choi Y, Kwon D. Assessing welding residual stress in A335 P12 steel welds before and after stress-relaxation annealing through instrumented indentation technique. *Scripta Materialia*. 2003;**48**:743-748. DOI: 10.1016/S1359-6462(02)00537-7
- [58] Ullner C, Brauser S, Subaric-Leitis A, Weber G, Rethmeier M. Determination of local stress–strain properties of resistance spot-welded joints of advanced high-strength steels using the instrumented indentation test. *Journal of Materials Science*. 2012;**47**:1504-1513. DOI: 10.1007/s10853-011-5936-3
- [59] Vourna P, Ktena A, Tsakiridis PE, Hristoforou E. An accurate evaluation of the residual stress of welded electrical steels with magnetic Barkhausen noise. *Measurement*. 2015;**71**: 31-45. DOI: 10.1016/j.measurement.2015.04.007

- [60] Vourna P, Ktena A, Tsakiridis PE, Hristoforou E. A novel approach of accurately evaluating residual stress and microstructure of welded electrical steels. *NDT&E International*. 2015;**71**:33-42. DOI: 10.1016/j.ndteint.2014.09.011
- [61] Vourna P. An accurate method for determining residual stresses with magnetic non-destructive techniques in welded ferromagnetic steels. *Materials Science and Engineering*. 2016;**108**:1-5. DOI: 10.1088/1757-899X/108/1/012017
- [62] Ju J-B, Lee J-S, Jang J-I, Kim W-S, Kwon D. Determination of welding residual stress distribution in API X65 pipeline using a modified magnetic Barkhausen noise method. *International Journal of Pressure Vessels and Piping*. 2003;**80**:641-646. DOI: 10.1016/S0308-0161(03)00131-5
- [63] Yelbay HI, Cam I, Gür CH. Non-destructive determination of residual stress state in steel weldments by magnetic Barkhausen noise technique. *NDT&E International*. 2010;**43**:29-33. DOI: 10.1016/j.ndteint.2009.08.003
- [64] Stewart DM, Stevens KJ, Kaiser AB. Magnetic Barkhausen noise analysis of stress in steel. *Current Applied Physics*. 2004;**4**:308-311. DOI: 10.1016/j.cap.2003.11.035
- [65] Gauthier J, Krause TW, Atherton DL. Measurement of residual stress in steel using the magnetic Barkhausen noise technique. *NDT&E International*. 1998;**31**:23-31. DOI: 10.1016/S0963-8695(97)00023-6
- [66] Mitra A, Chen ZJ, Jiles DC. Nondestructive magnetic measurements in weld and base metals of service exposed Cr-Mo steel. *NDT&E International*. 1995;**28**:29-33. DOI: 10.1016/0963-8695(94)00002-2
- [67] Lachmann C, Nitschke-Pagel T, Wohlfahrt H. Characterisation of residual stress relaxation in fatigue loaded welded joints by X-ray diffraction and Barkhausen noise method. *Materials Science Forum*. 2000;**347-349**:374-381. DOI: 10.4028/www.scientific.net/MSF.347-349.374
- [68] Palanichamy P, Vasudevan M, Jayakumar T. Measurement of residual stresses in austenitic stainless steel weld joints using ultrasonic technique. *Science and Technology of Welding & Joining*. 2009;**14**:166-171. DOI: 10.1179/136217108X394753
- [69] Lu H, Liu XS, Yang JG, Zhang SP, Fang HY. Ultrasonic stress evaluation on welded plates with Lcr wave. *Science and Technology of Welding & Joining*. 2008;**13**:70-74. DOI: 10.1179/174329307X249405
- [70] Egle DM, Bray DE. Measurement of acoustoelastic and third-order elastic constants for rail steel. *The Journal of the Acoustical Society of America*. 1976;**60**:741-744. DOI: 10.1121/1.381146
- [71] Uzuna F, Bilge AN. Immersion ultrasonic technique for investigation of total welding residual stress. *Procedia Engineering*. 2011;**10**:3098-3103. DOI: 10.1016/j.proeng.2011.04.513
- [72] Tanala E, Bourse G, Fremiot M, De Belleval JF. Determination of near surface residual stresses on welded joints using ultrasonic methods. *NDT&E International*. 1995;**28**:83-88. DOI: 10.1016/0963-8695(94)00013-A

- [73] Woo W, Em V, Mikula P, An G-B, Seong B-S. Neutron diffraction measurements of residual stresses in a 50 mm thick weld. *Materials Science and Engineering A*. 2011;**528**: 4120-4124. DOI: 10.1016/j.msea.2011.02.009
- [74] Warren BE, Averbach BL. The effect of cold-work distortion on X-ray patterns. *Journal of Applied Physics*. 1950;**21**:595-599. DOI: 10.1063/1.1699713
- [75] Kromm A, Kannengiesser Th, Gibmeier J, Genzel Ch, van der Mee V. Determination of residual stresses in low transformation temperature (LTT-) weld metals using X-ray and high energy synchrotron radiation. *Welding in the World*. 2009;**53**:3-16. DOI: 10.1007/BF03266687
- [76] Cheng X, Fisher JW, Prask HJ, Gnäupel-Herold T, Yen BT, Roy S. Residual stress modification by post-weld treatment and its beneficial effect on fatigue strength of welded structures. *International Journal of Fatigue*. 2003;**25**:1259-1269. DOI: 10.1016/j.ijfatigue.2003.08.020
- [77] Monin VI, Gurova T, Castello X, Estefen SF. Analysis of residual stress state in welded steel plates by X-ray diffraction method. *Reviews on Advanced Materials Science*. 2009; **19**:172-175
- [78] Reynolds AP, Tang W, Gnaupel-Herold T, Prask H. Structure, properties, and residual stress of 304L stainless steel friction stir welds. *Scripta Materialia*. 2003;**48**:1289-1294. DOI: 10.1016/S1359-6462(03)00024-1
- [79] Gou R, Zhang Y, Xu X, Sun L, Yang Y. Residual stress measurement of new and in-service X70 pipelines by X-ray diffraction method. *NDT&E International*. 2011;**44**:387-393. DOI: 10.1016/j.ndteint.2011.03.003
- [80] Paradowska AM, Price JWH, Finlayson TR, Lienert U, Walls P, Ibrahim R. Residual stress distribution in steel butt welds measured using neutron and synchrotron diffraction. *Journal of Physics: Condensed Matter*. 2009;**21**:1-5. DOI: 10.1088/0953-8984/21/12/124213
- [81] Park MJ, Yang HN, Jang DY, Kim JS, Jin TE. Residual stress measurement on welded specimen by neutron diffraction. *Journal of Materials Processing Technology*. 2004;**155-156**: 1171-1177. DOI: 10.1016/j.jmatprotec.2004.04.393
- [82] Albertini G, Bruno G, Dunn BD, Fiori F, Reimers W, Wright JS. Comparative neutron and X-ray residual stress measurements on al-2219 welded plate. *Materials Science and Engineering A*. 1997;**224**:157-165. DOI: 10.1016/S0921-5093(96)10546-3
- [83] Ganguly S, Fitzpatrick ME, Edwards L. Use of neutron and synchrotron X-ray diffraction for evaluation of residual stresses in a 2024-T351 Aluminum alloy variable-polarity plasma-arc weld. *Metallurgical and Materials Transactions A*. 2006;**37A**:411-420. DOI: 10.1007/s11661-006-0012-3
- [84] Tra TH, Okazaki M, Suzuki K. Fatigue crack propagation behavior in friction stir welding of AA6063-T5: Roles of residual stress and microstructure. *International Journal of Fatigue*. 2012;**43**:23-29. DOI: 10.1016/j.ijfatigue.2012.02.003

- [85] Owen RA, Preston RV, Withers PJ, Shercliff HR, Webster PJ. Neutron and synchrotron measurements of residual strain in TIG welded aluminium alloy 2024. *Materials Science and Engineering A*. 2003;**346**:159-167. DOI: 10.1016/S0921-5093(02)00547-6
- [86] Woo W, Feng Z, Wang X-L, Brown DW, Clausen B, An K, Choo H, Hubbard CR, David SA. In situ neutron diffraction measurements of temperature and stresses during friction stir welding of 6061-T6 aluminium alloy. *Science and Technology of Welding & Joining*. 2007;**12**:298-303. DOI: 10.1179/174329307X197548
- [87] Staron P, Koçak M, Williams S, Wescott A. Residual stress in friction stir-welded Al sheets. *Physica B: Condensed Matter*. 2004;**350**:e491-e493. DOI: 10.1016/j.physb.2004.03.128
- [88] Daymond MR, Bonner NW. Measurement of strain in a titanium linear friction weld by neutron diffraction. *Physica B: Condensed Matter*. 2003;**325**:130-137. DOI: 10.1016/S0921-4526(02)01514-4
- [89] Turner R, Ward RM, March R, Reed RC. The magnitude and origin of residual stress in Ti-6Al-4V linear friction welds: An investigation by validated numerical Modeling. *Metallurgical and Materials Transactions B*. 2012;**43B**:186-197. DOI: 10.1007/s11663-011-9563-9
- [90] Withers PJ. Mapping residual and internal stress in materials by neutron diffraction. *Comptes Rendus Physique*. 2007;**8**:806-820. DOI: 10.1016/j.crhy.2007.09.015
- [91] Barbieri G, Soltani P, Kaciulis S, Montanari R, Varone A. IN792 DS superalloy: Optimization of EB welding and post-welding heat treatments. *Materials Science Forum*. 2016;**879**:175-180. DOI: 10.4028/www.scientific.net/MSF.879.175
- [92] Montanari R, Varone A, Barbieri G, Soltani P, Mezzi A, Kaciulis S. Welding of IN792 DS superalloy by electron beam. *Surface and Interface Analysis*. 2016;**48**:483-487. DOI: 10.1002/sia.5946
- [93] Angella G, Barbieri G, Donnini R, Montanari R, Richetta M, Varone A. Electron beam welding of IN792 DS: Effects of pass speed and PWHT on microstructure and hardness. *Materials*. 2017;**10**:1-19. DOI: 10.3390/ma10091033
- [94] Montanari R, Riccardi B, Volterri R, Bertamini L. Characterisation of plasma sprayed W-coatings on a CuCrZr alloy for nuclear fusion reactor applications. *Materials Letters*. 2002;**52**:100-105. DOI: 10.1016/S0167-577X(01)00375-5
- [95] Riccardi B, Montanari R, Casadei M, Costanza G, Filacchioni G, Moriani A. Optimisation and characterisation of tungsten thick coatings on copper based alloy substrates. *Journal of Nuclear Materials*. 2006;**352**:29-35. DOI: 10.1016/j.jnucmat.2006.02

Numerical Welding Simulation as a Basis for Structural Integrity Assessment of Structures: Microstructure and Residual Stresses

Kimiya Hemmesi and Majid Farajian

Additional information is available at the end of the chapter

<http://dx.doi.org/10.5772/intechopen.74466>

Abstract

The importance of welding process modeling is specifically related to the role of the induced welding residual stresses and distortions on the structural behavior of the components under service load. In the absence of reliable information on the magnitude and distribution of residual stresses, it is generally assumed that residual stresses are as high as the yield strength of the material that could lead to overconservatism in design and consequently economic challenges. The more exact the microstructure and residual stress or strain fields is predicted, the better one can judge the risk of structural damage, for example, the formation of fatigue cracks or initiation of failure. In this chapter, the application of finite element approach to the calculation of welding residual stresses is described through three different case studies. SYSWELD has been used for welding simulation. Residual stress measurements are carried out to determine the distribution of residual stresses in three orthogonal directions, on the surface and in the bulk of the material. The numerical results are compared directly with the measured data. The overall aim is to evaluate the use of finite element approach in the accurate calculation of residual stress states for use in the structural integrity assessments.

Keywords: welding simulation, residual stresses, finite element method (FEM), X-ray diffraction, neutron diffraction

1. Introduction

In fusion welding, concentrated heat is injected into the joint locally and is dissipated into the weldments, leading to an inhomogeneous temperature field in the welded material.

The maximum temperature in this time-dependent field reaches beyond the melting point in the weld pool, and the minimum value is the ambient temperature being reached after cooling down. Within this temperature field and due to the temperature-dependent physical and mechanical properties, an inhomogeneous thermal stress field is generated. The thermal stresses can either be accommodated elastically or lead to a stress state in which plastic deformations would be inevitable. There is another source of plastic deformation, which is induced during solid-state phase transformations if phase transformation occurs. As a result of the inhomogeneous plastic deformation during welding, some regions do not fit into the space available, and due to geometrical compatibility, a residual stress field arises.

The reliable characterization of welding residual stresses in structural components has been widely considered in many research communities. Tensile residual stresses which are present in welds could potentially decrease the tolerance of the component against applied external loads. In integrity assessments, the interaction between load and residual stresses is taken into account by using a couple of conservative approaches [1]. In order to predict the more realistic service life of welded components, it is necessary to be aware of the residual stress fields, particularly in the critical crack initiation sites. Over the past few decades, a large number of researches have been devoted to the experimental and numerical determination of welding residual stresses. Recent advances in both simulation and measurement of weld residual stresses have provided the possibility to describe the residual stresses. However, owing to the different thermal, metallurgical, and mechanical complexities and the interaction between them, there still exist a number of uncertainties in the accurate calculation and measurement of residual stresses. On the other hand, it is extremely difficult to quantify separately the effects of several variables and parameters.

1.1. Computational welding mechanics

Experimental analysis for the determination of the residual stress fields in welds by means of nondestructive methods requires complementary diffraction instruments [2]. Such studies are very costly, and because of the limitation of the volume and mass of the investigated object, they could just provide one in best case information about a portion of the whole residual stress field in a large structure. A scientific and engineering approach to solve this problem is the application of numerical methods for describing the development of residual stresses and studying their behavior under different mechanical and thermal loads.

Welding as a multi-physics problem is one of the most complicated processes from the modeling point of view. Different aspects, namely the arc physics, transient heat transfer, conductivity, fluid flow, phase transformations, grain size and deformations must be taken into account into the model. The first works on application of the numerical analysis of welds and the behavior of the material during welding are those of Boulton [3] and Rosenthal [4]. Since then, many models for the description of the heat source have been developed, which are all mentioned in the literature survey by Goldak [5].

In most models, which are used for the calculation of residual stress and distortion, the real heat input is simulated via an equivalent substitute heat source moving in the direction of welding. The fluid dynamics in the weld pool are almost always not included.

Residual stress and distortion are strongly influenced by the temperature-dependent plasticity. In **Figure 1**, the thermomechanical processes for the development of welding stresses are schematically illustrated. Here in this model from Radaj [6], the plastic zones in front and a linear heat source in a quasi-stationary temperature field are shown. The drawn parabola-like curve separates the heated front area which is due to the thermal stresses under compression from the rear region which is under tensile stresses. The zone of elastic unloading is located between the two areas. The cyclic plasticity at the shown locations in the base material, the heat affected zone and the weld during the heating and cooling phases show how the residual stresses develop. Point 1 undergoes elastic compressive stress, and at point 2, a plastic deformation occurs after reaching the compressive yield strength before this point is elastically relieved at point 3. The permanent elongation by compression at point 3 could lead to tensile residual stresses after cooling. Points 4 and 5 experienced tensile stresses during cooling due to the shrinkage restraint.

The remaining strain at point 5 may indicate that after reaching room temperature, compressive residual stresses may be present. Point 6 would have a mechanical load cycle as point 5, if it would not have been so close to the heat source. Point 7 is on the weld center and is only subjected to elasto-plastic tensile stresses. It is understandable that the temperature-dependent spatial and temporal process and material modeling determine the accuracy of the residual stress and distortion calculations.

Computational welding mechanics is an engineering subject concerned with the mechanics and the material behavior during welding. In research and applications, the different welding processes, the microstructures resulting in the weld and their mechanical properties in terms of deformability, strength, and toughness and the structural behavior of welded components are to be considered for an advanced fitness-for-service assessment of welded components.

The accuracy of the predicted results in the calculation of residual stresses as a complex non-linear problem is influenced by several assumptions and simplifications. Nevertheless, the experimental measurement of welding residual stresses involves a significant range of uncertainties. Since both numerical and experimental approaches involve inevitably their own limitations, it is necessary to apply these methods in combination with each other.

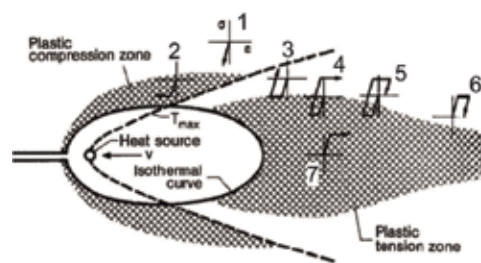


Figure 1. Cyclic plasticity in the weld, heat-affected zone and the base material and the formation of welding residual stresses [6].

With the development of modern high speed computers, process modeling has become a powerful tool for controlling and optimizing of different process parameters. Nowadays, finite element method has contributed in process simulation extensively. In the context of weld computational mechanics, modern software infrastructures, that is, the physics, mechanics, materials science, mathematics and numerical algorithms have been enriched enough to allow complex calculation of welded structures [7]. A proper FE model for welding simulation involves advanced aspects such as definition of the heat source, material phase transformations, temperature-dependent thermophysical and mechanical properties and material hardening behavior. But the key issue in this regard is to understand the underlying theory well enough. In the study described here, it has been tried to handle as much as possible the various assumptions and simplifications in the prediction of welding residual stresses.

In this chapter, three fusion weld case studies are described with focus on different geometries, single or multiple pass welds and finally different types of base materials particularly with regard to metallurgical behavior and hardening behavior. As the first case study [8], under the support of German Research Foundation (DFG) [9], a tubular specimen made of S355J2H structural steel was utilized for the weld residual stress assessments. The specimen was manufactured under closely controlled conditions. After the preparations, a single-pass dummy weld without filler material was created in the specimen. Appropriate material characterization was performed on the base metal under static and cyclic loading conditions. In the case studies two [10] and three [11], the results of a scientific community, the international *Network on Neutron Techniques standardization for Structural Integrity* (NeT) will be discussed. This network consists of 15 European-based member research institutes, universities and industries, which meet twice a year and discuss the results of defined round-robin tasks on welding simulation and experimental residual stress measurement techniques. Within the framework of NeT round robin, case study two focuses on a single bead on plate made of austenitic stainless steel and finally case study three deals with the multipass welding of Inconel.

Nickel alloy similar to stainless steel is a face-centered cubic, which shows no phase transformation during cooling from its melting temperature down to the room temperature. Thus, cooling rate for both stainless steel and nickel alloy is of less importance. However, for nickel alloys, particularly the precipitation hardened alloys, the composition-related metallurgical effects should be taken into account. Nickel alloys compared with stainless steels have lower thermal expansion coefficient, which may cause less distortion problems. The procedures for welding of stainless steels and nickel alloys are relatively similar. Sequentially, coupled thermal-mechanical analyses were performed in both task groups. The accuracy of predictions for the transient temperature field, welding residual stresses, equivalent plastic strains, and so on was then calibrated based on experimental measurements. The achievements and results could be then used as lessons for further numerical simulation. This involves the global calibration of the heat input on the basis of the thermocouple responses and detailed determination of the heat source parameters by matching the weld fusion boundaries to real weld cross sections.

Different stages of calculation were compared with experimental tests by taking into account the limitations and uncertainties of the measurements. In the thermo-metallurgical



Figure 2. Simulation studies and residual stress measurements: cooperation in NeT (left), investigations within the project by German Research Foundation (DFG) (right).

phase, the transient temperature history during the welding process was calibrated by means of the measured thermocouple profiles. Furthermore, the fusion boundary of the weld bead was controlled by the cross-sectional macrograph of the specimen. Once an accurate thermo-metallurgical solution is obtained, one can study the mechanical aspect of the weld calculation. One of the most important focuses on the mechanical solution as the next step is to determine the best explanatory material hardening model. Since the predicted residual stresses are sensitive strongly to the high-temperature mechanical properties and especially to the cyclic hardening parameters, it is important to consider all the possible material-related simulation variables. The accuracy of calculated residual stresses was then controlled with measured data in order to optimize the choices for different variables. Since it is preferred to make use of through-thickness stress profiles for structural integrity and defect tolerance assessments [1], both X-ray and neutron diffraction measurement techniques were used in order to describe the surface and depth profile of welding residual stresses.

For all the calculations, the FEM weld-specific program SYSWELD was used as simulation tools (**Figure 2**).

2. Numerical studies of welding residual stresses

The accurate structural integrity assessment of welded structures or components requires the designers to be aware of the existing welding residual stress field within the material. A complex process such as welding could be described by means of both numerical and experimental techniques.

In this chapter, the applicability of FEM to the simulation of welding process is being examined. Three-dimensional models were applied within the commercial software package SYSWELD 8.5 to calculate numerically the inevitable residual stress field, which is produced as a consequence of nonuniform heating and cooling. A coupled thermo-metallurgical simulation was then conducted and the results of which included temperature history and phase proportions. These were then used as the input for further mechanical analyses within the uncoupled simulation technique. Using this technique, though the insignificant dimensional changes as well as the mechanical work are neglected, the accuracy of the results is kept to a high level. Different aspects of numerical welding simulation are explained in detail in Ref. [8].

2.1. Case study 1: S355J2H single bead on tube

On the basis of the well-documented experimental results on tubular specimens made of S355J2H in the project DFG FA992/1-1 [9], extensive numerical studies on welding simulation were performed on this material. The key modeling issues were as follows: heat source representation, solid-state phase transformation kinetic, material hardening laws and temperature-dependent material behavior. In the thermo-metallurgical phase, the transient temperature history during the welding process was calibrated according to the measured responses from the thermocouples along with the cross-sectional macrographs from the weld fusion boundaries. Once an accurate thermo-metallurgical solution was obtained, the mechanical aspects of the welding simulation were considered. Temperature dependent material properties together with cyclic hardening parameters are two important material related simulation variables which must be taken into account since they may affect strongly the predicted residual stresses. The accuracy of the calculated residual stress field was then validated by means of X-ray and neutron diffraction measurements.

2.1.1. Welded specimens

The tubular specimens out of structural steel S355J2H had a length of 250 mm with the outside and inside diameter of 56 and 36 mm, respectively. The base metal before welding had been heat treated for 30 min at 600°C under shielding gas in order to relieve the existing machining-induced residual stresses. The samples were produced by means of Tungsten Inert Gas (TIG) welding without filler material (**Figure 3**). The arc voltage, welding current and welding speed were set to 12 V, 250A and 15 cm/min, respectively, providing a total input energy of 7.2 kJ/cm. In this way, a 10 mm wide and 2.5 mm deep weld bead was produced on every tube. NiCr-Ni thermocouples were used to measure the temperature history at every 90° around the weld toe (Q1-Q4) [12].

2.1.2. Plasticity and material hardening model

Von Mises yield function is considered in this work as the criterion to describe where the plastic deformation begins. Besides that, the constitutive behavior of the material and the respective hardening model must be defined properly in order to preserve the accuracy of the calculated residual stresses. For simplicity, a single-element FE analysis technique was then applied in order to investigate the influence of the chosen hardening model on the predicted stress-strain responses of the material under mechanical loading conditions. In this regard, the calculation



Figure 3. TIG welding of the tubular specimens with temperature measurements [8].

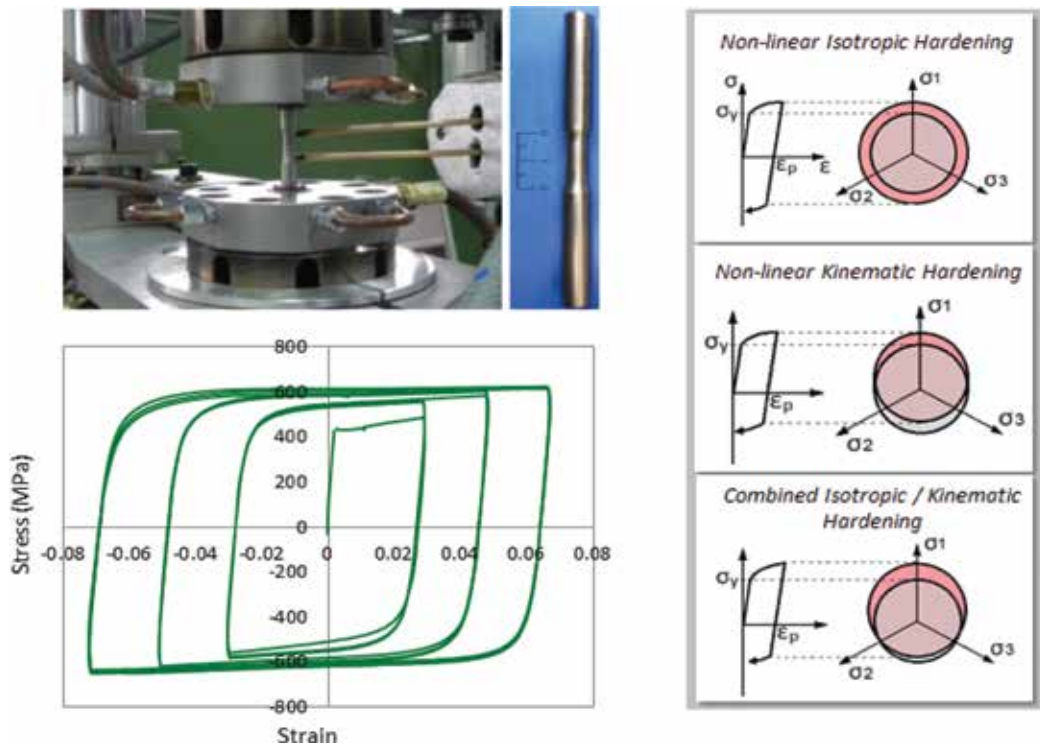


Figure 4. Low cycle fatigue test results of S355J2H at $\Delta\epsilon = 0.06, 0.1$ and 0.14 (left), different types of hardening model [8].

results under symmetric strain-controlled cyclic loading were compared with the obtained stress-strain responses from the isothermal low cyclic fatigue tests at constant amplitude. Three process-related strain ranges, namely 6%, 10% and 14% were chosen for the LCF tests as shown in **Figure 4**.

SYSWLED supports the modeling of the nonlinear kinematic hardening behavior in the form of Armstrong-Frederick combined hardening model [13] under the isothermal and monophasic condition:

$$\hat{\sigma}(\epsilon_{eq}^p) = \hat{\sigma}_0(\epsilon_{eq}^p) + \frac{C}{\gamma}(1 - e^{-\gamma\epsilon_{eq}^p}) \tag{1}$$

where $\hat{\sigma}$ represents $\sigma - \sigma_0$ and $\hat{\sigma}_0$ is the yield stress at zero plastic strain, ϵ_{eq}^p is the equivalent plastic strain and C and γ are material kinematic hardening parameters (supported only as a single pair for this model). Isotropic hardening component that defines the expansion of the yield surface as a function of accumulated plastic strain is represented through the $\hat{\sigma}_0$ term. Meanwhile, the kinematic hardening component is introduced to the model to describe the translation of the yield surface in the stress space.

In order to define the kinematic hardening parameters, the model could be fitted in different ways to either monotonic or uniaxial cyclic stress-strain curves. Two case studies were considered in this work. In case 1, whether a pure kinematic or a combined isotropic-kinematic hardening model is implemented, the kinematic behavior is assumed to be linear. In this regard, the maximum plastic strain for defining the monotonic true stress versus plastic strain response was set to 100%. In case 2, a nonlinear kinematic hardening behavior was taken into account for both pure kinematic or combined hardening models. In this case, the first cyclic response of the material taken from the LCF test data was used in order to calibrate the respective model

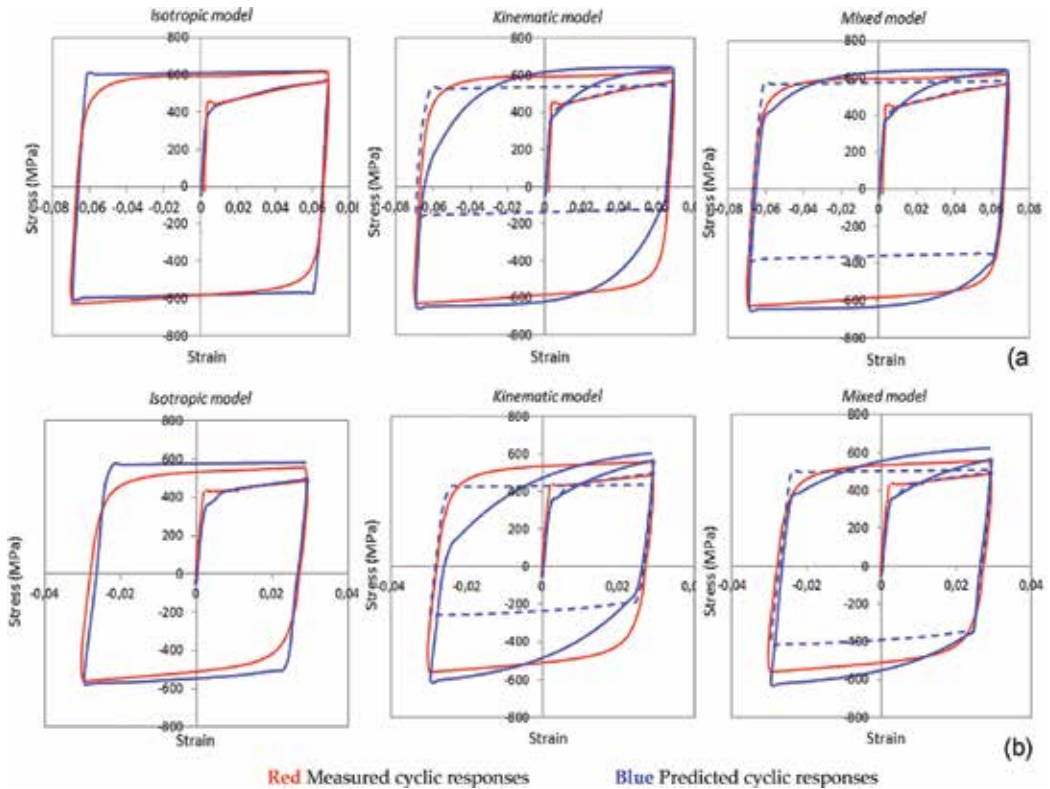


Figure 5. Comparison between the measured and predicted stress-strain responses of S355J2H during the first load reversal at room temperature for strain ranges $\Delta\epsilon=0.14$ (top) and $\Delta\epsilon=0.06$ (bottom). Continuous and dashed lines are related to case studies 1 and 2 for finding the kinematic parameters [8].

parameters through the fitting procedure. The total strain range in the respective LCF test was set to 14%. Being a one-pass weld is the cause for choosing the first load reversal as for the fitting procedure. In this case, any extra cyclic hardening is ignored. **Figure 5** shows the predicted responses at two of the strain ranges (6 and 14%) for simple isotropic, pure kinematic and combined isotropic-kinematic hardening models. Red and blue plots in **Figure 5** represent the measured and predicted responses, respectively. The dashed or continuous blue plots refer back to the used fitting approaches for defining the kinematic hardening parameters. In this regard, dashed blue lines and continuous blue line represent case 1 and case 2, respectively. As can be seen in **Figure 5** using the pure isotropic hardening model, though the Bauschinger effect is neglected, the predicted and measured monotonic responses as well as the peak stress values of the cyclic responses agree reasonably well except that the predicted yielding points during the cyclic responses are sharper than the measured ones. In case of using a pure kinematic hardening model, the reversed yielding points were predicted to be much lower than the measured ones due to the incorporation of the Bauschinger effect. In this regard, the nonlinear kinematic hardening model gives obviously better results in predicting the shape and peaks of the hysteresis loops but poorer results in predicting the monotonic stress-strain responses of the material rather than linear one. It should be noted that the level of peak stresses predicted by the linear kinematic hardening model depends strongly on the predefined maximum plastic strain in the monotonic mechanical property. By using the combined isotropic-kinematic hardening model with a 50% isotropic proportion, the reversed yielding points were improved significantly comparing with the pure kinematic cases. Even in the case of combined hardening, if the kinematic model parameters are obtained by fitting to the cyclic stress-strain curves, the predicted monotonic responses do not conform to the experimental curves though the cyclic responses match well enough. Indeed, matching both monotonic and cyclic responses is difficult, which could influence the final results differently depending on the case of study.

2.1.3. Residual stress results

The calculated and measured residual stress fields in the axial and hoop directions at 180° from the weld start point (Q3) are shown in **Figure 6**. As can be seen, the numerical results conform very well the experimentally measured data. Residual stress measurements by means of neutron diffraction (ND) were conducted at Helmholtz-Zentrum Berlin (HZB).

To be able to interpret the formation of welding residual stresses numerically, different aspects of the simulation need to be explained in detail. It is obvious that during welding every material point in the specimen is experiencing different thermal history depending on its location relative to the welded area. In this regard, the evolution of different material phases, cumulative and equivalent plastic strains and finally the welding residual stresses are investigated through the numerical analysis at different positions with respect to the welded area (**Figure 7**). For instance, at node-1, which is located within the welded area, the temperature goes beyond the melting point during heating and thus austenite transformation occurs substantially since the maximum temperature exceeds the austenitization finish temperature (Ac3).

Then, the material cools down from the maximum temperature and the austenite starts to transform into bainite and martensite depending on the cooling rate. The evolution of different

phases during heating and cooling is shown in **Figure 8a**. In **Figure 8b**, the evolution of the axial and hoop residual stresses, the cumulative plastic strain and the equivalent plastic strain are shown by dividing the total process time into seven smaller time intervals. During time intervals 1 and 2, the moving torch does not yet reach Q3; thus, the material at node-1 undergoes some tension and compression elastically. Once the welding torch reaches Q3, the local temperature starts to increase during the time interval 3 and the material undergoes expansion-induced compressive stresses. Since yielding occurs in this period, plastic strain begins to accumulate in the material. In the interval 4 during which the temperature goes beyond 1300°C, the stress components and the cumulative plastic strains disappear since the temperature exceeds the material annealing temperature, which was previously set to 1300°C. Unexpectedly, the equivalent plastic strain is retained as can be seen in **Figure 8b**. Time interval 5 represents the cooling phase from annealing temperature down to bainitic transformation temperature. In this period, tensile stresses appear due to the shrinkage of the material at the point of interest. Meantime, plastic strains start to accumulate again in this period. By further cooling in the time interval 6, austenite starts to transform to bainite since the temperature has dropped below the bainitic transformation temperature. This type of transformation is associated with the decrease of density, which causes volume expansion and thus local compression in the material. Below 420°C in the time interval 7, rest of the austenite phase transforms into martensite, which is associated with more volume increase and consequently the compressive stresses increase. During the time intervals 6 and 7, the strain hardening of the material vanishes gradually due to the hardening recovery phenomena caused by austenite to ferrite transformation.

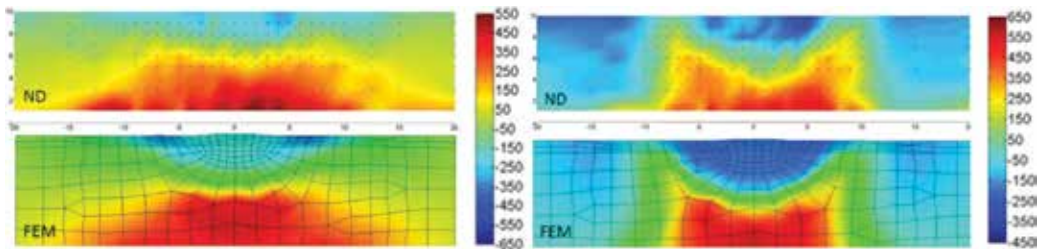


Figure 6. Comparison of the calculated axial (left) and hoop (right) residual stress fields at Q3 with the ND-measurements [8].

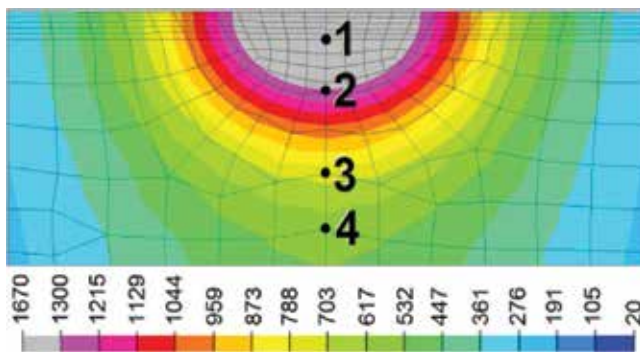


Figure 7. Different representative material zones in the weld cross-section from the FE model at Q3 [8].

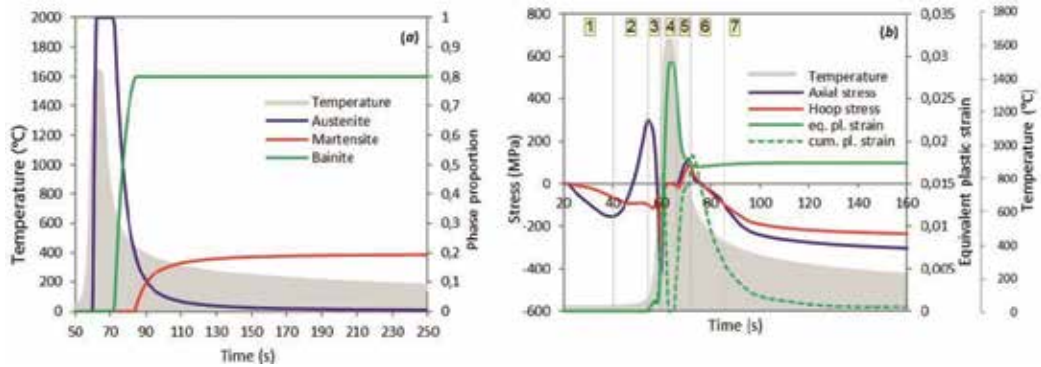


Figure 8. Evolution of different material phases (a) and residual stresses, cumulative and equivalent plastic strains (b) at node-1 with respect to the relevant temperature history [8].

The situation at nodes 2 to 4 differs from what is explained at node-1 regarding the formation of thermal stresses or plastic strains, which is discussed in detail in Ref. [8].

2.2. Case study 2: 316 L single bead on plate

A single weld bead on plate made of austenitic stainless steel was chosen as the benchmark problem for NeT Task Group 1 (TG1) in order to examine the influence of different simulation variables on the accuracy of predicted residual stresses. The specimen geometry and its boundary condition during welding are shown in **Figure 9**. The plate was 17 mm thick and was 200 mm and 150 mm in length and width, respectively. A single TIG weld bead with the same material as the base metal and a width of 7 mm was laid on the surface of the plate. The heat input and welding speed were set to 633 J/mm and 2.27 mm/s, respectively. Both base material and weld metal were characterized using temperature-dependent monotonic and cyclic mechanical tests. For calibration reason, a number of thermocouples were applied to the specimen top and bottom surfaces, along the weld line and as close as possible to the weld. After welding, residual stress measurements were also performed at different locations of the plate by using different techniques such as hole-drilling, contour method and neutron diffraction technique [10]. In TG1, the Bayesian average of the residual stress results from different measurements was used for the calibrations.

2.2.1. NeT TG1 simulation results

A three-dimensional finite element model was developed, and the welding simulations were conducted through sequentially coupled thermal-mechanical solutions. A moving heat source with the Goldak [14] formulation was applied to the model in order to simulate the movement of the welding torch. The gradual material deposition was also included in the model. The annealing scheme was incorporated in the model by considering a melting temperature of 1400°C. In this way, the material history including stress and strain as well as the strain hardening would be eliminated above the annealing temperature.

The heat input energy was calibrated first according to the responses of nine thermocouples [10]. After that, parameters of the heat source were adjusted according to the cross-sectional macro-graphs of the weld in order to match the boundaries of the calculated melted area with the real condition (**Figure 10**).

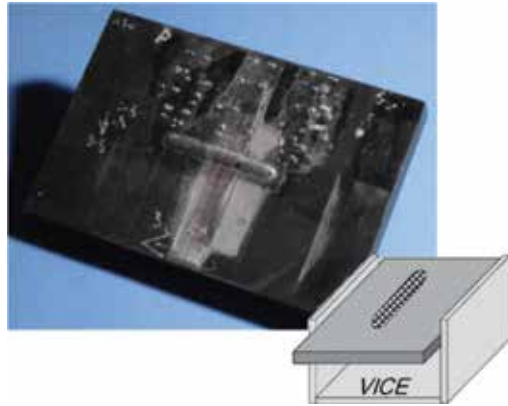


Figure 9. NeT TG1 specimen.

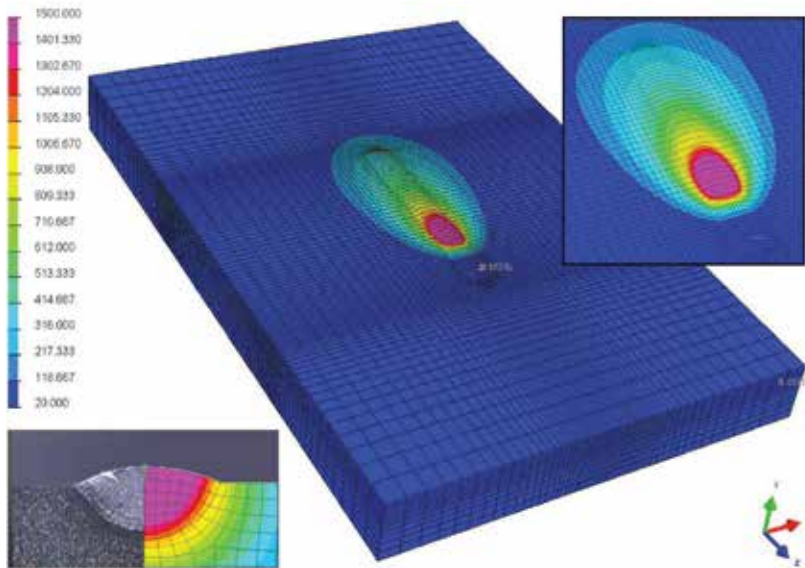


Figure 10. NeT TG1 weld bead on plate simulation.

One of the most important features of NeT TG1 was to comprehensively investigate the influence of material hardening model on the final field of predicted residual stresses. Of course the choice of the hardening model depends strongly on the used material. In this study, isotropic, kinematic and combined isotropic-kinematic hardening models were examined for the welding simulations. For determining the material kinematic hardening parameters, different fitting strategies were adopted, which have been described comprehensively in Ref. [10]. **Figure 11** shows the through thickness variation of transverse residual stresses in the mid-plane. As can be seen, the use of the isotropic hardening model in the welding simulation of the austenitic stainless steel has caused over conservatism in the predicted residual stresses. Combined isotropic-kinematic hardening model has given the best agreement with the experimental results.

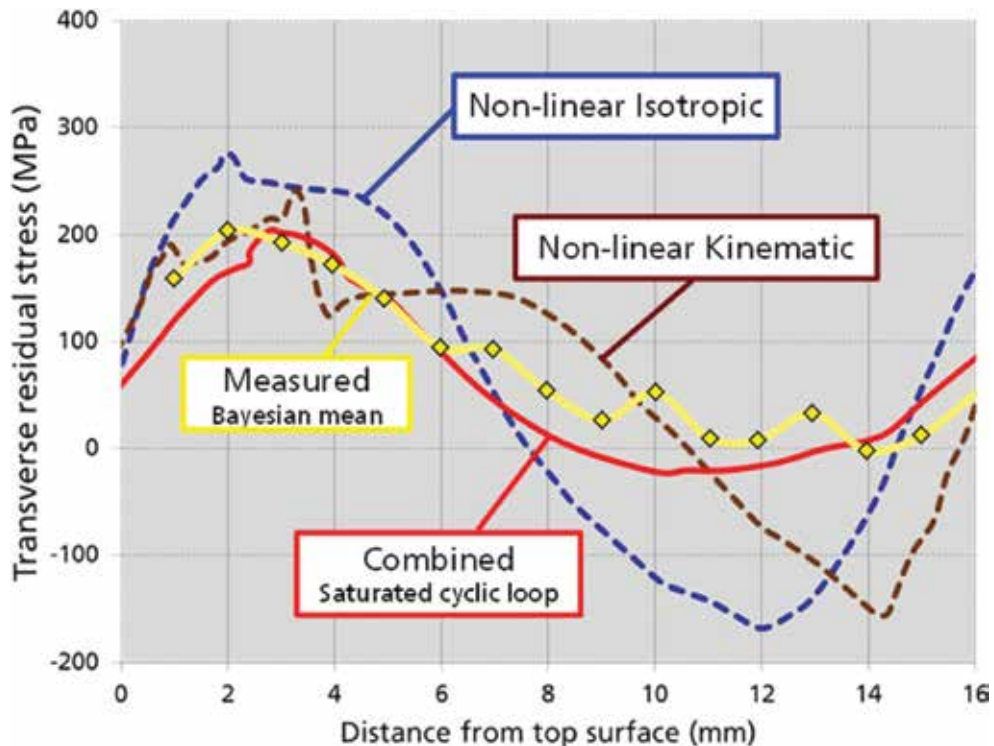


Figure 11. Comparison between the residual stress results using different material hardening models [11].

It should be noted that the yellow curve in **Figure 11** is representative of the Bayesian average of different measured data obtained from different techniques, which were comparable to each other. The combined hardening model in this case is optimized by matching to the saturated cyclic response of the material. In this project, it was observed that other mechanical solution variables than temperature-dependent material properties and material hardening behavior have minor influence on the final simulation results. Experiences and lessons of NeT TG1 were then collected together as a simulation strategy for the future works and task groups. These lessons are summarized as follows:

- In welding simulation, before proceeding to mechanical simulation, a verified global heat input and a calibrated heat source are absolutely necessary.
- The use of kinematic and combined hardening models or preferably elasto-viscoplastic material constitutive behavior is recommended for the welding simulations.
- The used material constitutive model for the weld metal could differ from that of base material.

2.3. Case study 3: nickel alloy three-pass bead-in-slot

A three-pass slot weld in nickel alloy 600 plate has been chosen as the case study of NeT Task Group 6 (TG6). The dimensions of the plate are 200 mm × 150 mm × 12 mm. The slot is 76 mm

long and 5 mm deep, which was filled with filler material made of alloy 82 (or 182) using the TIG welding process. The welding voltage ranges from 10 to 13 V depending on the weld pass number. Welding current and speed were set to 220 A and 70 mm/min for every pass. The specimen was constrained weakly to allow for free deformations. The multipass welding condition in this study provides complex thermomechanical loading condition, which requires more detailed assumptions and considerations regarding the cyclic behavior of the material. As noted in the NeT TG6 simulation protocol [11], the residual stress measurement is more challenging for the nickel-based alloys as compared with the stainless steel AISI 316. The objective of the NeT TG6 round robin is to promote parallel simulations and measurements in order to accurately predict the welding residual stresses in the slot welds.

2.3.1. Experimental work

A wide range of experiments were performed within the activities of NeT TG6 to support the numerical simulations:

2.3.1.1. Material characterization

The chemical composition, temperature-dependent tensile monotonic and uniaxial cyclic properties of alloy 600 and alloy 82 were determined in the NeT TG6 measurement round robin. Thermomechanical tests using the Gleeble testing machine were performed to determine the properties of the material in the heat-affected zone. LCF test results for alloy 600 at room temperature and 700°C are shown in **Figure 12**. For alloy 182 (weld metal), it was observed that the cyclic hardening rate is lower than the AISI 316 L. Thus, the combined isotropic-kinematic hardening model could be replaced simply with the pure kinematic one. Based on the test results, although the 0.2% proof stresses for the base material and the weld

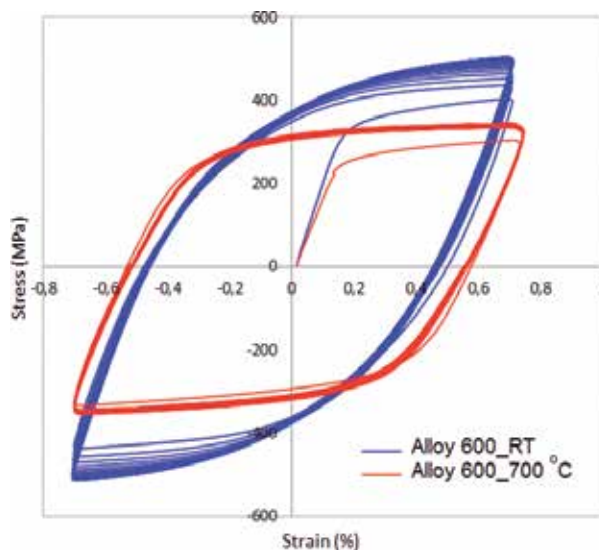


Figure 12. LCF test results for alloy 600 at room temperature and 700°C ($\Delta\varepsilon_{\text{tot}} = 1.5\%$).

metal are similar, their work hardening rates are different. Combined hardening (Lemaitre-Chaboche) or pure nonlinear kinematic hardening models were then fitted to the available experimental data in order to determine the model parameters.

2.3.1.2. Hardness measurement

Transverse hardness mapping after producing every single pass is shown in **Figure 13**. As can be seen, the hardness of the weld area is lower than base material.

2.3.1.3. Temperature measurement

A total number of 10 thermocouples were attached to the specimen top and bottom surfaces and close to the weld line. The global heat input and dwell times could be then calibrated on the basis of thermocouples responses. The specimen geometry and the configuration of thermocouples are shown in **Figure 14**.

2.3.1.4. Residual stress measurement

Three sets of neutron diffraction measurements, one set of X-ray diffraction as well as one set of contour method measurements were planned in order to define experimentally the residual stress field in the material. Different sets of measured residual stresses agree well with each other.

2.3.2. Numerical simulations

The simulation methodology used for the welding simulation of nickel alloys is similar to that of AISI 316 L. Lessons and recommendations of NeT TG1 are supposed to be applied in the

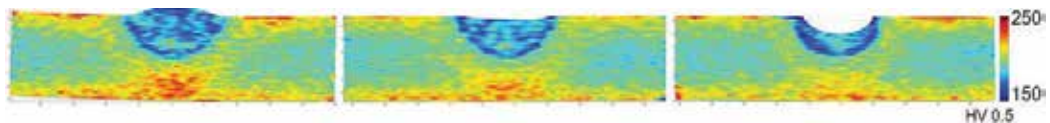


Figure 13. Measured hardness field after finishing each pass.



Figure 14. Specimen geometry and location of the thermocouples close to the slot.

TG6 solutions. Some of these recommendations were mentioned in Section 2.2.1. A preliminary finite element thermal calculation has been performed in Fraunhofer IWM as one of the simulation partners in NeT TG6 round robin. **Figure 15** depicts the comparison between the calculated temperature history and the response of a mid-length thermocouple called TC2.

The agreement between the results is quite well. The criterion for an accurate thermal simulation (as the basic prerequisite for residual stress calculation) is to achieve an agreement with the mid-length thermocouple response within 10%. On the other hand, the calculated melting boundaries including the cross-sectional area and shape of the fusion zone should match the real condition within $\pm 20\%$. According to **Figure 16**, the calculated fusion boundaries match quite well to the real weld cross section illustrated in the macrographs.

The variation of calculated residual stress components along line BD (through the thickness) and B2 (across to the weld) are shown in **Figure 17** in comparison with the measured results. These results are obtained from neutron diffraction measurements. As can be seen, there exists a reasonable agreement between the calculations and measured results. The existing discrepancy might be attributed to the high-temperature annealing behavior, which is neglected in this study.

As shown in **Figure 17** (top), the maximum amount of longitudinal residual stress along line BD is predicted to be close to the bottom surfaces. According to **Figure 17** (bottom), relatively high tensile residual stresses exist in the weld area and HAZ. A peak value of 500 MPa in the longitudinal direction was observed at the weld toe, which could increase the probability of crack formation at the stress concentration sites, particularly because the most serious cracking problem with nickel alloys is hot cracking in either the weld metal or close to the fusion line in the HAZ with the latter being the more frequent [11].

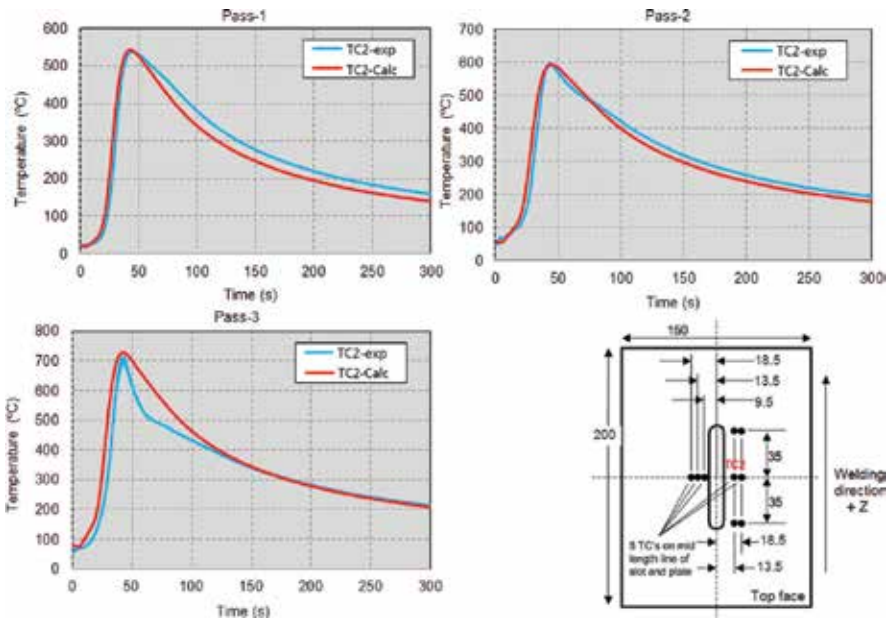


Figure 15. Experimental and numerical temperature histories for three-pass slot weld at mid-length thermocouple TC2.

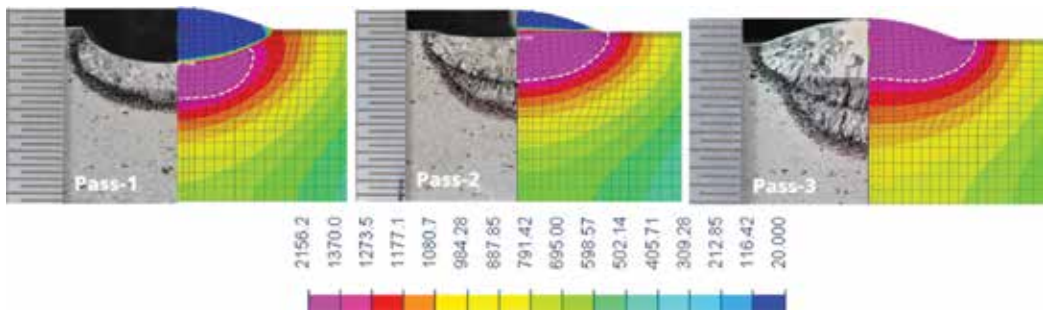


Figure 16. Calculated temperature contour plots of three weld passes compared with the real fusion boundaries.

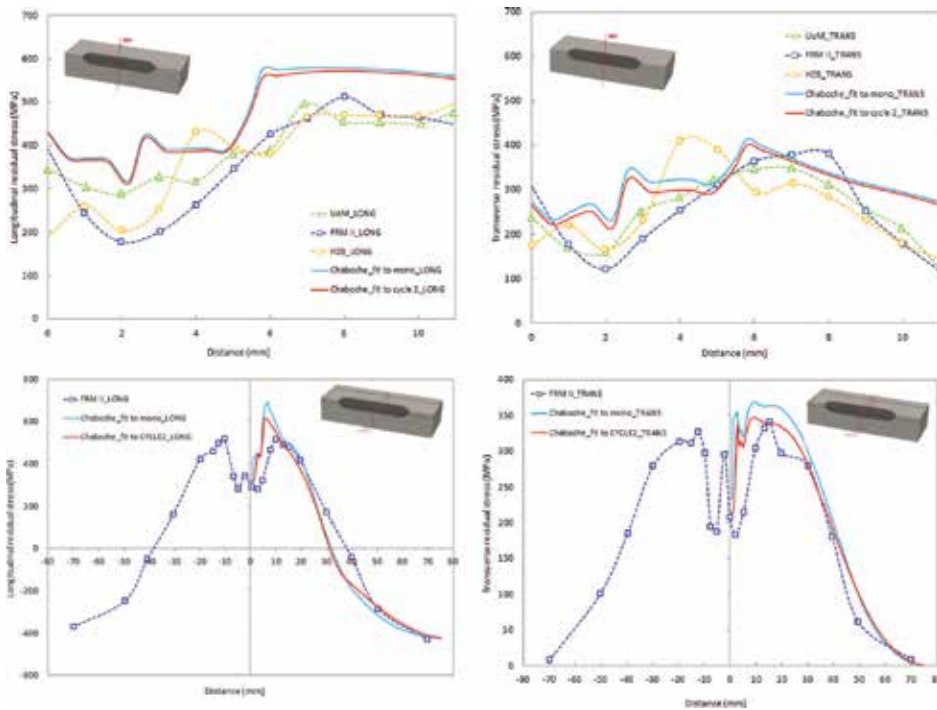


Figure 17. Comparison between the measured and calculated residual stress components on lines BD (top) and B2 (bottom).

3. Conclusions

In this chapter, three welding simulation case studies were reviewed. As the first case study, the numerical analysis of welding residual stresses in single bead tubular specimens made of structural steel S355J2H was studied. In case study 2, the NeT Task Group 1 was reviewed which focuses on single-pass weld bead on plate made of AISI 316 L and for case study 3, the NeT Task Group 6 was considered which is about the three-pass slot welds of nickel alloys. There exist very well documented experimental results on tubular specimens made of S355J2H in the project DFG FA992/1-1. On the other hand, NeT projects include a

wide range of experimental measurements parallel to its advanced simulation programs. The goal is to develop a comprehensive simulation methodology for the prediction of residual stresses under the assistance of precise measurement techniques. Based on the results and achievements, FE simulation could be applied as a powerful tool for predicting the welding residual stresses required for the integrity assessments. The summaries of all these efforts have been already released in terms of a couple of recommendations. Exact thermal solutions, use of advanced material hardening models and including high-temperature annealing effects are some of the most important items out of those recommendations.

The key conclusions and findings in this period are listed as follows:

1. Welding residual stresses within the tubular welded joint could be accurately determined by means of the numerical simulation approach considering the phase transformations, microstructure- and temperature-dependent mechanical properties, transformation-induced plasticity and recovering of strain hardening during transformation.
2. Combining the residual stress measurement results from X-ray and neutron diffraction over the whole cross section of welds showed a sharp gradient in the welding residual stress profile from top surface toward the material bulk.
3. Based on the simulations of the tubular welds, the material in the weld area undergoes compressive stresses due to the $\gamma \rightarrow \alpha$ transformation-induced expansions during cooling.
4. For the material S355J2H, isotropic hardening model seems to be suitable for predicting welding residual stresses.
5. In welding simulation, before proceeding to mechanical simulation, a verified global heat input and a calibrated heat source is absolutely necessary.
6. The use of kinematic and combined hardening models or preferably elasto-viscoplastic material constitutive behavior is recommended for the welding simulation of stainless steel and Inconel.
7. The used material constitutive model for the weld metal could differ from that of base material.

Acknowledgements

This contribution was partially supported by the German Research Foundation (Deutsche Forschungsgemeinschaft – DFG) as part of the projects DFG FA992/2-1 “Numerical description of the behavior of welding residual stress field under multiaxial mechanical loading” and DFG FA992/2-2 “Numerical Incorporation of the Damaging Effects of Residual Stresses in the Multiaxial Fatigue Assessment of Welded Components and Structures”. The respective residual stress measurements were done at the Helmholtz-Zentrum Berlin (HZB) and the Forschungs-Neutronenquelle Heinz Maier-Leibnitz (FRM II) in Munich, Germany. The authors would like to thank deeply for the support. For those experiments conducted within the activities of NeT (Network on Neutron Techniques standardization for Structural Integrity) round robin, the authors would like to use the opportunity to express their gratitude to everyone who was involved in this fruitful collaboration.

Author details

Kimiya Hemmesi and Majid Farajian*

*Address all correspondence to: majid.farajian@iwf.fraunhofer.de

Fraunhofer Institute for Mechanics of Materials IWM, Germany

References

- [1] R6. Assessment of the Integrity of Structures Containing Defects. Br. Energy. Revision 4; 2013
- [2] Farajian M, Nitschke-Pagel T, Wimpory RC, Hofmann M, Klaus M. Residual stress field measurements in welds by means of X-ray, synchrotron and neutron diffraction. *Journal of Materials Science and Engineering Technology*. 2011;**42**(11):996-1001
- [3] Boulton NS, Lance Martin HE. Residual stresses in arc-welded plates. *Proceedings of the Institution of Mechanical Engineers*. 1936;**133**:295-347
- [4] Rosenthal D. Mathematical theory and heat distribution during welding and cutting. *Welding Journal*. 1941;**20**(5):220-234
- [5] Goldak JA, Akhlaghi M. *Computational Welding Mechanics*. New York, USA: Springer; 2005. ISBN-10:0-387-23287-7
- [6] Radaj D. *Eigenspannungen und Verzug beim Schweißen, Rechen- und Messverfahren*. Fachbuchreihe Schweißtechnik. Düsseldorf: DVS-Verlag GmbH; 2000
- [7] Goldak J. Web based simulation of welding and welded structures. CWA Conference. 2013
- [8] Hemmesi K, Farajian M, Boin M. Numerical studies of welding residual stress field in tubular joints and the related experimental investigations by means of X-ray and neutron diffraction analysis. *Materials and Design*. 2017;**126**:339-350
- [9] Farajian M. Residual stress relaxation in high strength steel welded joints under multi-axial loading. DFG-FA992/1-1 Final Report. 2015
- [10] Smith MC, Smith AC, Wimpory R, Ohms C. A review of the NeT Task Group 1 residual stress measurement and analysis round robin on a single weld bead-on-plate specimen. *International Journal of Pressure Vessels and Piping*. 2014;**120-121**:93-140
- [11] Smith MC. NeT TG6 Finite Element Simulation Protocol, Issue 1 for Phase 1 Simulations, 2016
- [12] Farajian M. Stability and relaxation of welding residual stresses [PhD dissertation]. Braunschweig, Germany: Shaker Verlag; 2011
- [13] Armstrong PJ, Frederick CO. A mathematical representation of the multiaxial bauschinger effect. CEBG Report RD/B/N731. 1966
- [14] Goldak J, Chakravariti A, Bibby M. A new finite element model for welding heat sources. *Metallurgical Transactions*. 1984;**15B**:299-305

Residual Stress Analysis of Laser Remanufacturing

Shi-yun Dong, Chao-qun Song, Xiang-yi Feng,
Yong-jian Li and Shi-xing Yan

Additional information is available at the end of the chapter

<http://dx.doi.org/10.5772/intechopen.72749>

Abstract

Laser remanufacturing is an advanced repairing method to remanufacture damaged parts based on laser processing, such as laser cladding and laser welding. As a critical factor in determining the remanufacturing quality, residual stress of different laser-remanufactured parts was analysed by numerical methods based on deactivating and reactivating element theory, as well as experimental methods such as X-ray diffraction and hole drilling measurements. The distributions and evolution law of residual stress during multipass laser welding of 7A52 high-strength aluminium alloy, and the effects of forming strategy, heat input and solid-state phase transition on residual stress in the laser cladding forming layers of QT 500 cast iron and FV520B high strength steel, were emphatically studied. The simulation results of residual stress fit well with the experimental results, indicating that both residual stress and its accumulation phenomenon would occur during the laser welding and laser cladding forming, and were affected by factors such as welding pass, heat input and phase transition. It is feasible to control residual stress by using cross path forming strategy, less heat input and alloying power materials with low martensite transition point (Ms).

Keywords: residual stress, phase transition, laser remanufacturing, finite element analysis

1. Introduction

Remanufacturing was defined as a process of returning the used product to its original performance. And, it is required that performance specification of the remanufactured product should be equivalent to or even better than that of the new one. Remanufacturing engineering generally refers to the related techniques or engineering activities to remanufacture the waste products, which regards product life cycle theory as instructions and performance upgrading

as goals, with rules of energy-saving environment conservation-good quality-high efficiency by using advanced processing techniques [1]. It can bring great economic and social benefits on sources and environment to the world and has become an important way for sustainable society development [1–3].

Figure 1 shows the main procedures of used equipment remanufacturing process, which generally involves many steps such as disassembling, cleaning, detecting and assessing of the used components, remanufacturing, examining and reassembling of the remanufactured equipment. It also reveals that remanufacturing is supported by a series of relevant techniques during the whole process.

The remanufacturing forming procedure is of great importance to the quality of the remanufactured parts, which is also an obvious characteristic to distinguish remanufacturing production from manufacturing. As an advanced remanufacturing technology, laser remanufacturing can restore geometrical size and upgrade performance of the worn components with high productivity and little distortion, using laser cladding, laser welding, laser sintering or other laser-related processing methods [4, 5]. It has shown great benefits to the society for its successful applications over the last decade. More and more institutes, enterprises and industry sectors show great attentions to laser remanufacturing.

However, there are still some challenges for application of laser remanufacturing, especially residual stress-related problems such as brittle fracture, fatigue failure, stress corrosion cracking and buckling deformation [6]. As a research focus in recent years, residual stress has been experimentally measured by various damage detection methods such as hole drilling and indentation strain, as well as several non-destructive detection methods such as ultrasonic, X-ray diffraction and neutron diffraction methods. However, the experimental data are limited to thoroughly characterize the region distribution of residual stress. Hence, simulation method based on finite element model (FEM) is necessary to estimate the 3D residual stress field of the laser-remanufactured pieces. In this chapter, it introduces some researches on residual stress of laser remanufacturing metal pieces with cases of high-strength aluminium alloy, cast iron and high-strength steel, respectively.

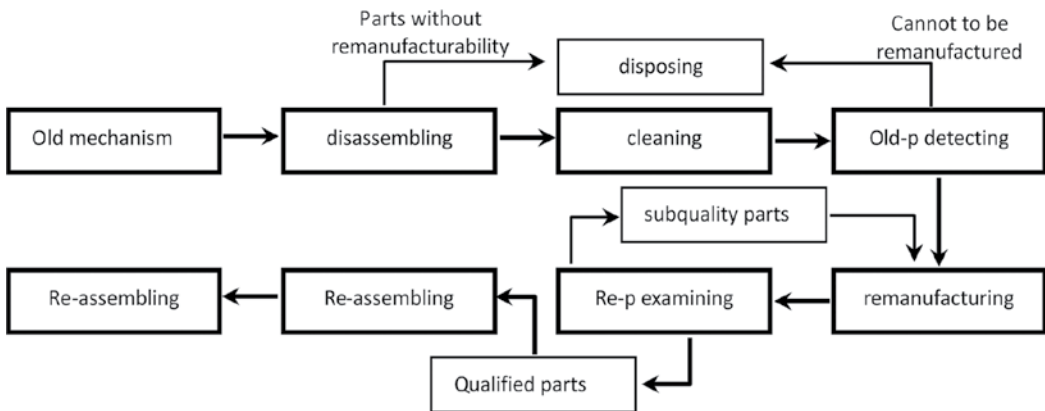


Figure 1. General procedures of mechanism remanufacturing.

2. Residual stress analysis of high-strength aluminium alloy pieces remanufactured by laser welding

Solidification cracking and stress corrosion cracking frequently occur in high-strength aluminium alloys, on the account of their relatively large linear expansion coefficients and high stress corrosion cracking susceptibility [7, 8]. Narrow gap laser welding (NGLW) is considered as one of the most effective ways to repair the cracks, for its lower heat input, less repairing deformation and better repairing quality, comparing with the conventional electric arc or plasma arc welding method [9–12]. However, residual stress of NGLW is also a vital factor for repairing quality of cracks and has been one of the research focuses of NGLW [13–15]. The aim of this work is to present distributions and evolution of residual stress during multipass NGLW processing.

2.1. Experimental procedure

The base material sample in this case was 7A52 aluminium alloy plates with dimensions of $50 \times 50 \times 20 \text{ mm}^3$, and the filler wire was ER 5356 feed wire. A parallel I-type groove was applied, with gap width 3 mm and groove depth 18 mm, as shown in **Figure 2a**.

The six-pass NGLW was conducted by a 4 kW IPG fibre laser system with welding parameters: laser power 3.20 kW, welding speed 0.48 m/min and wire feed speed 2.15 m/min. A K-type thermocouple was used to detect temperatures during the six-pass NGLW processing, which was located in the heat-affected zone (HAZ) about 5 mm from the groove sidewall and 9 mm from the plate top surface.

2.2. Numerical simulation procedure

MSC.Marc 2016.0.0 software was exploited to simulate the six-pass NGLW processing without regard to the molten pool flow and droplet transfer behaviour. One-half of the symmetric geometric model was adopted as shown in **Figure 2b**. The values of material thermo-physical

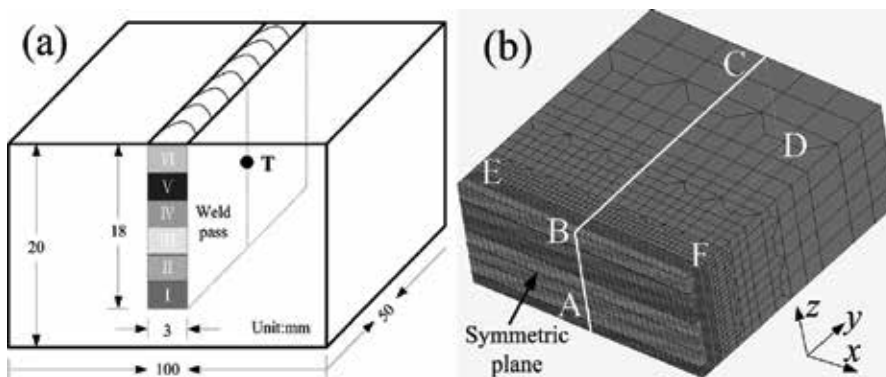


Figure 2. Sketch of the geometric model: (a) narrow gap groove and (b) mesh generation.

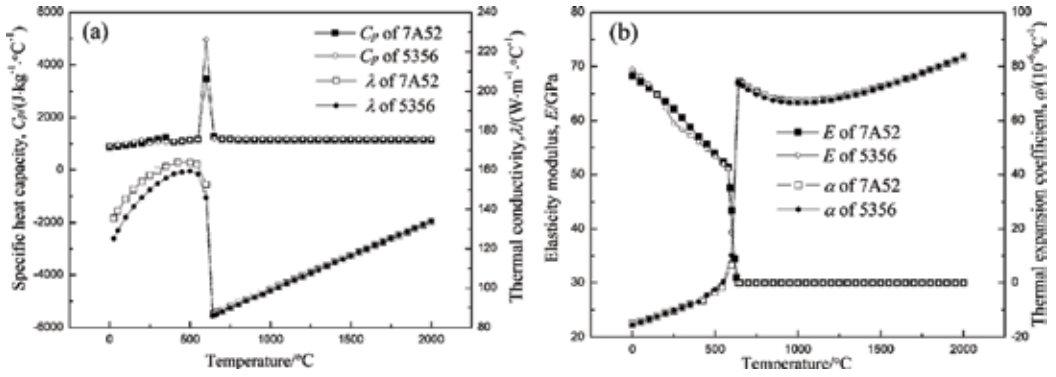


Figure 3. Thermo-physical values of 7A52 and 5356 aluminium alloys: (a) specific heat and thermal conductivity and (b) elasticity modulus and thermal expansion coefficient.

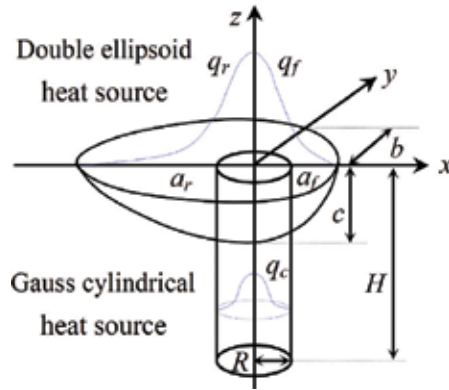


Figure 4. Sketch of the hybrid heat source model for NGLW.

property such as thermal conductivity thermal expansion coefficient and specific heat were estimated by the thermodynamic software JMatPro as given in **Figure 3**.

2.2.1. Heat source model

In order to more accurately describe the combined thermal effects of molten drop and laser irradiation on the base metal, a hybrid heat source model was adopted by combining double-ellipsoid heat source and Gauss cylindrical heat source, as shown in **Figure 4**.

The heat flux distribution in front half part (q_f) and latter half part (q_r) of the double ellipsoid could be, respectively, described as follows:

$$q_f(x, y, z) = \frac{6\sqrt{3}Q_1 f_f}{a_f b c \pi \sqrt{\pi}} \exp \left\{ -3 \left[\frac{(x - v_w t)^2}{a_f^2} + \frac{y^2}{b^2} + \frac{z^2}{c^2} \right] \right\} \quad (1)$$

$$q_r(x, y, z) = \frac{6\sqrt{3}Q_1 f_r}{a_r b c \pi \sqrt{\pi}} \exp \left\{ -3 \left[\frac{(x - v_w t)^2}{a_r^2} + \frac{y^2}{b^2} + \frac{z^2}{c^2} \right] \right\} \quad (2)$$

Parameter	a_f	a_r	f_f	f_r	b	c	R	H	β
Values	1.5 mm	4.0 mm	0.55	1.45	1.5 mm	2.5 mm	0.4 mm	4.0 mm	0.15

Table 1. The values of heat source parameters.

where a_f , a_r , b and c are the geometric parameters, v_w and t are the welding velocity and time and f_f and f_r are the distribution coefficient of heat flux determined by a_f and a_r .

The heat flux values (q_c) in Gauss cylindrical are characterized by Gaussian distribution in the radial direction and exponential decay along the depth, expressed as follows:

$$q_c(r, h) = \frac{6Q_2}{2\pi HR^2 + \beta\pi RH^2} \exp\left[\frac{-3r^2}{R^2}\right] \left[\frac{\beta h + R}{R}\right] \quad (3)$$

where R and H are the effective radius and height of Gauss cylindrical, respectively, and β is the energy attenuation coefficient.

Here, the adopted values of heat source parameters are given in **Table 1** on the basis of previous optimization by experimental observations to molten pool, measurements of joint on its cross section and comparisons between the simulated and experimental results.

2.2.2. Governing equations

The heat transfer phenomena in NGLW process is governed by the three-dimensional heat conduction equation for unsteady state:

$$\rho C_p \frac{\partial T}{\partial t} = \frac{\partial}{\partial x} \left(\lambda \frac{\partial T}{\partial x} \right) + \frac{\partial}{\partial y} \left(\lambda \frac{\partial T}{\partial y} \right) + \frac{\partial}{\partial z} \left(\lambda \frac{\partial T}{\partial z} \right) + Q_i + \Delta H \quad (4)$$

where ρ , λ and C_p are the density, thermal conductivity and specific heat, T is the temperature, Q_i is the internal heat source intensity and ΔH is the latent heat of fusion and crystallization. In this case, equivalent specific heat method was used to deal with ΔH , assuming that values of C_p had abrupt changes between the solidus and liquidus temperatures.

2.2.3. Boundary conditions

The symmetrical plane was assumed as adiabatic condition, while on other planes, heat transfer from metal substrate to atmosphere or backing plate occurred by means of thermal convection and radiation, and the thermal boundary condition can be defined as

$$-\lambda \frac{\partial T}{\partial n} = h_c(T - T_0) + \sigma\varepsilon(T^4 - T_0^4) \quad (5)$$

where λ is the thermal conductivity, T_0 is the atmosphere temperature, h_c is the convective heat transfer coefficient, σ is the Stephan-Boltzmann constant and ε is the emissivity.

As for the mechanical boundary conditions, the y -direction displacement of all nodes was fixed on the symmetrical plane to keep the balance of joint, while the nodes on the bottom plane and side edge were fixed in z direction to prevent rotational movement.

2.3. Result and discussions

2.3.1. Validation of the model

Figure 5 shows the comparison of calculated and measured temperature curves from the third pass during NGLW processing, which presents good agreement between them. The peak temperature of the calculated curve was 308.2°C, which was close to the measured 301.5°C. And the heating or cooling rates of the measured curve are slightly lower due to thermal inertia of thermocouple.

2.3.2. Evolution of transient stress field

Figure 6 shows the evolution of calculated transverse stress σ_y distribution in the middle of the first, third and fifth pass during NGLW processing. There is almost no stress existing in molten pool for melting of metal substrate. However, stress of its vicinity appears as compressive stress as a result of thermal expansion effect, which in turn leads to a tensile transverse stress at its distant zone. By comparing absolute value of the transverse stress and its concentration region in different weld passes, the existence of stress accumulation phenomenon can be confirmed during the multipass NGLW process.

2.3.3. Residual stress analysis

Figure 7 shows the 3D distributions of the numerically predicted transverse residual stress, longitudinal residual stress, vertical residual stress and von Mises equivalent residual stress in the joint. The concentration region of high residual stress is predominately presented in the weld zone or HAZ near the fusion line, where the latter part has higher values of von Mises equivalent stress than the front part for the gradual accumulations of distortion and stress, as shown in **Figure 7d**.

The residual stress distributions along the weld centre line EF and its vertical line BC, as marked in **Figure 1b**, are shown in **Figure 8**. Along the centre line of weld, both the transverse and longitudinal residual stresses show stable tensile stress characteristics with average values of 45.5 and 141.4 MPa, without regard to its unstable front and latter part. During the welding, rapid fusion and solidification appear along welding direction, accompanied by unbalanced

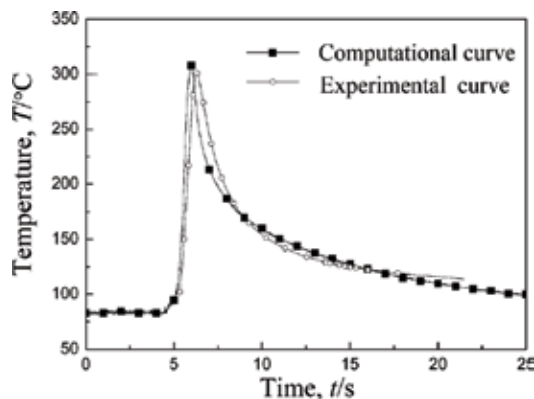


Figure 5. Calculated and measured temperature curves from the third pass.

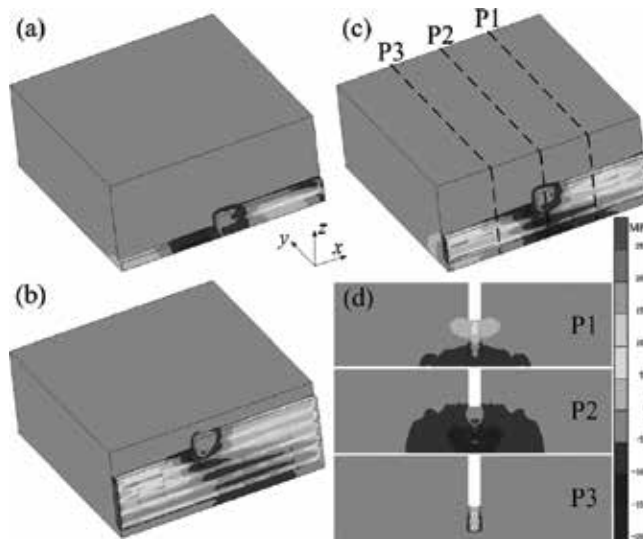


Figure 6. Distribution of transverse stress during the (a) first pass, (b) fifth pass, (c) and (d) third pass NGLW.

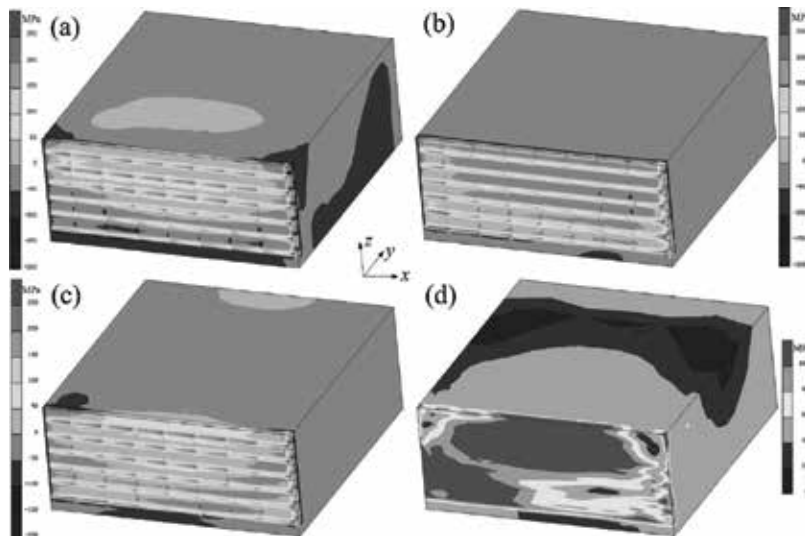


Figure 7. 3D residual stress distributions: (a) transverse residual stress σ_y , (b) longitudinal residual stress σ_x , (c) vertical residual stress σ_z and (d) von Mises equivalent stress.

expansion and shrinkage behaviours, resulting in higher longitudinal residual stress than the transverse residual stress. Nevertheless, the distribution of residual stress in its vertical direction is more complicated, as presented in **Figure 8b**. With increase of distance from the weld centre, values of transverse and longitudinal residual stress rapidly decline at the fusion line, and then the longitudinal residual stress decreases gradually until it turns into compressive residual stress from tensile stress, while the transverse residual stress begins to increase and then descends again, maintaining tensile residual stress all through.

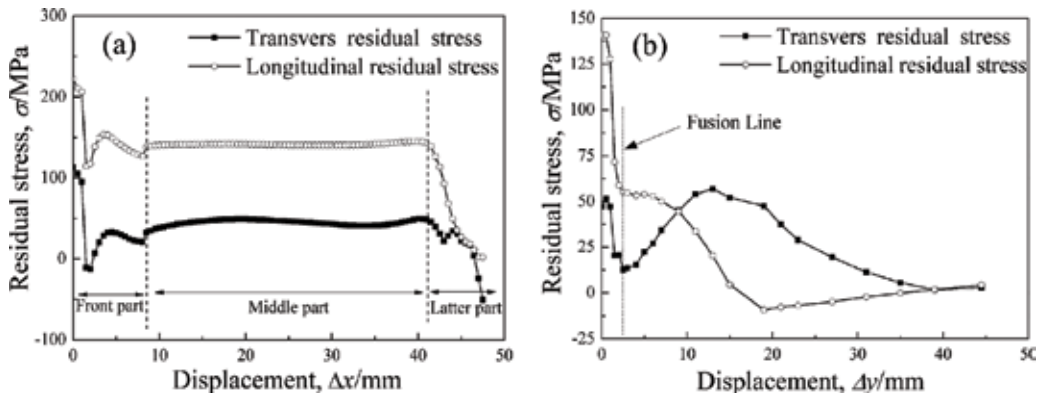


Figure 8. Residual stress distributions along (a) line EF and (b) line BC marked in Figure 1b.

3. Residual stress analysis of cast iron pieces remanufactured by laser cladding

QT 500 nodular cast iron as an industrial basic material is widely used in ship engines, crankshafts and machine tools [16–18]. As for laser cladding remanufacturing the cast iron pieces, due to the high carbon content, brittle phases are easily generated near the interface between the clad and substrate which causes residual stress during remanufacturing process. Therefore, study on residual stress and its control measures is vital to successful remanufacturing of cast iron components [19–21]. Two common laser pass-forming methods, parallel stacking forming and cross stacking forming, are chosen for the laser cladding process, as shown in Figure 9. A kind of Ni-Cu alloy power with element content of 0.03 wt.%C, 2.0 wt.%Si, 1.1wt.% B, 0.5wt.%Fe and 20.0 wt.%Cu and the balance Ni was selected as the cladding material, whose particle size scale was 20–106 μm .

3.1. Numerical simulation procedures

Thermal stress after cast iron laser cladding mainly comes from shrinkage of the clad layers during cooling process. Larger expansion coefficient difference between the substrate and the clad always caused larger residual stress after processing, which is usually a direct reason to the layer cracking. The cast iron parts are often large-scale castings, which can be considered as a fully constrained state around the forming layer.

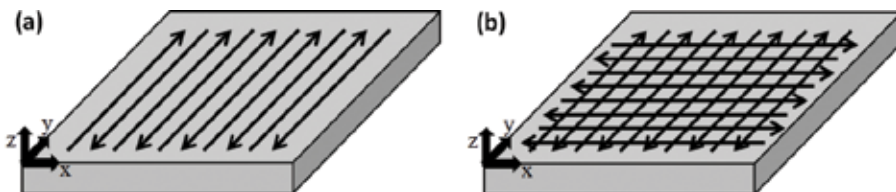


Figure 9. Sketch of the laser passes: (a) parallel stacking and (b) cross stacking.

Double-ellipsoid heat source model and Gauss body heat source model are often used to simulate the welding process, but the process of laser cladding is different with welding process; these heat source models are not suitable for simulating the cladding. Coupling of uniform body heat source (the energy density is same in different points of the heat source) and Gauss surface heat source was adopted in this experiment simulation process. The simulation uses ANSYS finite element software. Firstly, the stress evolution process under parallel stacking forming and cross stacking forming passes was simulated. Considering the actual remanufacturing process, the model is under one side constraint or fully constrained state. **Figure 10** is the temperature distribution at 2 and 5 s after multilayer laser cladding process, and **Figure 11** shows the temperature cycle curve of the fusion zone and the heat-affected zone. It can be seen that the clad layer and the heat-affected zone undergo repeated thermal cycles, which easily results in stress concentration.

Figure 12 shows the nephogram of the longitudinal stress, the deformation and macroscopic stress state in remanufacturing process. Ends of the sample in x direction are restrained. It can be seen that the stress is mainly concentrated around the constraint parts and the layers. **Figure 13** is the curve of the longitudinal stress of a node in the layer and a node in the substrate, and the node's location can be seen in **Figure 12**. The layer mainly presents the tensile stress state, while the substrate is mainly in the state of compressive stress. For the actual remanufacturing process, the constraints should be avoided or removed as far as possible.

3.2. Experimental procedure

In order to obtain the residual stress distribution in the surface and interior of the clad layer, X-ray diffraction method was used for measuring the accumulation of residual stress in the clad layer. The electrolytic etching method was used to peel clad layer from the top surface to the internal layer, and the thickness of the peeling layer is 60 μm . Residual stress parallel or vertical to the cladding line was tested, respectively, at a certain point, and the schematic diagram of the test is shown in **Figure 14**.

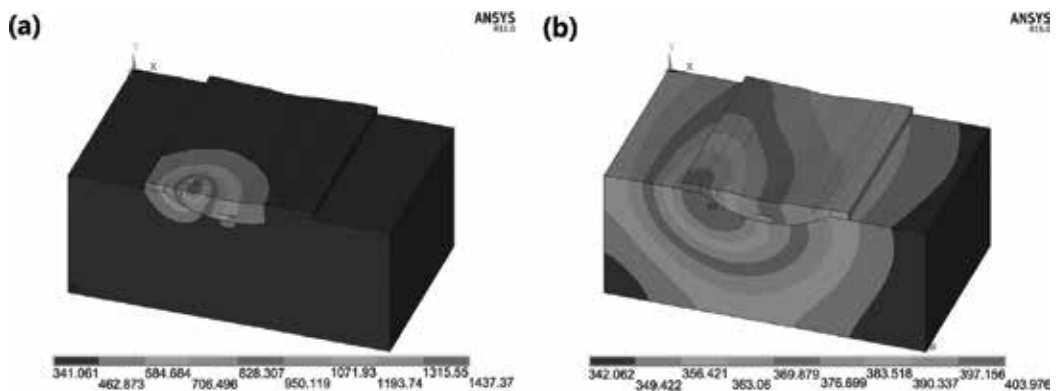


Figure 10. Temperature distribution at (a) 2 and (b) 5 s.

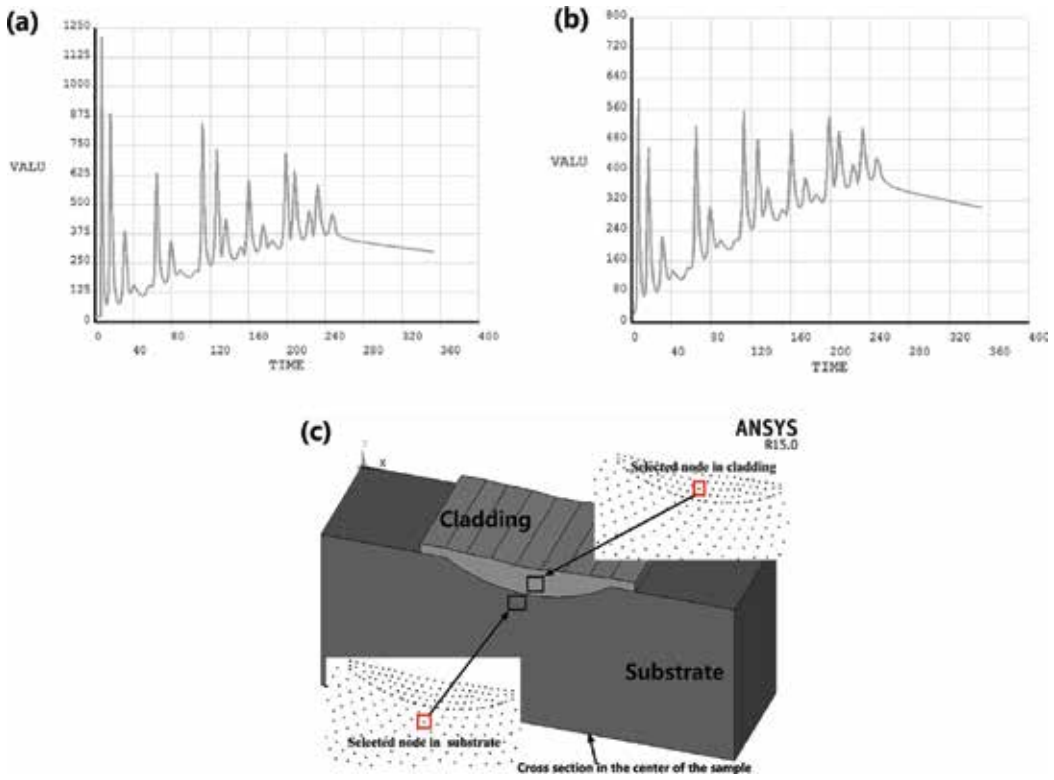


Figure 11. Temperature distribution of different zones: (a) the fusion zone and (b) the HAZ (c) location of the selected nodes.

3.3. Results and discussions

Figure 15 shows residual stress distribution in different scanning passes in the clad layer. It can be found that residual stress increases slowly from the surface to inside of the layers formed by cross stacking method. The state of stress is tensile stress with the highest value +300 MPa. The residual stress of the clad layer formed by the parallel path is fluctuated from the surface to the interior, and the fitting curve shows a downward trend. The residual stress at the top of the clad layer reaches the highest tensile stress, reaching +380 MPa, and the lowest residual stress is 50 MPa inside the clad layer. It can be seen that the residual stress of the cross path cladding is smaller than that of the parallel path in the range of 340 μm depth from the surface, and beyond this range, residual stress changes in opposite direction. Residual stress distribution vertical to cladding line direction of the cladding is shown in Figure 15b. It can be found that residual stress from the surface to the interior in the clad layer in two kinds of forming methods is increased, but the residual stress in the layers formed in cross path is smaller than that of parallel path at different depths. It can be seen that the cross path forming is beneficial to reduce the thermal stress of the clad layer in the vertical direction.

The thermal cycle curve of the cross stacking forming shows irregular and overlapping effect, and the interval between two adjacent temperature peaks is relatively large. Therefore, there is

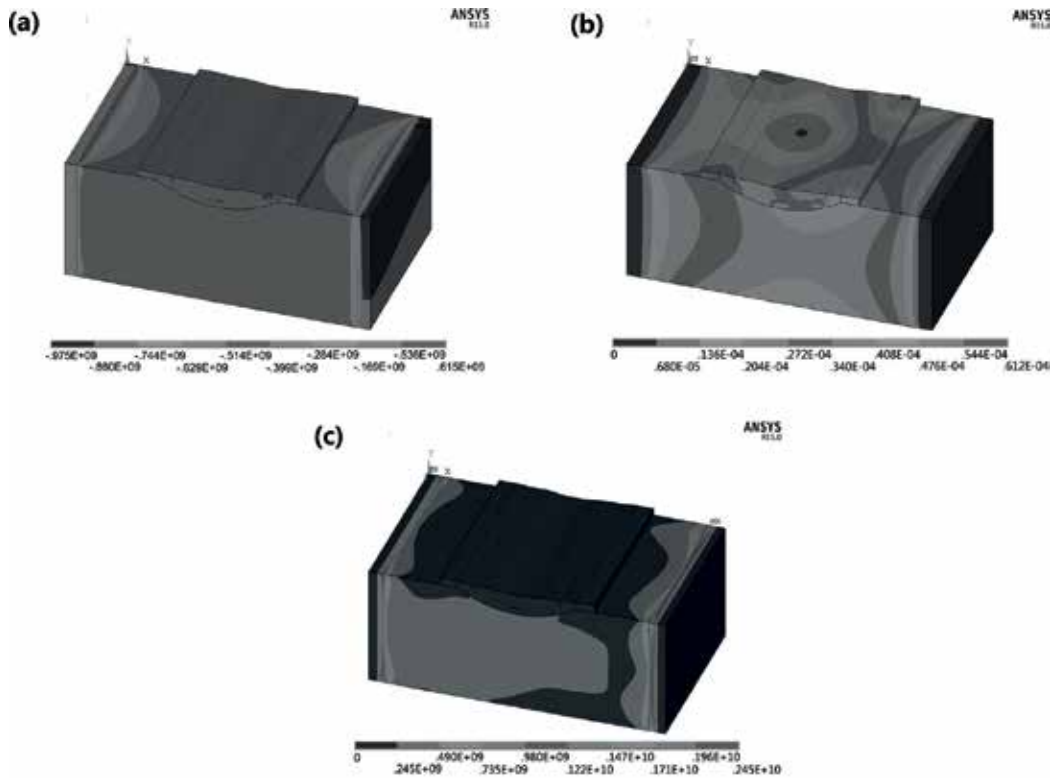


Figure 12. Nephogram of stress and deformation: (a) longitudinal stress, (b) deformation and (c) macroscopic stress.

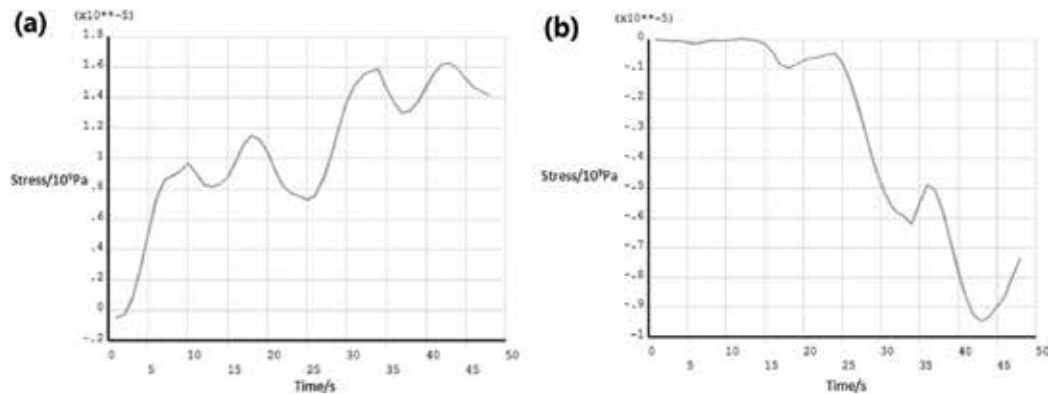


Figure 13. Stress curves of the (a) selected node in the layer and (b) selected node in the substrate.

no apparent periodic heat accumulation in the clad layer, and the heat dispersion effect is obvious. Therefore, characteristics of the temperature field with relatively small temperature gradient caused smaller shrinkage difference of the clad layer, and the thermal stress in the clad layer decreased. The thermal cycling curves of parallel path forming show apparent

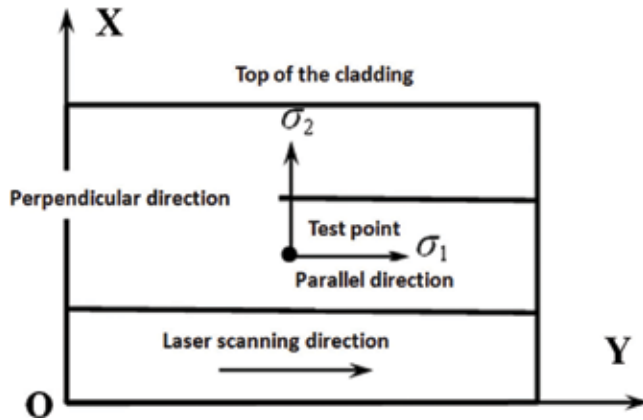


Figure 14. Schematic diagram of residual stress tests.

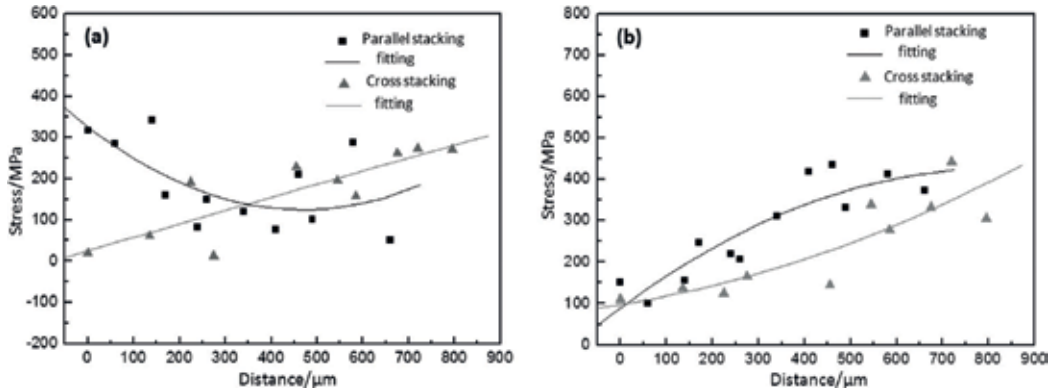


Figure 15. Residual stress in different scanning passes: (a) parallel and (b) vertical to cladding line.

periodic thermal cumulative effect and heat accumulation of the clad layers, then large temperature gradient exists between high-temperature area of molten pool and the ambient clad layer and the shrinkage deformation and the stress of layers increases. Therefore, the cross path forming is beneficial to the thermal stress control of the clad layer.

Figure 16 shows residual stress distribution in the clad layer with different laser powers. It shows that the residual stress differs obviously in the parallel direction and vertical direction when the power increased from 800 to 1200 W. The residual stress decreases apparently in the layers parallel to cladding direction when depth increases. The residual stress in the surface reaches 120 MPa. In depth of 60 μm layer, the tensile stress begins to change into the compressive stress, and in depth of 600 μm , the residual stress reached -300 MPa in the clad layer. In contrast, stress decreases slowly when the power is 800 W.

In the vertical direction of the cladding line, with the increase of layer depth, residual tensile stress of clad layer increases from the surface to the interior when the power reaches 1200 W. The curve slope becomes larger, which means that the stress increases persistently with the

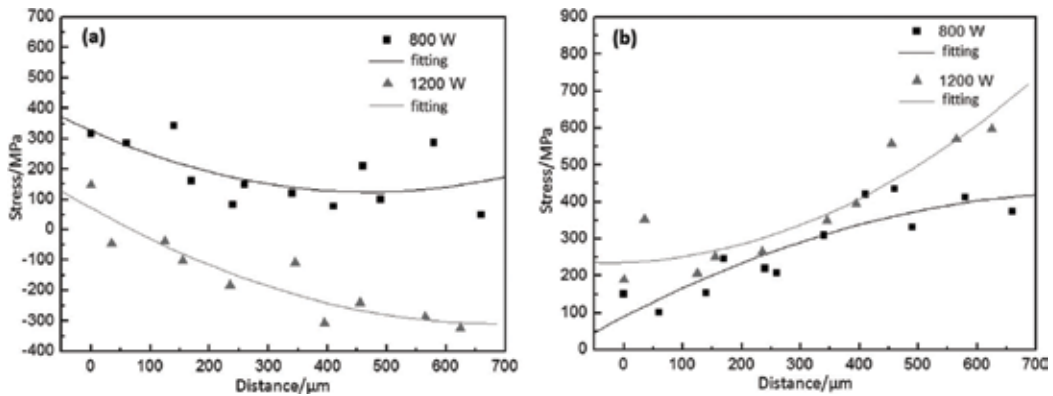


Figure 16. Residual stress curves in different laser powers: (a) parallel and (b) vertical to cladding line.

increase of the depth. At the depth of 600 μm, the residual tensile stress of the clad layer reaches 600 MPa, approaching the tensile strength of the clad layer, and the cracking tendency of the deposited clad layer increases. Therefore, the stress distribution characteristics of the clad layer under 1200 W are poor, and the cracks may exist in the clad layer. This also verifies that the low-power cladding process has good quality control effect on the remanufacturing of cast iron castings.

According to the analysis of temperature field at the laser power of 800 and 1200 W, with the increase of laser power, the peak temperature of the thermal cycle curve increases significantly, and the temperature gradient of molten pool and gradient around the area increases. Reduction of cooling time causes cooling velocity to increase rapidly and results in the increasing of elastic-plastic deformation of cladding under residual stress. After solidification, the residual stress distribution along different directions is shown in **Figure 16**.

To sum up, temperature field of laser cladding during cladding process has an important influence on the residual stress of the laser cladding. The results of the simulation and the actual test show that for the remanufacturing process of cast iron, it can be helpful to reduce the overall residual stress by using cross path method, and lower heat input causes lower residual stress. These two methods result in the homogenization of the expansion and contraction of the layers during cladding process; therefore, the deformation is smaller, and the residual stress is relatively low. Therefore, from the point of view of controlling the residual stress of the clad layer, using low power and cross path method are used to control the residual stress of the clad layer.

4. Residual stress analysis of high-strength steel pieces remanufactured by laser cladding

During the complex thermal cycling of laser cladding, the high-strength steel, solid phase transition, such as eutectoid reaction, solid solution reaction, austenite transition and martensitic transition usually take place. Solid-state phase transition, which is accompanied by specific

volume change, transition plasticity and some other effects, will affect the stress field and final residual stress distribution.

The occurrence of solid-state phase transition may have a certain impact on laser cladding or other welding processes under certain conditions. In some cases, the effect is even dominant. Since transition-induced plasticity increases the martensitic transition temperature, the martensitic transition has a significant effect on distribution of residual stress [22]. Ohta [23] studied the effect of solid phase transition on the evolution of residual stress and analysed the influence of diffusion phase transition and non-diffusion phase transition on residual stress. Materials with low phase transition point will result in lower residual stresses; the effect of solid-state phase transition on mechanical properties, solid phase transition volume effect and solid-state phase transition plasticity is the main factors affecting the stress evolution [24].

For steel, it is a hotspot to consider the solid-state phase transition effect in the process of laser cladding thermal-machine simulation. However, the actual situation is complex and still has some work to be done [25]. Firstly, the coupling interaction is very complicated since the stress has a great effect on the phase transition temperature and phase transition kinetics, which in turn affects the evolution of stress. Secondly, the tempering effect accompanying the thermal cycling will affect the physical properties and phase transition properties of the material. Then, many work lacks systematic and reliable physical data, especially computer simulation, in which the systematic and reliability of the data is a very important factor. Moreover, the research results are mostly limited to the welding process [25, 26].

4.1. Numerical simulation procedure

The laser cladding is a processing with multi-parameter, complex nonlinearity and strong coupling and has a wide variety of scanning strategies; the scanning strategy is in direct relation to the thermal cycle of the laser cladding process, which has great influence on the stress, strain and microstructure of the remanufacturing part. Based on a few simplification and assumptions, computer simulation can try all kinds of process parameters and provides the temperature and stress data of remanufacturing part at any point and any time for the analysis of stress, microstructure and properties evolution.

Austenite is set as the initial phase in the solidification process. As temperature decreases, the martensitic phase transition starts at M_s (the martensite starting temperature) and finishes at M_f (the martensite finishing temperature). The volume fraction of martensite phase (f_M) can be shown as [27]

$$f_M = 1 - f_{\gamma 0} \Phi(T) \quad (6)$$

$$\Phi(T) = \begin{cases} 1 & T \geq M_s \\ \exp(-\alpha(M_s - T)) & T < M_s \end{cases} \quad (7)$$

where $f_{\gamma 0}$ is the initial austenitic volume percentage and $f_{\gamma 0} \Phi(T)$ is the ratio of austenite at a specific temperatures α is the kinetics coefficient of phase change, and can be obtained by experiments.

Phase transition plasticity refers to the plastic strain of the material under the external load which is much less than yield strength. It mainly comes from the Greenwood-Johnson mechanism and the Magee mechanism. According to the classic work of Inoue, Leblond and Fisher, considering that during the laser cladding processing the longitudinal residual stress value is close to that of yield strength, the expression of the stress increment should be revised to

$$\Delta\varepsilon^{Trp} = -\frac{2\Delta\varepsilon_{\alpha\gamma}}{\sigma_y^y(\varepsilon_y^{eff})} \ln(f_M) \Delta f_M \cdot h\left(\frac{\sigma^{eq}}{\sigma^y}\right) \cdot S_{ij} \quad (8)$$

where $\Delta\varepsilon_{\alpha\gamma}$ is the strain difference between austenite and martensite considering the volume effects of phase transition, $\sigma_y^y(\varepsilon_y^{eff})$ is the yield strength of high-temperature phase (taking into account the hardening effect), S_{ij} is the deviatoric stress tensor and f_M is the volume fraction of martensite.

The expression above is complex, and in practice the related parameters are difficult to obtain. A simplified equation is put forward [25]:

$$\Delta\varepsilon^{Trp} = 3k(1 - f_M) \Delta f_M \cdot S_{ij} \quad (9)$$

where k is easily obtained by experiments.

It is assumed that the initial and final austenitic ratio is $f'\gamma_0$ and 100% when the temperature rises to Ac_1 and Ac_3 , respectively; the percentage of austenite phase increases linearly as temperature rises. Once the temperature is lower than Ms , austenite will partially or totally transform into martensite during the subsequent cooling period. The martensite tempering and formation of interdendritic eutectic phase during solidification are neglected.

In this work, under the condition of single-pass deposition, three kinds of situations are analysed in comparison: the two are phase transition (one considering stress influence) and the other one without phase transition. We obtained the following characteristics by experiments: expansion coefficient of martensite state is about $18.75 \times 10^{-6}/^\circ\text{C}$ (room temperature) and rises up to $\sim 19 \times 10^{-6}/^\circ\text{C}$ (at above 600°C); $Ms = 160^\circ\text{C}$, $Ac_1 = 600^\circ\text{C}$ and $Ac_3 = 900^\circ\text{C}$; the volumetric change strain is 0.0067352; kinetic coefficient of the phase transition during the cooling period is ~ 0.02347 ; and parameter of transition plasticity is 1.165×10^{-4} . Molten pool convection is simulated indirectly by elevated thermal conductivity coefficient (twice as large as that of room temperature) and the double-ellipsoid heat source. Latent heat (283 J/g) is taken into consideration when melting and solidification take place. The emissivity (ε) is defined to be 0.5, and the convection coefficient (h_c) is $30 \text{ W/m}^2 \text{ K}$. Initial temperature is set at 25°C (room temperature). Finally, the deposition process is regarded as quasi-steady process, and the materials are assumed isotropic [25].

4.2. Experimental measuring procedure

In the same piece of substrate, under the same experimental conditions, technological parameters and using different material powders (with phase transition and without phase transition,

	C	Cr	Ni	Mo	Mn	Nb	Si	B	Cu	Fe
1	0.13	12.8	4.7	—	—	—	1.0	1.4	—	Bal
2	0.03	—	Bal	—	—	—	2	1.1	20	0.5
3	0.03	17.5	14	2.3	2.0	—	1.0	—	—	Bal
4	0.1	15	10	—	—	—	1.0	1.0	—	Bal
5	0.03	13.8	4.5	1.0	0.7	0.35	0.5	—	—	Bal
6	0.12	15.4	4.2	1.4	0.6	—	1.4	0.8	—	Bal
7	0.05	—	Bal	—	—	—	2.7	1.8	—	0.4

Table 2. The ingredients of the used laser cladding alloying powders.

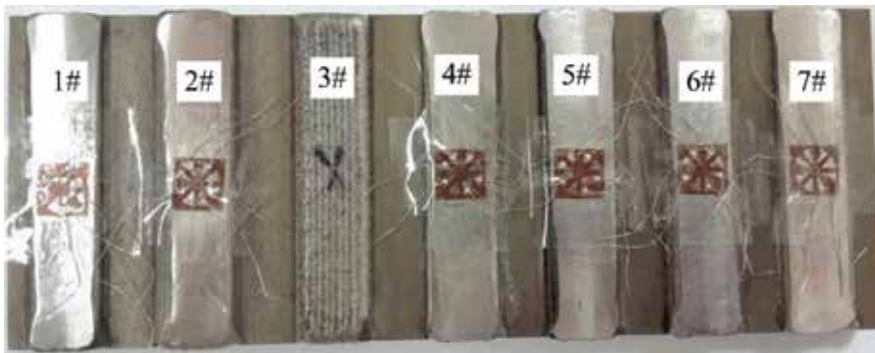


Figure 17. The laser cladding samples of different alloying powders.

	M_s (°C)	Y_s (MPa)	σ_1 (MPa)	σ_2 (MPa)	σ_e (MPa)
1	250	1280	163.44	-32.06	181.60
2	None	—	88.86	-8.11	73.26
3	Below RT	—	—	—	—
4	Below RT	720	430.07	111.04	386.69
5	158	920	-196.91	-307.47	269.75
6	190	1150	-67.52	-169.83	148.11
7	None	530	349.26	187.61	302.75

Table 3. The result of the residual stress (RT, room temperature).

respectively) as shown in **Table 2**, the hole drilling method is used for measurement of residual stress of different powders in one position.

In this case, FV520B is martensitic precipitation-hardening steel with excellent strength and good welding performance and is used as the substrate. These samples (**Figure 17**) are clad layers of different materials, and the scanning strategy is arch deposition (as shown in **Table 2**).

The technology parameters of the laser cladding process are as follows: energy power is 1.8 kW; scanning rate is 8 mm/s; width of a single track is 3 mm; and lapping rate is 0.5.

The residual stress results are shown in **Table 3**; it can be seen that:

1. For samples with solid-state phase transition, the first principal stress values are both low; #5 and #6 samples show compressive stress, and #1 sample is in tension stress state, whose value is at about 12.7% of the yield stress in the room temperature.
2. For most samples with no solid-state phase transition, the first principal stress of tension stress state and the stress value are high.
3. For materials with solid-state phase transition, the higher solid-state phase transition temperature means higher residual stress obtained.

4.3. Result and discussions

Figure 18 shows the residual stress distribution under the condition of single-pass deposition. Firstly, the stress distribution is nearly the same in the area away from the cladding bead. For the case with phase transition considered (**Figure 18b**), it is obvious that the stresses are lower in the clad bead as well as the adjacent region. Moreover, the interface between the cladding and substrate shows a lower stress level than that of the clad layer and substrate. The maximum tensile stress is observed at about a few millimetres from the surface of the clad layer. Nonetheless, when the phase transition is ignored (**Figure 18a**), the residual stresses in the cladding bead increase obviously, which are near the yield strength; the maximum tensile stress is found in the interface between the substrate and the clad layer. When phase transition is taken into account, the cases with and without considering the stress effect on phase transition temperature (**Figure 18c** and **d**, respectively) show a similar residual stress level and distribution [25].

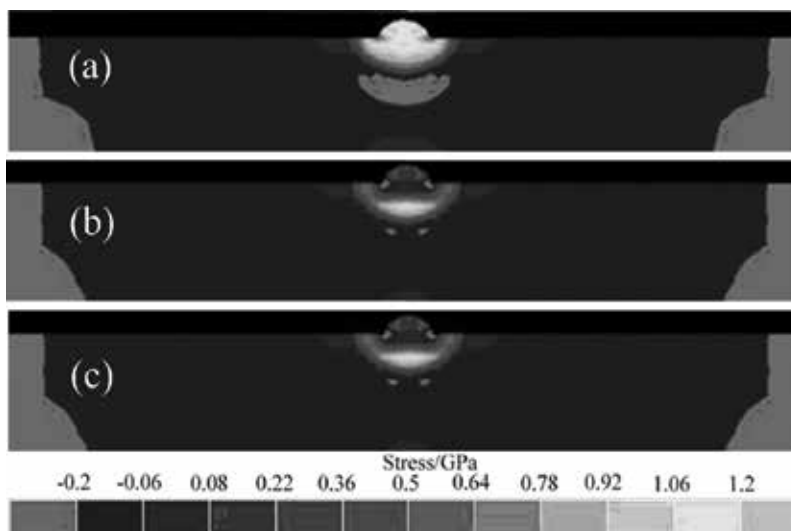


Figure 18. Stress distribution of single-layer laser clad sample: (a) ignore phase transition (b) considering phase transition, and ignore the stress effect on phase transition temperature (c) considering both phase transition and stress effect on phase transition temperature.

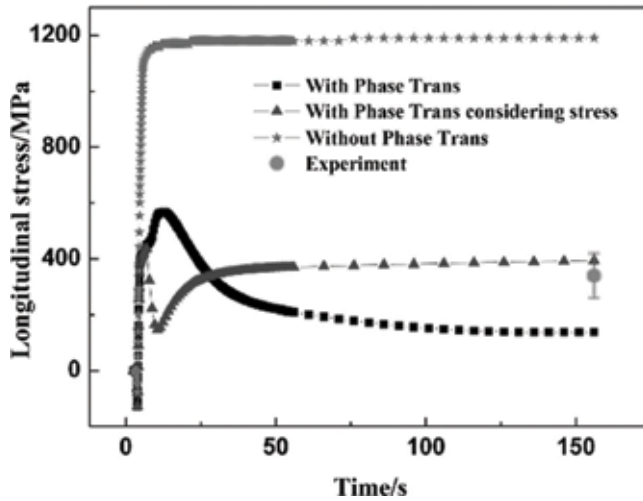


Figure 19. Longitudinal stress of a single-pass laser clad from calculation and experiment determination.

Figure 19 shows longitudinal residual stress evolution (z direction, along the laser travel) of the midpoint in a clad layer. The simulation results are in contrast to the results obtained by experimental determination. When the phase transition is ignored, the residual longitudinal stress is close to the yield strength (around 1200 MPa). When considering the phase transition, as the temperature decreases, the maximum longitudinal stress is around 600 MPa and finally stabilized at around 200 MPa. When the stress influence on phase transition temperature is considered, the residual longitudinal stress is closer to the experimental results (394 MPa) than the other two cases. Generally speaking, phase transition has an obvious effect on the residual stresses, making it a more accurate simulation result.

5. Conclusions

Laser remanufacturing is an advanced repairing method to restore the damaged parts based on laser processing, such as laser cladding and laser welding. To avoid obvious distortion and severe residual stress concentration, it is necessary to carry out residual stress analysis by numerical simulation and experimental methods. For high-strength aluminium alloy parts remanufactured by multipass NGLW process, welding passes have obvious effects on the distribution of residual stress, and its accumulation phenomenon would be exacerbated with the increase of welding passes. From the point of view of controlling the residual stress, low laser power and cross path forming strategies were suggested for their important influences on the residual stress in the laser clad layer of nodular cast iron pieces. For high-strength steel with solid-state phase transition remanufactured by laser cladding, the phase transition from austenite to martensite during the cooling process had a positive influence to reduce the magnitude of residual stresses, and a lower residual stress can be obtained using alloying powder materials with lower solid-state phase transition temperature.

Acknowledgements

The work was supported by the key programme of the National Key Research and Development of China (Grant No. 2016YFB1100205), NSFC programme (Grant No.51705532) and Beijing Science and Technology projects (Grant No. Z161100004916009, Z161100001516007).

Author details

Shi-yun Dong*, Chao-qun Song, Xiang-yi Feng, Yong-jian Li and Shi-xing Yan

*Address all correspondence to: syd422@sohu.com

National Key Laboratory for Remanufacturing, Beijing, China

References

- [1] Xu BS. Theory and technology of equipment remanufacturing engineering. National Defense Industrial Press, Beijing, China; 2007
- [2] Xu Bs, Dong sy, Zhu S, et al. Prospects and developing of remanufacture forming technology [J]. Journal of Mechanical Engineering. 2012;**48**(15):96-105. DOI: 10.3901/JME.2012.15.096
- [3] Cunha JO, Konstantaras I, Melo RA, et al. On multi-item economic lot-sizing with remanufacturing and uncapacitated production. Applied Mathematical Modelling. 2017;**50**: 772-780. DOI: 10.1016/j.apm.2016.10.037
- [4] Xu BS, Dong SY. Laser Remanufacturing Technology. Beijing, China: National Defense Industry Press; 2016
- [5] Dong SY, Xu BS, Wang ZJ, et al. Laser remanufacturing technology and its applications. Lasers in Material Processing and Manufacturing III. 2007;**6825**:68251N. DOI: 10.1117/12.782335
- [6] De A, DebRoy T. A perspective on residual stresses in welding. Science and Technology of Welding and Joining. 2011;**16**(3):204-208. DOI: 10.1179/136217111X12978476537783
- [7] Hu B, Richardson IM. Mechanism and possible solution for transverse solidification cracking in laser welding of high strength aluminium alloys. Materials Science and Engineering: A. 2006;**429**(1):287-294. DOI: 10.1016/j.msea.2006.05.040
- [8] Sheikhi M, Ghaini FM, Assadi H. Prediction of solidification cracking in pulsed laser welding of 2024 aluminum alloy. Acta Materialia. 2015;**82**:491-502. DOI: 10.1016/j.actamat.2014.09.002

- [9] Guo W, Li L, Dong SY, et al. Comparison of microstructure and mechanical properties of ultra-narrow gap laser and gas-metal-arc welded S960 high strength steel. *Optics and Lasers in Engineering*. 2017;**91**:1-15. DOI: 10.1016/j.optlaseng.2016.11.011
- [10] Dittrich D, Schedewy R, Brenner B, et al. Laser-multi-pass-narrow-gap-welding of hot crack sensitive thick aluminum plates. *Physics Procedia*. 2013;**41**:225-233. DOI: 10.1016/j.phpro.2013.03.073
- [11] Zhang ZH, Dong SY, Wang YJ, et al. Microstructure characteristics of thick aluminum alloy plate joints welded by fiber laser. *Materials & Design*. 2015;**84**:173-177. DOI: 10.1016/j.matdes.2015.06.087
- [12] Zhang ZH, Dong SY, Wang YJ, et al. Study on microstructures and mechanical properties of super narrow gap joints of thick and high strength aluminum alloy plates welded by fiber laser. *The International Journal of Advanced Manufacturing Technology*. 2016;**82**(1-4): 99-109. DOI: 10.1007/s00170-015-7334-5
- [13] Guo W, Francis JA, Li L, et al. Residual stress distributions in laser and gas-metal-arc welded high-strength steel plates. *Materials Science and Technology*. 2016;**32**(14):1449-1461. DOI: 10.1080/02670836.2016.1175687
- [14] Elmesalamy A, Francis JA, Li L. A comparison of residual stresses in multi pass narrow gap laser welds and gas-tungsten arc welds in AISI 316L stainless steel. *International Journal of Pressure Vessels and Piping*. 2014;**113**:49-59. DOI: 10.1016/j.ijpvp.2013.11.002
- [15] Phaoniam R, Shinozaki K, Yamamoto M, et al. Solidification cracking susceptibility of modified 9Cr1Mo steel weld metal during hot-wire laser welding with a narrow gap groove. *Welding in the World*. 2014;**58**(4):469-476. DOI: 10.1007/s40194-014-0130-2
- [16] Jeshvaghani RA, Harati E, Shamanian M. Effects of surface alloying on microstructure and wear behavior of ductile iron surface-modified with a nickel-based alloy using shielded metal arc welding. *Materials and Design*. 2011;**32**(3):1531-1536. DOI: 10.1016/j.matdes.2010.10.006
- [17] Pouranvari M. On the weldability of grey cast iron using nickel based filler metal. *Materials & Design*. 2010;**31**(7):3253-3258. DOI: 10.1016/j.matdes.2010.02.034
- [18] Cheng X, Hu SB, Song WL, et al. Improvement in corrosion resistance of a nodular cast iron surface modified by plasma beam treatment. *Applied Surface Science*. 2013;**286**(4): 334-343. DOI: 10.1016/j.apsusc.2013.09.083
- [19] Abboud JH. Microstructure and erosion characteristic of nodular cast iron surface modified by tungsten inert gas. *Materials & Design*. 2012;**35**:677-684. DOI: 10.1016/j.matdes.2011.09.029
- [20] Zhong ML, Liu WJ, Zhang HJ. Corrosion and wear resistance characteristics of NiCr coating by laser alloying with powder feeding on grey iron liner. *Wear*. 2006;**260**(11-12): 1349-1355. DOI: 10.1016/j.wear.2005.09.033

- [21] Ghaini FM, Ebrahimnia M, Gholizade S. Characteristics of cracks in heat affected zone of ductile cast iron in powder welding process. *Engineering Failure Analysis*. 2011;**18**(1):47-51. DOI: 10.1016/j.engfailanal.2010.08.002
- [22] Bhadeshia H. Phase transformations contributing to the properties of modern steels. *Bulletin of the Polish Academy of Sciences Technical Sciences*. 2010;**58**(2):255-265. DOI: 10.2478/v10175-010-0024-4
- [23] Ohta A, Suzuki N, Maeda Y, et al. Fatigue strength improvement of lap welded joints by low transition temperature welding wire—Superior improvement with strength of steel. *Welding in the World*. 2003;**47**(3–4):38-43. DOI: 10.1533/weli.18.2.112.27124
- [24] Hu LX, Dongpo W, Wenxian W, et al. Ultrasonic peening and low transition temperature electrodes used for improving the fatigue strength of welded joints. *Welding in the World*. 2004;**48**(3–4):34-39. DOI: 10.1007/BF03266425
- [25] Fang JX, Dong SY, Wang YJ, et al. The effect of solid-state phase transition upon stress evolution in laser metal powder deposition. *Materials & Design*. 2015;**87**:807-814. DOI: 10.1016/j.matdes.2015.08.061
- [26] Francis JA, Bhadeshia H, Withers PJ. Welding residual stresses in ferritic power plant steels. *Materials Science and Technology*. 2007;**23**(9):1009-1020. DOI: 10.1179/174328407X213116
- [27] Koistinen DP, Marburger RE. A general equation prescribing the extent of the austenite-martensite transition in pure iron-carbon alloys and plain carbon steels. *Acta Metallurgica*. 1959;**7**(1):59-60. DOI: 10.1016/0001-6160(59)90170-1

Residual Stress in Friction Stir Welding and Laser-Assisted Friction Stir Welding by Numerical Simulation and Experiments

Caterina Casavola, Alberto Cazzato and
Vincenzo Moramarco

Additional information is available at the end of the chapter

<http://dx.doi.org/10.5772/intechopen.72271>

Abstract

The friction stir welding (FSW) has become an important welding technique to join materials that are difficult to weld by traditional fusion welding technology. In this technique, the material is not led to fusion, and the joint is the result of the rotation and movement along the welding line of the tool that causes softening of material due to frictional heat and the stirring of the same. In FSW, the temperature does not reach the fusion value of the materials, and this helps to decrease the residual stress values. However, due to the higher force involved in the weld and, thus, the rigid clamping used, the residual stresses are not low in general in this technique. As the presence of high residual stress values influences the post-weld mechanical properties, e.g. fatigue properties, it is important to investigate the residual stress distribution in the FSW welds. In this chapter, two numerical models that predict temperatures and residual stresses in friction stir welding and laser-assisted friction stir welding will be described. Experimental measurements of temperatures and residual stress will be carried out to validate the prediction of the models.

Keywords: friction stir welding, laser-assisted friction stir welding, residual stress, thermography, X-ray diffraction

1. Introduction

Since 1991, when the process was initially developed, friction stir welding (FSW) has become a promising welding method for joining materials that would otherwise be hardly weldable by means of the conventional welding technology [1]. This important advantage is mainly due to the FSW nature of being a solid-state welding process. In fact, the material is not

fused, and the welding process is the result of the tool rotation and movement along the welding line that causes softening of material due to frictional heat and the stirring of the same. In FSW, the temperature does not reach the fusion value of the materials, and this helps to decrease the residual stress values. However, due to the higher force involved in the weld and, thus, the rigid clamping used, the residual stresses are not low in general in this technique. The constraints avoid the contraction of the materials during cooling in both longitudinal and transverse directions, thereby resulting in generation of longitudinal (parallel to welding direction) and transverse stresses (normal to welding direction). As the presence of high residual stress values influences the post-weld mechanical properties, e.g. fatigue properties, it is important to investigate the residual stress distribution in the FSW welds. Some studies have been carried out on residual stresses in FSW [1, 2–5]. In most of these, some similar conclusions can be highlighted. First, the residual stresses in FSW welds are lower than those generated during fusion welding, but they are not negligible at all. The low residual stress in the FSW welds has been attributed to the lower heat input during FSW and recrystallization accommodation of these stresses. Second, the transverse stresses are lower than the longitudinal ones, independent on tool rotation rate, traverse speed and pin diameter. Third, the distributions of the transverse and longitudinal residual stresses show an “M”-like trend across the welded joint. Moreover, in the advancing side, there is a higher residual stress peak [1].

This chapter will describe the temperature fields and residual stresses in both FSW and laser-assisted friction stir welding (LAFSW), evaluated by means of experimental measurements and finite element analysis. Two numerical models will be developed and validated on the experimental results of temperatures and residual stresses. Furthermore, besides a deeper knowledge of FSW, these numerical simulations have also the aim to guide the development of the process through the research of optimal parameters minimising the amount of trial and error.

2. The friction stir welding process

The FSW main idea is very simple. A rotating tool is inserted into the plates to be welded, and while rotating, it is moved along the welding line (**Figure 1**).

During the FSW process, the material undergoes a severe plastic deformation at elevated temperature. This generates a fine and equiaxed recrystallized grain structure that produces good mechanical properties [1, 6].

2.1. Process

The welding process is divided into four main steps: rotating, plunge and dwell, translation and exit. The tool starts to rotate before the plunge phase (**Figure 2a**). During the plunge phase, the tool penetrates the material, and subsequently, it is held in position for a few seconds while still rotating (**Figure 2b**). This phase is called dwell time, and the aim of this step is to heat and thus soften the material before welding. Then the tool moves along the joint line carrying out the weld (**Figure 2c**). Finally, the tool is pulled out from the material (**Figure 2d**).

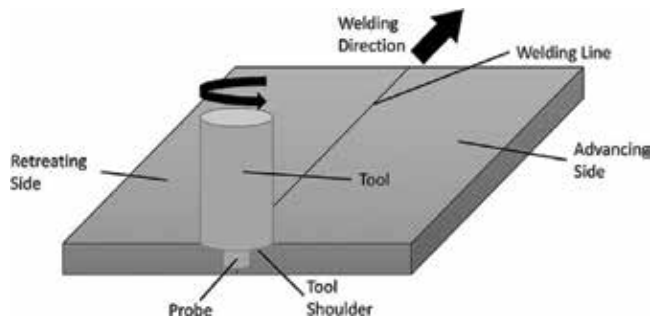


Figure 1. Scheme of friction stir welding process.

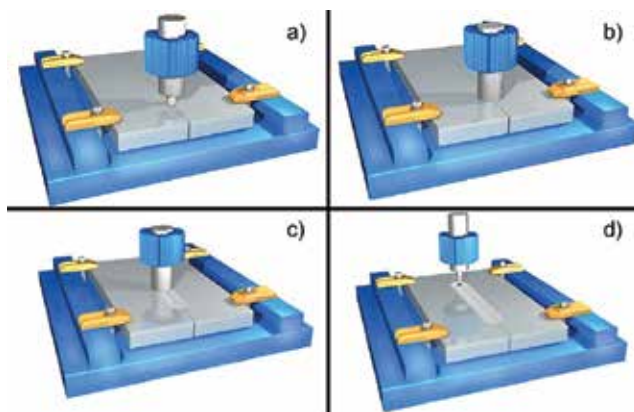


Figure 2. Scheme of FSW process steps: (a) rotating tool before plunging, (b) plunging and then tool shoulder touches the work piece surface producing frictional heat, (c) rotating tool traverses along the work piece and (d) pulling out from the workpiece.

The tool (Figure 1) has two main functions: heat the workpiece and move the material to produce the joint. The heat is produced mainly by the shoulder friction with the top surface of the workpiece. This softens the material to be welded. Moreover, the shoulder prevents expulsion of the material and guides the flow of the material during welding. The tool pin, in addition to being the secondary source of heat generation, provides the stirring action to the materials of the two plates to be joined [1]. FSW is mainly a mechanical process, and the forces involved in this type of work are relevant. Thus, the workpiece is placed on a thick backing plate and is clamped rigidly by strong fixture to eliminate any degrees of freedom.

2.2. Welding parameters

Two are the main parameters in FSW: tool rotation rate [rpm] and tool traverse speed [mm/min]. The rotation of tool controls the stirring and mixing action of the material, and the tool translation moves the stirred material from the front to the back of the pin. Higher tool rotation rates generate an increase of temperature due of higher friction heating and result in more intense stirring and mixing of material, but the frictional coupling of tool surface with

workpiece controls and governs the heating. Consequently, there is not a monotonic increase in heating with increasing tool rotation rate because the coefficient of friction at interface will change with the tool rotation rate.

Further, the insertion depth of pin into the workpieces (in position control mode) or the downward force on the tool (in force control mode) is important for producing good welds. When these parameters are not correct, the shoulder of tool may not contact the workpiece surface or create excessive flash around the welds.

In addition, preheating or cooling can also be important for some FSW processes. For example, in materials with high melting point such as steel or titanium, the heat produced by friction and stirring may be not sufficient to soften and plasticize the material around the tool. In these cases, preheating or an additional external heating source, e.g. laser, can help the material flow and widen the process window [1].

2.3. Laser-assisted friction stir welding

In this technique, a defocused laser beam precedes the FSW tool during welding at a distance between 10 and 40 mm, increasing the temperatures reached in front of the tool and allowing an easier advancement of the same. In **Figure 3**, a scheme of the LAFSW setup has been reported.

The commonly used laser sources are diode laser, Nd:YAG fibre optic laser and CO₂ laser. The laser spot is activated just before the plunging stage or at the start of the welding phase of FSW [7]. The assistance of the laser in FSW is an attractive way to preheat the material with a conventional FSW setup. This technique has been employed to weld a variety of light alloys, high-strength alloys and dissimilar alloys. The higher heat input allows a better material plasticisation and grain refinements that improve the material flow and the mechanical properties. The better plasticisation should help also to reduce the downward axial force, the tool wear and increase welding speed [7].

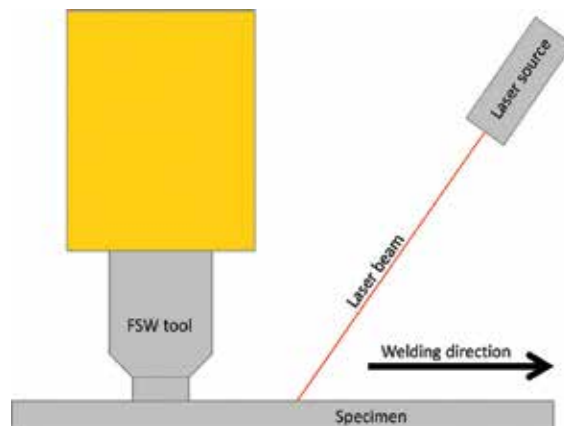


Figure 3. Scheme of the LAFSW setup.

3. Temperature field in FSW and laser-assisted FSW processes

The temperature distributions and the thermal histories have a key role in FSW and LAFSW. They determine whether the welding process will produce a good weld, influencing the residual stresses, the microstructure and the strength of welds. Several studies have measured temperatures in FSW using thermocouples [8–10], but only a few have been involved in experimental analysis using thermography [9] and still less on laser-assisted friction stir welding. Employing thermocouples, Xu et al. [8] showed that the temperature decreases with decreasing the transverse speed and increases with increasing the rotational speed. Moreover, they noted that the distribution of the temperatures in the plunge phase is correlated only to the rotational tool speed. Finally, they showed that mechanical properties such as the yield and tensile strengths of the welded plate are related to the process parameters. Increasing the rotational tool speed increases yield and tensile strengths, while the elongation decreases. Hwang et al. [9] conducted a study on temperature distribution using thermocouples and find out that the temperatures on the advancing side are slightly higher than those on the retreating side. Also, Maeda et al. [10] have applied thermocouples on both top and bottom surfaces of the work plates and have found an asymmetric temperature distribution between the advancing side and the retreating side.

Although experimental measures are fundamental to understand the thermal phenomenon in the FSW process and LAFSW, they present some limitations, (e.g. economic costs or internal temperature measurements). For this reason, the implementation of numerical models that can predict the temperature distributions has a significant role to estimate the correct weld parameters, to improve mechanical properties of the welded joints and reduce the amount of trials and errors.

In the next section, the experimental setup employed to measure the temperature field on both FSW and LAFSW will be described. These experiments will be used for the validation of the numerical models that will be described later.

3.1. Thermographic analysis of FSW and laser-assisted FSW

A NEC H2640 infrared camera with configurable ranges between -40 and 2000°C , a resolution of 0.06°C , an accuracy of $\pm 2^{\circ}\text{C}$ and a spectral range of $8\text{--}13\ \mu\text{m}$ has been used to acquire the temperature during the welding process. **Figure 4** shows the experimental setup of the thermal camera.

The angle between the FSW tool axis and the camera has been set to 30° . In order to reduce problems related to the low emissivity of aluminium and reflection, the specimen has been painted with matte black acrylic spray paint. An emissivity $\varepsilon = 0.95$ has been set on the camera.

When the specimens have to be mechanically tested after the welding process, the central zone of the specimen has not been painted to avoid paint inclusion into the welded joint. This allows to acquire correctly the temperature near the tool, but not influencing the mechanical characteristics of the joints. However, when there is the necessity to acquire the temperatures in front of the tool, e.g. in LAFSW, the specimens have been completely painted, and bead-on-plate welds have been done. Consequently, no mechanical tests have been done on this typology



Figure 4. Thermographic experimental setup.

of specimens. Temperature measurements have been carried out on the retreating side of the welded plate because the configuration of the FSW machine prevents access to both sides.

3.2. Numerical prediction of temperature fields in FSW and LAFSW

3.2.1. FSW model description

Finite element analysis, by means of software ANSYS 14.5, has been implemented to develop a 3D transient thermal model and simulate the FSW thermal history. Due to the symmetry of the problem, a half plate model has been simulated to decrease the element number and reduce the computational time. The model has been meshed using 6000 SOLID90 elements. A thicker mesh has been employed near the welding line (**Figure 5**) to describe in a more accurate way the thermal behaviour near the tool area and to consider the higher gradient of temperature. The natural convection on the top surface and on the lateral side of the specimen has been set to $20 \text{ W/m}^2 \text{ } ^\circ\text{C}$. Moreover, a convection coefficient of $300 \text{ W/m}^2 \text{ } ^\circ\text{C}$ has been employed to simulate the conduction between the backing plate and bottom surface of the specimen. The specific value of the convection coefficient has been employed to match the maximum temperature, reached during the weld process, between the experimental data and the numerical model.

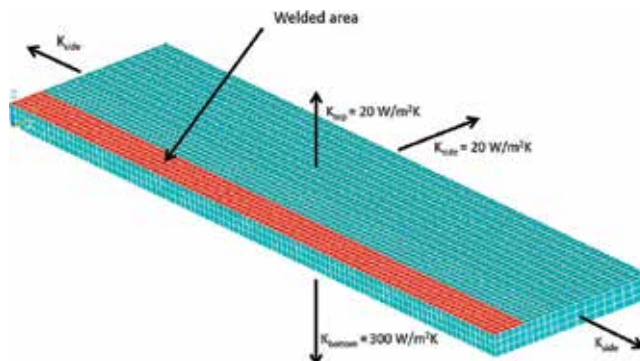


Figure 5. FSW model mesh and convection coefficient.

In the numerical model, as the temperature does not exceed 500°C, the heat lost by radiation has not been considered [11].

The AA5754 thermo-physical material properties (i.e. thermal conductivity and specific heat) have been implemented as a function of temperature [12]. Due to a lack of literature data, the density of the material has been kept constant with the temperature.

The welding process has been simulated by a moving thermal source along the welded zone. According to Schmidt et al. [13, 14], the analytical expression used for simulating FSW tool heat generation is reported in Eq. (1):

$$Q = \frac{2}{3} \mu \omega \frac{F_n}{R_{shoulder}^2} \left((R_{shoulder}^3 - R_{probe}^3) (1 + \tan \alpha) + R_{probe}^3 + 3 R_{probe}^2 H_{probe} \right) \quad (1)$$

The R_{probe} and $R_{shoulder}$ are the pin and shoulder radius of the tool (Eq. (1), **Figure 6**). H_{probe} and α are the pin height and the shoulder concavity angle. Moreover, F_n , ω and μ are the normal plunge force, the rotational speed and the friction coefficient, respectively. The μ coefficient has been set to 0.3 according with Schmidt et al. papers [13, 14]. The remaining terms in the equation are $R_{shoulder}$ 10.75 mm, R_{probe} 3 mm, $\alpha = 0^\circ$ and H_{probe} 5.8 mm. The traverse speed has been set to 20 cm/min, the rotational speed to 500 RPM and the normal force F_n to 20,000 N in accordance with the process parameters.

3.2.2. Results and discussion for FSW model

The verification and validation of the previously described FSW model have been carried out on bead-on-plate welds. The studies have been regarded three steps (**Figure 7**) of the welding process. During each step, the numerical and experimental temperature data have been acquired and compared. In particular, the start phase is the welding initial step where the

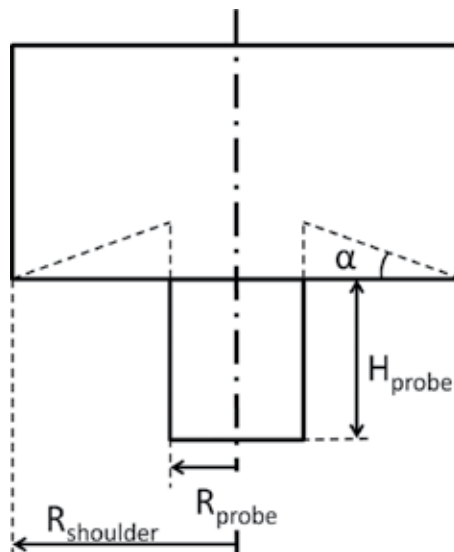


Figure 6. Tool geometry scheme.

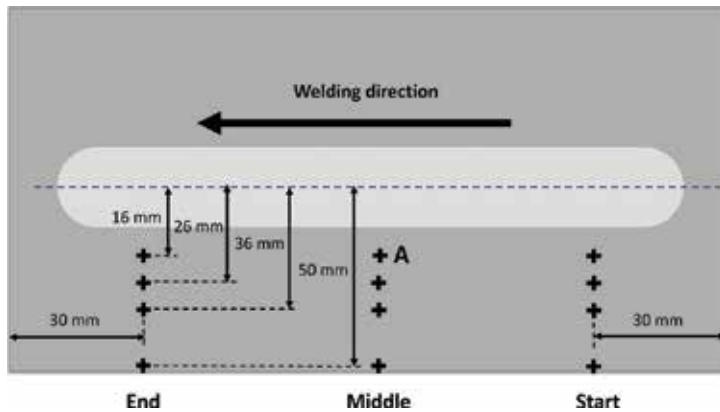


Figure 7. Location scheme of experimental measured points.

FSW tool is at about 30 mm from the edge of the plate. The middle step is in the half of the specimen, and finally, the end phase is at 30 mm from the left edge of the plate.

The graphs of the maximum temperatures versus distance from the weld line, for both experimental and numerical data, have been plotted in **Figure 8a–c**. The trends highlight that the estimation of the numerical model agrees with the experimental data. Indeed, in the start phase (**Figure 8a**), the maximum error between experimental and numerical data is 5.9%; in the middle step, it is 6.2% (**Figure 8b**) and in the end step (**Figure 8c**), the error is 6.3%. In order to accurately validate the numerical model, in **Figure 8d**, the temperature vs. time of the numerical model and experimental data for the point A in **Figure 7** has been reported. The trends are in good agreement though there are some small differences in the cooling phase. These differences are due to the use of heat convection instead of conduction in the numerical simulation of the contact between backing plate and specimen. Finally, the model is validated, and its results are good (37.1% of maximum error) considering all the parameters, such as coefficient of convection, friction coefficient and variability of normal force, that are difficult to consider.

Figure 9 shows the comparison between the numerical isothermals at the top surface of the specimen and the image of the surface temperature distribution taken by the infrared camera.

The white area in this figure describes the zone of the plate where the temperature exceeds 250°C. Overall, there is a good agreement between the numerical and experimental data on the whole plate. Only in the area near the clamping system, not implemented in the FEM model, the surface temperature is slightly different.

3.2.3. Laser-assisted FSW model description

The LAFSW numerical simulation is based on the previously described FSW model. However, beyond the adding of the laser source, some other improvements have been done, e.g. the adding of a backing plate to simulate in a better way the cooling phase. The same temperature-dependent thermo-physical properties of the previously described model have been

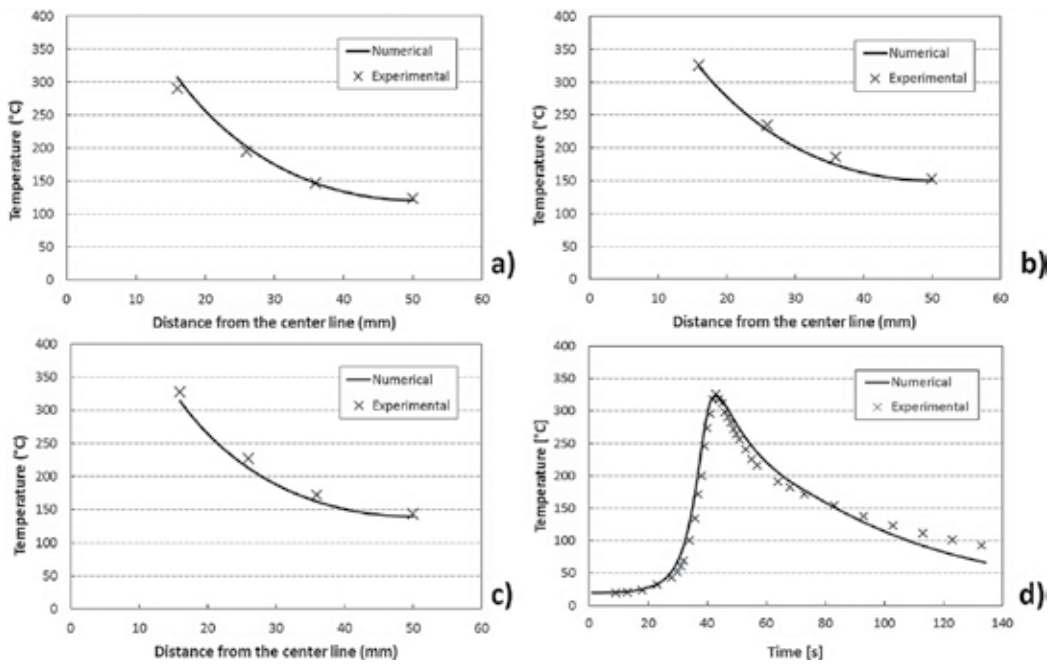


Figure 8. Temperature trend in the start phase (a), in the middle phase (b) and in the end phase (c) and temperature vs. time of a middle point distant 16 mm from the centre line (d) for FSW.

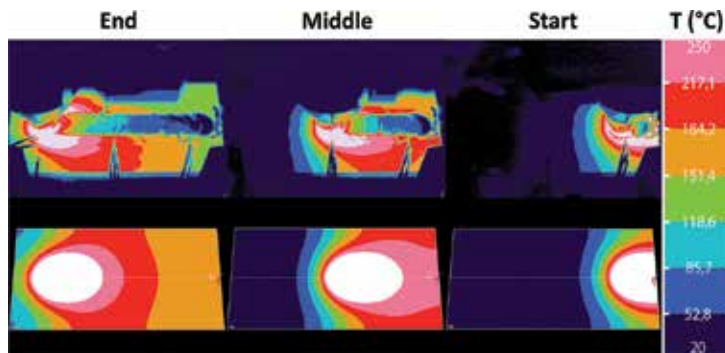


Figure 9. Graphical comparison between numerical data and the experimental ones for FSW.

used [12], and also in this case, only half plate has been simulated to reduce the computational time. The process parameters for the FSW are the same of the previous models. The laser power has been set to 500 W, and the distance of FSW tool-laser spot is 40 mm. A gradual thicker mesh of SOLID90 elements has been adopted near the welding line to describe more accurately the thermal behaviour where the temperature gradient is higher (Figure 10). The natural convection between aluminium and air has been set to $20 \text{ W/m}^2 \text{ } ^\circ\text{C}$ on the top surface and on the lateral side of the specimen. In this model, in different manners of the previous model, the interface between the backing plate and the specimen has been simulated

employing the conduction (**Figure 10**). A coefficient of $450 \text{ W/m}^2 \text{ }^\circ\text{C}$ has been used to simulate the conduction between the backing plate (a $400 \text{ mm} \times 400 \text{ mm} \times 10 \text{ mm}$ FE360 steel plate) and bottom surface of the specimen. The specific value of the conduction coefficient has been employed to match the maximum temperature, reached during the weld process, between the experimental data and the numerical model.

As in the previous FSW model, the welding process has been modelled as a uniform thermal source. However, while F_n is the same as the previous model, the friction coefficient μ has been set equal to 0.237 according to the experimental tests. Finally, the laser source has been simulated as a uniform heat source of 2 mm radius that moves together to FSW tool.

3.2.4. Result and discussion for laser-assisted FSW model

As in the previously shown results for FSW, also in this case, three different steps have been studied and reported in the later graphs. As in the previous model, the middle step is in the middle of the plate; instead, the start position and the end position are at 65 mm from the right and left plate edges, respectively. The temperature has been acquired at 16, 26, 36 and 50 mm from the welding line for each of the three steps. The trends of the temperature versus distance from the weld line have been plotted for numerical and experimental data in the start (**Figure 11a**), middle (**Figure 11b**) and end (**Figure 11c**) phases. Generally, these graphs show that the numerical model fits the experimental data with low errors. This is confirmed by R^2 value that is 0.992 in the start step, 0.999 in the middle phase and, finally, 0.999 in the end step. In **Figure 10d**, the temperature versus time of the experimental data and the numerical model has been reported. This graph represents the temperatures of a central point distant 16 mm from the welding line. In general, there is a good agreement between the numerical model and the experimental data, and compared to the previous model, the adding of the baking plate improves the cooling phase prediction (**Figure 8d** vs. **Figure 11d**).

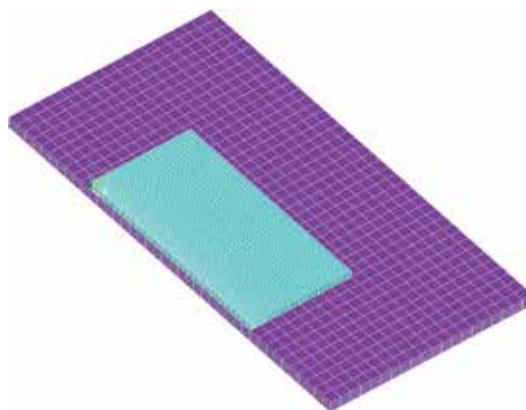


Figure 10. LAFSW scheme of model mesh.

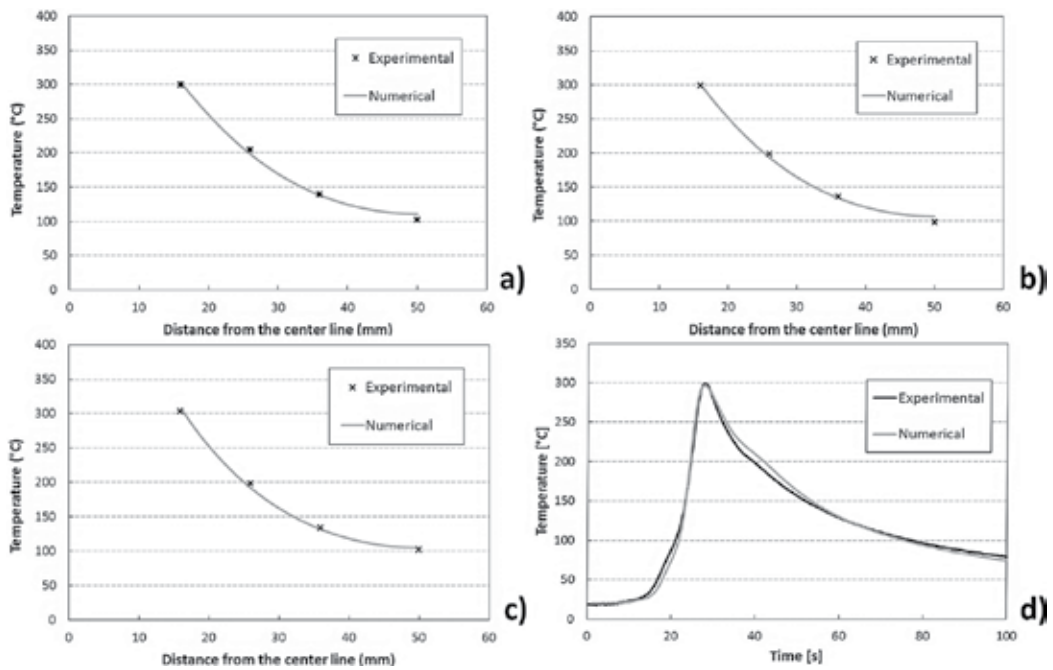


Figure 11. Temperature trend in the start phase (a), in the middle phase (b) and in the end phase (c) and temperature vs. time of a middle point distant 16 mm from the centre line (d) for LAFSW.

The value of the thermal contact conductance coefficient, between the aluminium specimens and the backing plate, has been selected to fit the numerical maximum temperature in the point A with the experimental data.

In **Figure 12**, a qualitative comparison of thermal field measured experimentally and that obtained numerically has been reported. Moreover, the temperature of welded area behind the FSW tool is not correct because there is a variation of the emissivity due to the paint removal and change of roughness after the transit of FSW tool.

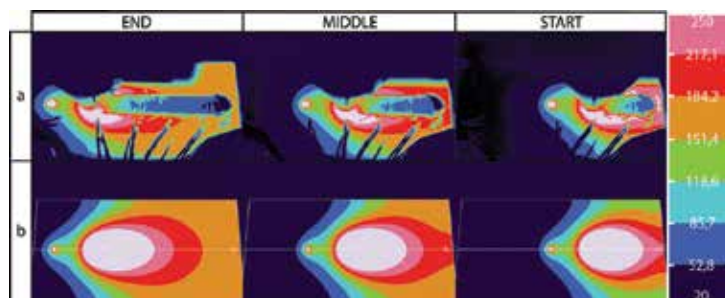


Figure 12. Graphical comparison between the experimental data (a) and numerical results (b) for LAFSW.

4. Residual stresses in FSW and LAFSW processes

Residual stresses have a fundamental role in welded structures because they affect the mechanical response of parts (i.e. corrosion resistance, fatigue life and many other material characteristics). Residual stress distribution, also in FSW process where, though the heat input is lower than traditional welding techniques, the constraints applied to the parts to weld are more severe, should be deeply studied.

Technical literature reports numerous research papers that deal with the experimental evaluation of residual stress distribution in FSW joints. Dalle Donne et al. [15], employing different techniques, have measured residual stress distribution on FSW 2024Al-T3 and 6013Al-T6 joints. They have shown that longitudinal and transverse residual stresses have a “M”-like distribution across the weld. Moreover, the longitudinal residual stresses are higher than the transverse ones regardless on traverse speed, tool rotation speed and pin diameter. Peel et al. [3], employing synchrotron X-ray method, have measured the residual stress in FSW AA5083 welded joints. The results show that there is a tension state in the weld bead in both longitudinal and transverse residual stress directions. Furthermore, they have proven that the longitudinal stresses increase with increasing the traverse speed. Sutton et al. [16] and also Donne et al. have proven that the longitudinal is the most important component in the residual stresses analysis in FSW process and that the transverse is about 70% of the longitudinal component.

In order to have a wider understanding of the FSW process, some researchers have recently simulated the FSW process by numerical models. Moreover, these numerical models have also the aim to develop the process through the research of optimal parameters minimising the amount of trial and error. Khandkar et al. [17] have made an uncoupled thermo-mechanical model for some aluminium alloys and 304 L stainless steel based on torque input for calculating temperature and then residual stress. Chen et al. [18] have developed a 3D numerical model to study the thermal impact and evolution of the residual stresses in the welded joints. However, the previously described numerical simulations are only thermal or thermomechanical models in which, for example, the tool mechanical force is not considered. These effects are important and should be included into the thermo-mechanical simulations.

Though many works on measuring residual stresses in FSW have been done, few works have been carried out on measuring or simulating residual stresses in innovative techniques, such as LAFSW. In the next section, the measurement of residual stresses in FSW and LAFSW will be presented, and the results will be useful to validate the FSW and LAFSW numerical models.

4.1. Residual stress measurements in FSW and LAFSW

FSW and LAFSW tests were conducted on 6-mm thick 5754 H111 aluminium alloy plates, in butt joint configuration. Two rectangular plates, 200 mm × 100 mm, have been welded perpendicular to the rolling direction. The welding process is the same in the previous sections.

A Xstress 3000 G3R Stresstech X-ray diffractometer has been employed to measure the residual stresses. 30 kV and 8 mA of current have been used to power a Cr tube ($\lambda = 0.2291$ nm). An angle of 156.7° has been selected as 2θ diffraction angle, and five ϕ different angles ($0, \pm 22.5, \pm 45^\circ$) with an oscillation of $\pm 3^\circ$ have been employed to increase the quality of the measures. The residual stresses, both longitudinal (x-axis direction) and transverse (y-axis direction), have been carried out along the centre line of the specimens, i.e. the line normal to the welding line in the middle of the plate.

4.2. Numerical prediction of residual stresses in FSW

4.2.1. Numerical model description

An uncoupled FE model has been carried out to calculate residual stress field. The first step has been to carry out a thermal analysis to simulate the temperature history related to the welding process. Then, the calculated temperature field has been used as thermal input to the mechanical model to predict the residual stresses and strains. This analysis has been implemented by means of FE software ANSYS 14.5. The thermal simulation is based on the previously presented model modified to describe the welding process of two $200 \text{ mm} \times 100 \text{ mm}$ plates in butt-weld configuration. With the aim of an accurate simulation of residual thermal stresses, beyond the temperature-dependent thermophysical properties, also temperature-dependent thermomechanical properties have been used [13]. It is worth noting that enthalpy values are not considered in the simulation, as the FSW is a solid-state welding method and there is no material melting. Moreover, a multilinear isotropic hardening has been employed to describe the material behaviour.

In order to calculate the residual stresses, the thermal histories simulated by the FE thermal model have been inputted in the mechanical simulation. To this aim, the SOLID186 elements have been employed instead of the SOLID90 elements, keeping the same load step and mesh size. Moreover, to simulate the mechanical effect due to the compression force applied by the tool, a uniform axial pressure distributed on tool area has been included in the FE mechanical model. The mechanical constraints have been set according with experimental setup. Once that the welding simulation is concluded, the constraints are gradually released, and the residual stresses due to FSW process have been evaluated.

The FSW has been carried out perpendicular to the rolling direction of the AA5754 sheets. As the layout of the FSW machine does not allow an easy access to both side of the plate, the temperature measurement, residual stresses analysis and numerical simulation have been executed in the retreating side of the plate.

4.2.2. Results and discussion

Numerical model has been validated on both temperatures and stresses on the actual case in order to obtain reliable stress values in the simulated case. To reach this aim, the temperature field of the specimen has been measured during the FSW test by an infrared thermo-camera. In the same way, as in the Section 3.2.2, the recorded values have been compared with the data calculated by the numerical model in three different positions when maximum. The middle

step is in the half of the plate; instead, the start position and the end position are at 50 mm from the right and left plate edges, respectively. The temperature has been acquired at 16, 36, 80 and 100 mm from the welding line for each of the three steps. In **Figure 13**, the graphs of the temperature versus distance from the weld line have been plotted both for numerical and experimental data. Generally, the numerical results show a good agreement with the experimental measurements. This is confirmed by R^2 that is 0.997 in the start step (**Figure 13a**), 0.999 in the middle phase (**Figure 13b**) and, finally, 0.991 in the end step (**Figure 13c**). The graph of temperature vs. time for both experimental and numerical data (of the A point in **Figure 7**) has been reported in **Figure 13d**. In general, the trends of experimental and the numerical data are in good agreement with some small difference in the cooling phase as already explained previously.

The mechanical part of the model has been validated based on the X-ray diffraction stress-measured data. In **Figure 14** the stress in the welding direction, i.e. the longitudinal stress, has been reported and compared with the numerical values. The longitudinal stress shows a “M”-like distribution across the weld, and moreover, the maximum stress value in a FSW weld is located on the edge of the bead described in **Figure 14** by the vertical grey line at 10.75 mm from the welding line.

The residual stresses in the transverse direction, for both experimental and numerical data, have been reported in **Figure 15**. The transverse residual stress values are roughly constant in the plate with a value of 60 MPa and, in agreement with Sutton et al. [16], are about 70% of the longitudinal one.

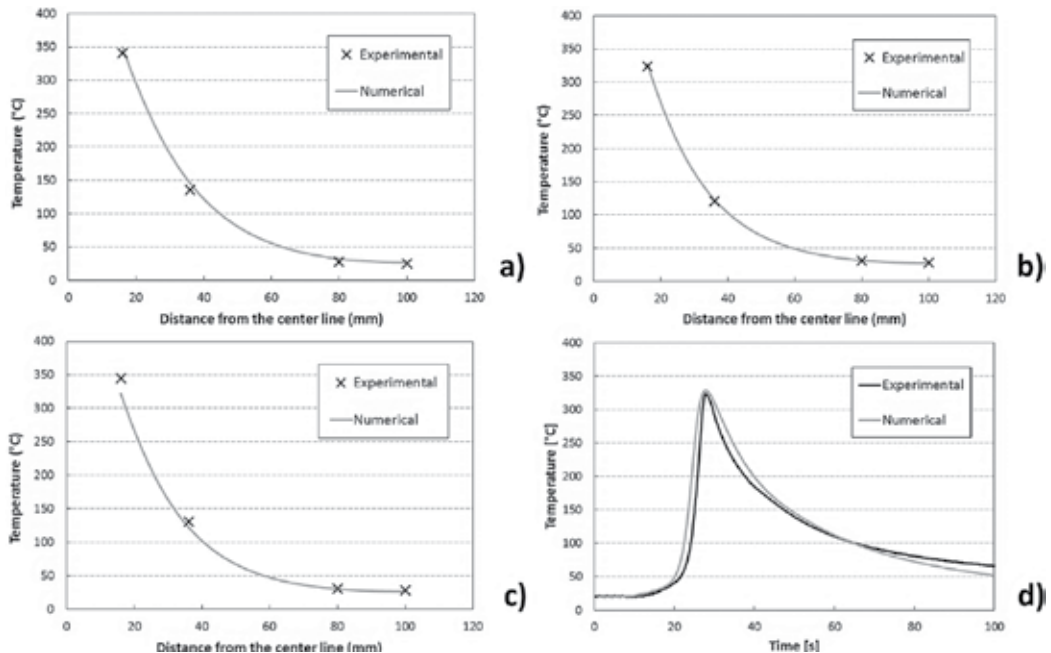


Figure 13. Temperature trend in the start phase (a), in the middle phase (b) and in the end phase (c) and temperature vs. time of a middle point distant 16 mm from the centre line (d) for FSW.

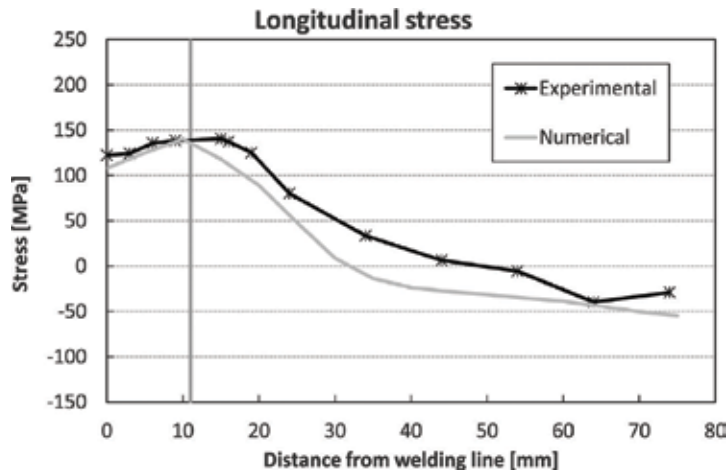


Figure 14. Numerical vs. experimental comparison of longitudinal stress in FSW.

The residual stress results show a good agreement between experimental and numerical data, although some little discrepancies exist. These are located away from the welding line where the initial residual stresses of the plate are preponderant. In the numerical model, the initial state of the plate is difficult to consider and to simulate.

4.3. Numerical prediction of residual stresses in LAFSW

4.3.1. Numerical model description

The mechanical part of the LAFSW model is based on the thermal model described in Section 3.2.3, but to the previously described thermal model, it has been added the

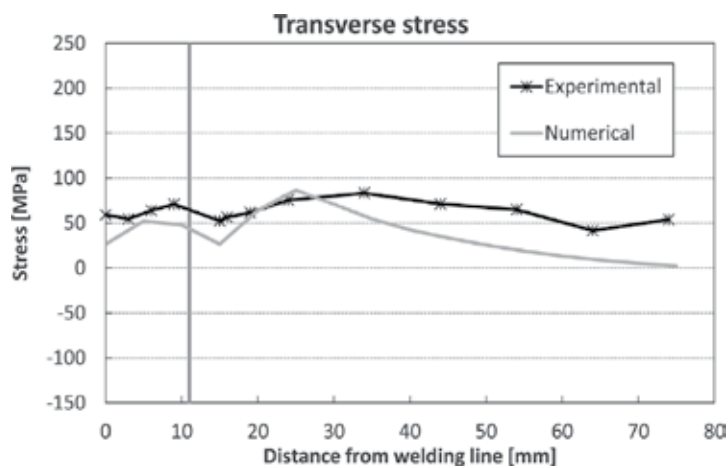


Figure 15. Numerical vs. experimental comparison of transverse stress in FSW.

mechanical part which employs the thermal data as an input to the mechanical model. However, as explained previously, the LAFSW has been validated on a bead-on-plate configuration to capture also the temperature in front of the tool. To validate the residual stress model, it is necessary to carry out the measurements on real butt-weld configuration. In order to solve this problem, once the numerical model has been validated (see Section 3.2.4), it has been implemented on the basis of the actual welding setup simulating the joining of two 200 mm × 100 mm plates. The new temperature distribution has been inputted to the mechanical part of the model to simulate the residual stresses in the actual configuration. Finally, the experimental data have been compared to the numerical residual stress values.

The same procedure to pass the temperature data from the thermal model to the mechanical part as an input, explained in Section 4.2.1, has been also employed in this model. Also in this case, the mechanical constraints have been set according to experimental setup, and once that the welding simulation is concluded, the constraints are gradually released, and the residual stresses due to LAFSW process have been evaluated.

4.3.2. Results and discussion

In **Figure 16**, the numerical versus experimental longitudinal stress trend has been reported for the retreating side. Also in this case, the maximum stress value in the LAFSW welds is located on the edge of the bead as has been shown in **Figure 16** by a vertical grey line at 10.75 mm from the joining line.

The transverse residual stress trend has been reported in **Figure 17**. This trend shows, for both experimental and numerical data, that the transverse residual stress values are roughly constant in the plate and that there is a good agreement between numerical and experimental results. However, the effect of the laser is visible in the welded zone where there is a small increment of the residual stress values.

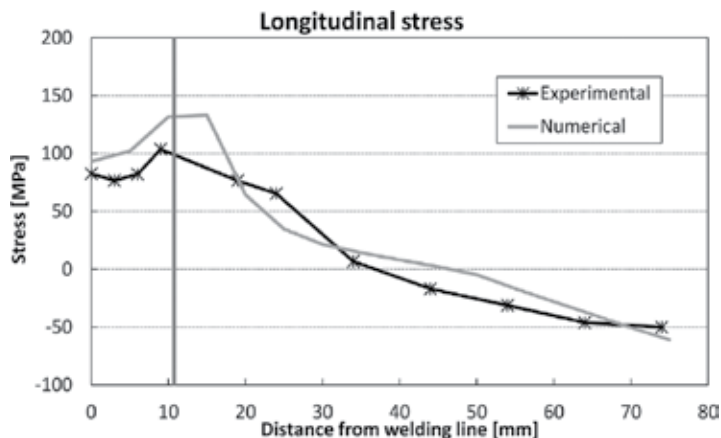


Figure 16. Numerical vs. experimental comparison of longitudinal stress for LAFSW.

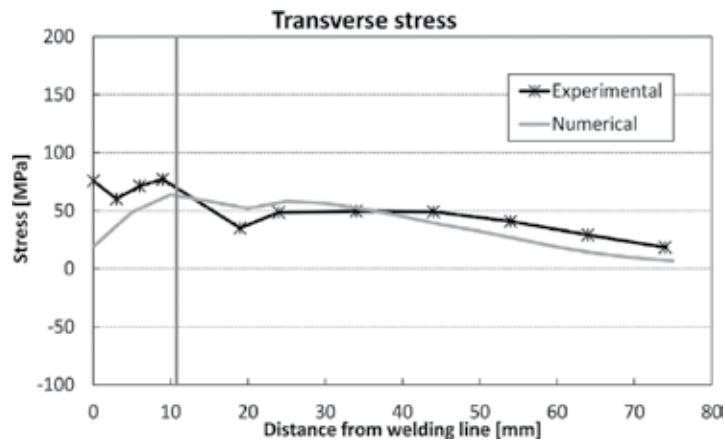


Figure 17. Numerical vs. experimental comparison of transverse stress for LAFSW.

5. Summary and conclusions

In this chapter, two 3D thermo-mechanical models have been developed in order to predict temperatures and residual stresses in friction stir welding and laser-assisted FSW. These models include the mechanical action of the shoulder and the thermo-mechanical characteristic of AA5754 at different temperatures. Thermographic analysis of FSW and LAFSW process and residual stress measurement by X-ray diffraction has been carried out to validate the model thermally and mechanically.

The results for both the numerical models and experimental data show that the longitudinal stress presents a “M”-like distribution across the weld, and moreover, the maximum stress value in a FSW and LAFSW weld is located on the edge of the bead. The stress in the transverse direction is roughly constant with values between 50 and 60 MPa along all the transverse directions of the plate. Moreover, according to the observations reported by Sutton et al. [16], the transverse stress has lower values than longitudinal stress and it is about 70% of the this one.

Although some little discrepancies exist between the simulated numerical values and the measured ones, the distribution of the residual stress, both longitudinal and transverse, shows a good agreement with the experimental results for both FSW and LAFSW models. However, away from the welding line, there is the maximum difference between numerical and experimental data for both longitudinal and transverse stresses. This could be explained considering that the initial residual stress in the numerical model is difficult to consider. Indeed, away from the welding line, the influence of the welding process is minimal, and the residual stress trend should tend to the pre-weld value.

In conclusion, the importance of the prediction and measurement of residual stress in FSW and LAFSW has been highlighted. Though the FSW is a solid-state welding process, the residual stresses are not low in general, and the influence of these stresses on the mechanical behaviour of the FSW joints should be considered.

As a future development of this work, the authors are improving the described models and Eq. (1) to consider and predict the differences in the temperatures and, thus, in the residual stresses between advancing and retreating sides. These differences change in accordance to the traverse and the rotating tool speeds due to the concordance and discordance between the travel and the rotating tool directions in, respectively, the advancing and the retreating sides.

Author details

Caterina Casavola*, Alberto Cazzato and Vincenzo Moramarco

*Address all correspondence to: casavola@poliba.it

Department of Mechanics, Mathematics and Management, Polytechnic University of Bari, Bari, Italy

References

- [1] Mishra RS, Ma ZY. Friction stir welding and processing. *Materials Science and Engineering: R: Reports*. 2005;**50**(1-2):1-78
- [2] Reynolds AP, Tang W, Gnaupel-Herold T, Prask H. Structure, properties, and residual stress of 304L stainless steel friction stir welds. *Scripta Materialia*. 2003;**48**(9):1289-1294
- [3] Peel M, Steuwer A, Preuss M, Withers PJ. Microstructure, mechanical properties and residual stresses as a function of welding speed in aluminium AA5083 friction stir welds. *Acta Materialia*. 2003;**51**(16):4791-4801
- [4] Prime MB, Gnäupel-Herold T, Baumann JA, Lederich RJ, Bowden DM, Sebring RJ. Residual stress measurements in a thick, dissimilar aluminum alloy friction stir weld. *Acta Materialia*. 2006;**54**(15):4013-4021
- [5] Darvazi AR, Iranmanesh M. Prediction of asymmetric transient temperature and longitudinal residual stress in friction stir welding of 304L stainless steel. *Materials & Design*. 2014;**55**:812-820
- [6] Rhodes CG, Mahoney MW, Bingel WH, Spurling RA, Bampton CC. Effects of friction stir welding on microstructure of 7075 aluminum. *Scripta Materialia*. 1997;**36**(1):69-75
- [7] Padhy G, Wu C, Gao S. Auxiliary energy assisted friction stir welding – Status review. *Science and Technology of Welding and Joining*. 2015;**20**(8):631-649
- [8] Xu W, Liu J, Luan G, Dong C. Temperature evolution, microstructure and mechanical properties of friction stir welded thick 2219-O aluminum alloy joints. *Materials & Design*. 2009;**30**(6):1886-1893
- [9] Hwang YM, Kang ZW, Chiou YC, Hsu HH. Experimental study on temperature distributions within the workpiece during friction stir welding of aluminum alloys. *International Journal of Machine Tools and Manufacture*. 2008;**48**(7-8):778-787

- [10] Maedaa M, Liub H, Fujiib H, Shibayanagib T. Temperature field in the vicinity of FSW-tool during friction stir welding of Aluminium alloys. *Welding in the World*. 2005;**49**(3):69-75
- [11] Chao YJ, Qi X, Tang W. Heat transfer in friction stir welding – Experimental and numerical studies. *Journal of Manufacturing Science and Engineering*. 2003;**125**(1):138-145
- [12] Khanna SK, Long X, Porter WD, Wang H, Liu CK, Radovic M, Lara-Curzio E. Residual stresses in spot welded new generation aluminium alloys part A–thermophysical and thermomechanical properties of 6111 and 5754 aluminium alloys. *Science and Technology of Welding & Joining*. 2013;**10**(1):82-87
- [13] Schmidt HB, Hattel JH. Thermal modelling of friction stir welding. *Scripta Materialia*. 2008;**58**(5):332-337
- [14] Schmidt H, Hattel J, Wert J. An analytical model for the heat generation in friction stir welding. *Modelling and Simulation in Materials Science and Engineering*. 2004;**12**(1):143
- [15] Dalle Donne C, Lima E, Wegener J, Pyzalla A, Buslaps T. Investigations on residual stresses in friction stir welds. In: 3rd International Symposium on Friction Stir Welding; 27-28 September 2001; Kobe (Japan). TWI, Cambridge (UK); 2001. pp. 1-10
- [16] Sutton MA, Reynolds AP, Wang DQ, Hubbard CRA. Study of residual stresses and microstructure in 2024-T3 aluminum friction stir butt welds. *Journal of Engineering Materials and Technology*. 2002;**124**(2):215-221
- [17] Khandkar MZH, Khan JA, Reynolds AP, Sutton MA. Predicting residual thermal stresses in friction stir welded metals. *Journal of Materials Processing Technology*. 2006;**174**(1):195-203
- [18] Chen C, Kovacevic R. Finite element modeling of friction stir welding – Thermal and thermomechanical analysis. *International Journal of Machine Tools and Manufacture*. 2003;**43**(13):1319-1326

Residual Stress Pattern Prediction in Spray Transfer Multipass Welding by Means of Numerical Simulation

Jon Ander Esnaola, Ibai Ulacia,
Arkaitz Lopez-Jauregi and Done Ugarte

Additional information is available at the end of the chapter

<http://dx.doi.org/10.5772/intechopen.72134>

Abstract

One of the main problems of gas metal arc welding (GMAW) process is the generation of residual stresses (RS), which has a direct impact on the mechanical performance of welded components. Nevertheless, RS pattern prediction is complex and requires the simulation of the welding process. Consequently, most of the currently used dimensioning approaches do not consider RS, leading to design oversized structures. This fact is especially relevant in big structures since it generates high material, manufacturing and product transportation costs. Nowadays, there are different numerical methods to predict the RS generated in GMAW process, being Goldak's method one of the most widely used model. However, the use of these methods during the design process is limited, as they require experimentally defining many parameters. Alternatively, in this chapter, a new methodology to define the heat source energy based on the spray welding physics is exposed. The experimental validation of the methodology conducted for a multipass butt weld case shows good agreement in both the temperature pattern (9.16% deviation) and the RS pattern (42 MPa deviation). Finally, the proposed methodology is extended to analyse the influence of the thickness and the number of passes in the RS pattern of thick T-joint welds.

Keywords: multipass welding, analytic procedure, finite element method, equivalent heat source, temperature distribution, residual stresses

1. Introduction

Gas metal arc welding (GMAW, also referred as metal inert gas (MIG)), is one of the most extended welding techniques in metal manufacturing industry [1, 2]. Particularly, multipass

welding in spray transfer mode presents uniform metal transfer to workpiece at high rate, together with high arc stability and low weld spatter. For this reason, spray transfer mode is especially adequate to join thick plate structures [3, 4].

Nevertheless, one of the main drawbacks of welded structures is the generation of residual stresses (RS), which may compromise their mechanical performance. RS are generated due to high thermal cycles in the welding process where non-uniform heating and cooling occur [5, 6]. High thermal gradients generate inhomogeneous thermal expansion constrained by the surrounding material, which presents temperature-dependent mechanical properties. This way, the material at lower temperature suffers lower thermal expansion and presents higher strength. Thus, they also limit the expansion of adjacent areas at higher temperature which, in addition, present lower strength and, consequently, can suffer compressive plastic deformation. Finally, during the cooling down process, the areas yielded at high temperature constrain the elastic springback of not yielded areas generating internal stresses that remain on the welded component. This RS can be tractive or compressive depending on the constraints transmitted from the adjacent areas. As a result, tensile and compressive areas as well as the magnitude of the final RS pattern depend on several factors such as structural dimension, welding sequence, preparation of the weld groove, mechanical restraints or the number of weld passes [7–9]. In general, tensile residual stresses are considered detrimental because they increase the susceptibility of the welded joint to fatigue damage, stress-cracking corrosion (SCC), structural buckling and brittle fracture [6, 10, 11].

Figure 1 shows an example of the RS evolution of a determined point (dx, dy) of a plate near the weld seam depending on the thermal history subjected during the welding process of a

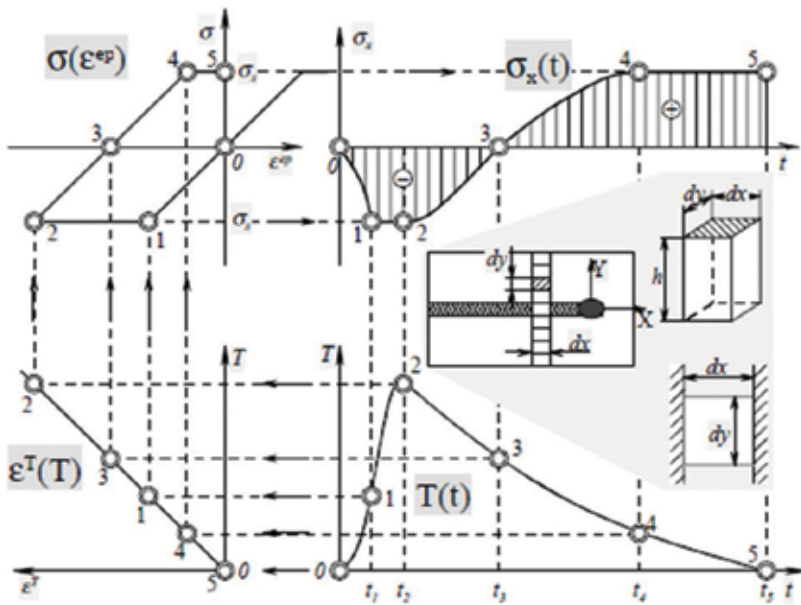


Figure 1. Schematic of the RS generation in a generic point nearby the welded seam [12].

butt weld [12]. It can be observed that from instant t_0 to t_2 , the material is heated up as the welding torch passes nearby trying to expand. The constraints of the surrounding material limit its expansion in x direction up to ε^T , and the initially stress-free material is compressed yielding at σ_1 and suffering elastic-plastic deformation ε^{ep} at high temperature T_2 up to σ_2 . Then, during the cooling down process from instant t_2 to instant t_5 , the elastic recovery from thermal expansion is limited by the surrounding material. Consequently, tensile stress that yields at σ_4 is generated suffering plastic deformation up to σ_5 .

Figure 2 compares the RS pattern variation near the weld toe for a butt weld case depending on the plate size and welding deposition rate. It can be observed that the distribution and magnitude of tractive and compressive stresses completely changes when modifying any of the selected parameters [13].

Due to the complexity of the multiphysics phenomena that take place in the RS generation of welded structures, the estimation of their magnitude and distribution is not straight forward [14, 15]. In addition, nowadays accurate experimental measurement of RS presents some limitations as experimental methods are not fully reliable and imply huge time and economic cost [9, 16, 17]. Consequently, most of the currently used welding dimensioning approaches do not consider RS. Therefore, current welded designs are in general conservative, leading to oversized structures. This fact is especially relevant in big structures since it generates high material, manufacturing and product transportation costs. As a simplified manner to take into account RS, some authors consider the yield stress value as RS magnitude [18–20].

However, nowadays the RS distribution and magnitude can be estimated by means of numerical simulation [14, 21]. As already explained, the RS generation in welded plates is very dependent on the thermal pattern history along the whole component as well as the materials thermomechanical properties. Thus, the procedure used to model the moving heat source during the welding process simulation is determinant in the accuracy of the predicted RS pattern [22].

Different approaches to model the heat source energy can be found in the literature. In the early 1940s, Rosenthal presented an analytic model to consider heat source at a quasi-steady regime, concentrated in a moving point [23]. Although the model could be applied in simple geometries, it was not suitable to be used at plates over certain thickness [2, 6]. At the end of

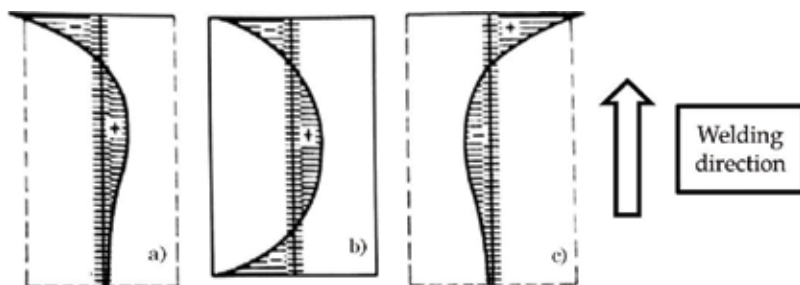


Figure 2. Transversal RS distribution near the weld toe of a butt weld: (a) under high deposition speed in a big plate, (b) high deposition speed in a short plate and (c) low deposition speed in a big plate [13].

1960s, Pavelic et al. [24] proposed a procedure to model as a moving circular heat input area with a Gaussian distribution of the heat intensity. The model considers that all the heat supplies occur through the surface, which also limits its use over certain plate thickness.

In 1984, Goldak et al. presented an alternative heat source model, known as the double ellipsoidal method or Goldak's method, which is one of the most extended methods nowadays [25–30]. This method considers a double ellipsoidal power density distribution (**Figure 3**). This method presents good accuracy even though it requires experimental run trials to measure the weld pool. These measurements should be conducted during or after finishing the welding process, which limits its use as a predictive tool [31]. In addition, the measurement of the weld pool for certain configurations such as T-joints or L-joints is geometrically limited. In 1997, Wahab et al. [32] developed some analytical equations based on experimental measurements to predict the weld pool depending on the applied voltage, current intensity, welding speed and $\text{CO}_2\%$. Nevertheless, even these analytical equations enable the use of Goldak's method as a predictive tool, it still presents a lack of precision with reported stress deviations higher than 100 MPa [10].

In 1998, Brickstad et al. [7] proposed a heat source modelling technique where the current and voltage applied in the welding process were used as input parameters. The technique was implemented to simulate a case study of a multipass butt weld of stainless steel pipes by means of a two-dimensional axisymmetric numeric model. The validity of the model was not evaluated against experimental data. In 2007, Barsoum et al. [33] implemented the same technique also in a three-dimensional model to simulate a multipass welding of a tubular joint. The results obtained in the experimental validation showed that even the temperature prediction for a single pass butt weld was accurate, the model presents a lack of precision for multipass cases. In addition, in this method the calculated temperature histories are set into agreement with experimental data measured by thermocouples. If there is no experimental data available, the welding parameters are adjusted to achieve a reasonable molten zone size and distance to the HAZ from the fusion zone boundary [30].

Finally, from 2007 to 2009, Hu et al. [34–36] presented several works where a 3D mathematical model was implemented to represent the physics of the plasma arc and the metal transfer in

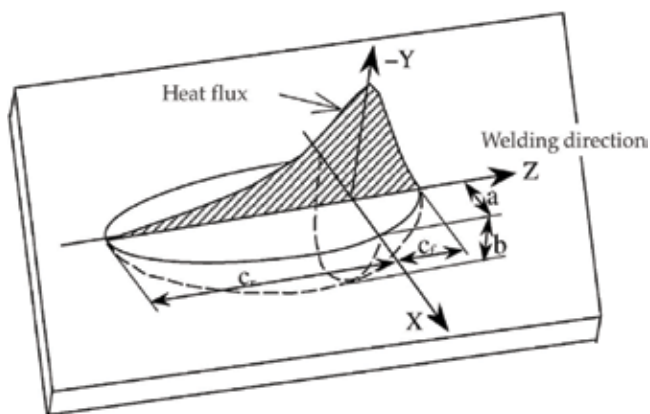


Figure 3. Schematic of the heat source modelization with Goldak's double-ellipsoidal method [25].

order to solve accuracy limitations. This method, besides the computational cost, requires the definition of many parameters such as the arc plasma viscosity, the arc plasma temperature, the surface tension coefficient, etc. The complexity to determine those parameters together with the high computational cost limits the use of this technique.

In general, the presented methods are sometimes imprecise or require defining experimentally many parameters, which limit their use during the design process. As an alternative, in this chapter an analytic procedure to calculate the welding process key parameters is presented. The procedure is based on the welding physics for spray transfer, and the key parameters are analytically estimated. Thus, the procedure feeds the FEM numerical model without the need to conduct experimental process measurements, which enables to be used as a predictive tool. The proposed procedure has been experimentally validated. First, the heat source model has been verified, and then the temperature pattern and the residual stress pattern predicted by the FEM model have been compared against experimental measurements. The main contribution of the presented procedure is that it provides an agreement between the accuracy of the model in the residual stress estimation, the computational cost and the model definition effort. In addition, the new procedure does not require any preliminary experimental welding test data, which make it suitable to be used in the design process.

Finally, the proposed procedure is extended to a T-joint configuration with 70% penetration in a thickness range from 20 to 60 mm to determine the influence of the thickness and number of passes in the RS pattern.

2. New methodology to predict RS

The proposed methodology to predict RS consists of two steps. First, the process key parameters, which are the heat source and the welding speed, are defined. For that purpose, an analytic procedure to determine the heat source and welding speed that ensure proper spray transfer welding is developed. Then, an uncoupled thermomechanical FEM model is used to simulate the welding process. This numerical model is fed from the previously defined process key parameters.

2.1. Determination of process key parameters

The multipass spray transfer welding numerical model requires the determination of the heat source energy and the welding speed as input data. Both parameters are estimated based on the welding torch configuration and the cross section to weld.

Figure 4 shows the detail of the configuration of the welding torch, where L_{arc} is the arc length, L_{CTW} is the contact to work distance and L_{SO} is the wire extension or electrical stick-out length.

2.1.1. Heat source energy

The heat source energy is the thermal energy provided to the weld bead along the welding process. This parameter is calculated considering the efficiency in the transformation of the

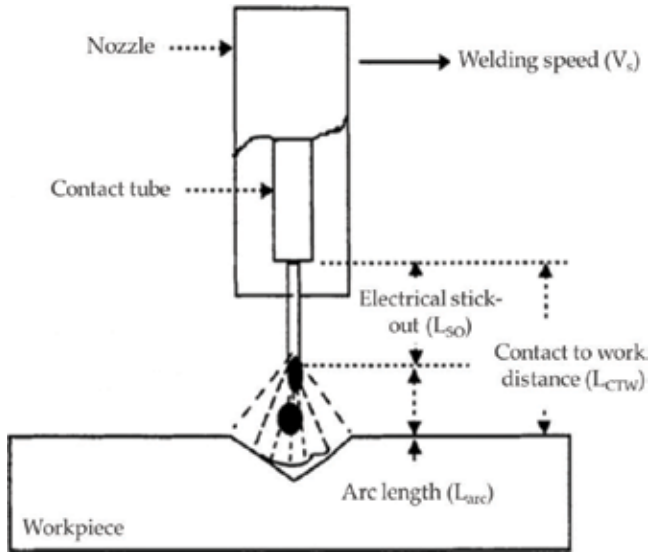


Figure 4. Schematic of the welding torch configuration (adapted from [1]).

consumed electric power into heat power. This energy loss is caused by the wire resistance, heat losses to the surrounding, the energy consumed in the gas or flux heating, etc. Thus, efficiency can vary between 0.66 and 0.85 depending on the used facility [1]. Therefore, the supplied heat power can be determined with Eq. (1):

$$P_{TH} = \eta \cdot I \cdot V_{Tot} \tag{1}$$

where P_{TH} is the supplied thermal power, η is the heat transformation efficiency, I is the current intensity and V_{Tot} is the total voltage.

In order to ensure proper spray transfer, the transition welding intensity between globular and spray transfer modes is determined first. This parameter is dependent on the used shielding gas and filler wire diameter. Thus, using current intensity values higher than the transition current intensity limit value provides proper spray transfer. Figure 5 represents the correlations proposed by Norrish [37] to determine the globular-to-spray mode transition current depending on the shielding gas for a wire diameter range between 0.8 and 1.6 mm.

The total voltage drop V_{Tot} is approximately the addition of the voltage drop in the electric stick-out length V_{so} and the voltage drop across the arc V_{arc} (2) [1].

$$V_{Tot} = V_{arc} + V_{so} \tag{2}$$

The arc voltage drop can be obtained with Eq. (3):

$$V_{arc} = I \cdot R_{arc} + a_0 + a_1 \cdot L_{arc} \tag{3}$$

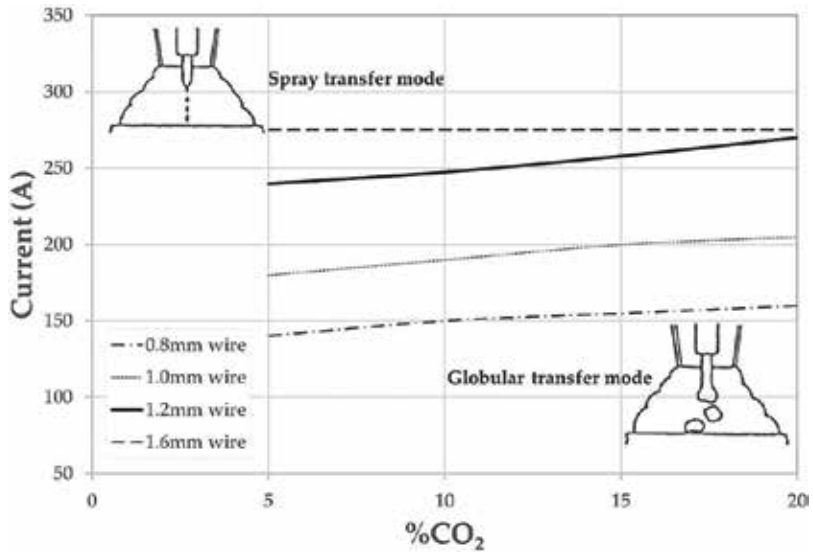


Figure 5. Globular mode to spray mode transition current depending on the use of shielding gas for wire diameter range between 0.8 and 1.6 mm (adapted from [37]).

where R_{arc} is the arc electric resistance, a_0 is the anode/cathode voltage drop and a_1 is the arc potential gradient. The minimum L_{arc} to ensure spray transfer has to be higher than 4.5 mm according to Lesnewich [48].

The voltage drop across the electrode is calculated with Eq. (4):

$$V_{so} = \rho_s \frac{L_{so}}{A_{so}} I \quad (4)$$

where ρ_s is the resistivity of the stick-out material and A_{so} is the cross-section area of the wire.

The stick-out length L_{so} (Figure 4) is determined with Eq. (5):

$$L_{so} = L_{CTW} - L_{arc} \quad (5)$$

2.1.2. Welding speed

The welding speed is the velocity the welding torch advances along the welding bead. It is assumed that GMAW process fulfils the mass conservation law. Thus, wire feed speed and welding speed can be determined by Eq. (6):

$$A_{so} \cdot v_w = A_s \cdot v_s \rightarrow v_s = \frac{A_{so} \cdot v_w}{A_s} \quad (6)$$

where v_w is the wire feed speed, A_s is the weld pass cross section and v_s is the welding speed.

There are two approaches to model the wire feed rate for constant voltage welding used in GMAW, as suggested by Palani et al. (2007) [39]. The first approach consists in fitting the

equation relating welding current and wire feed rate with experimental data. The second approach consists in using the results of the experiments to determine the constants of proportionality for the arc heating and the electrical resistance heating.

In the methodology presented in this chapter, the second approach is used. Thus, the wire feed speed is calculated with Eq. (7) [37]:

$$v_W = \alpha \cdot I + \frac{\beta \cdot L_{s0} \cdot I^2}{A_{s0}} \quad (7)$$

where α and β are constants dependent on the used wire properties.

Moreover, considering different values of the constants (α and β) from several studies for solid plain carbon steel wire analysed from literature (Norrish 1992 [37], Murray 2002 [40], Modenesi 2007 [41], Palani 2006 [42], Palani 2007 [39]), it is observed that their difference is negligible (**Figure 6**). Therefore, in the present work, it is decided to consider the values defined in [37], $\alpha \approx 0.3 \text{ mmA}^{-1} \text{ s}^{-1}$ and $\beta \approx 5 \cdot 10^{-5} \text{ A}^{-2} \text{ s}^{-1}$ for a 1.2 mm plain carbon steel wire.

2.2. Uncoupled thermomechanical FEM modelling procedure

Welding is a thermometallurgical process where the thermal field directly affects in the mechanical domain response, but the effect of the mechanical field on the thermal domain can be considered negligible as dimensional changes in the welding process are not representative and generated deformation energy is insignificant compared to the thermal energy from the welding arc [43]. Thus, the welding process can be modelled with an uncoupled

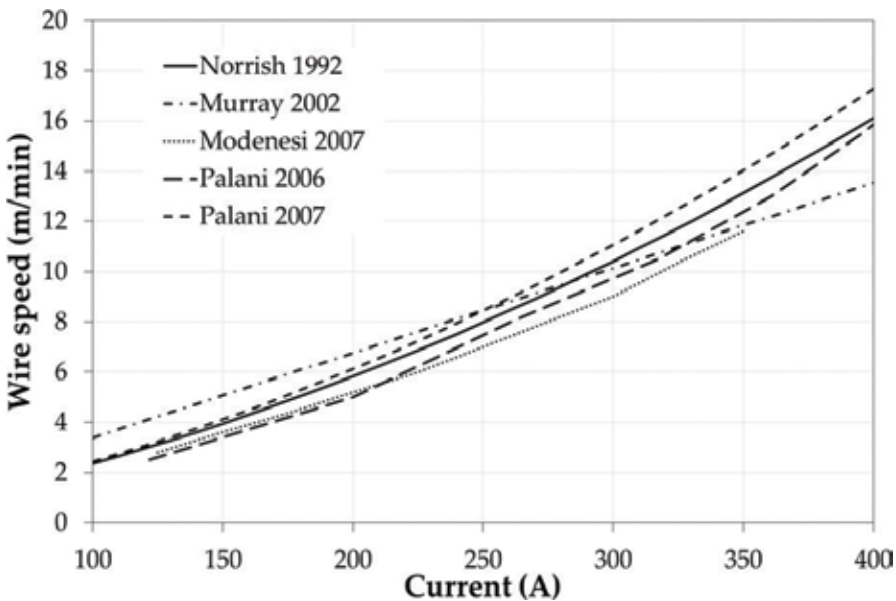


Figure 6. Comparison of different approaches to determine wire speed based on welding intensity for carbon steel filler (adapted from [37, 39–42]).

thermomechanical approach where the thermal domain is solved first. Then, the mechanical field is solved fed by the previously calculated thermal pattern history. Consequently, computational cost can be significantly reduced. Both equation systems are solved by using the implicit direct integration method.

Even though both models are solved separately, they share same geometric model where just the element type and restrictions differ.

2.2.1. Geometric model

The geometric model has to include the geometry of each welding pass based on the calculated cross section for each pass. According to Teng et al. [44], the flank angle does not have significant effect in the residual stress value. For this reason, considering the real geometry of the plates to weld, a flank angle of 30° has been selected to define the bead radius (see **Figure 7**). The arcs for the bead in the rest of the passes are defined concentric with respect to the last pass by keeping the value of the initially calculated cross section for each pass.

The model is meshed by using full integration continuum hexahedral elements (recommended) where the proper formulation is selected, respectively, to solve the thermal domain and the mechanical domain (**Figure 8a**). The addition of filler material through each pass is modelled by using the kill/rebirth method [13, 22, 26] (**Figure 8b and c**). In this method, all the weld bead elements are initially inactive and, consequently, eliminated from the equation system. Then, elements are activated in function of the welding speed (v), simulating the welding torch pass. In order to ensure sufficient resolution in the transient temperature evolution, a temporal discretization of one second is specified. Symmetry is not considered as an asymmetric clamping condition where just one plate end is fixed to avoid during the validation the influence of the boundary restrictions in the predicted RS pattern (in accordance with the used experimental set-up).

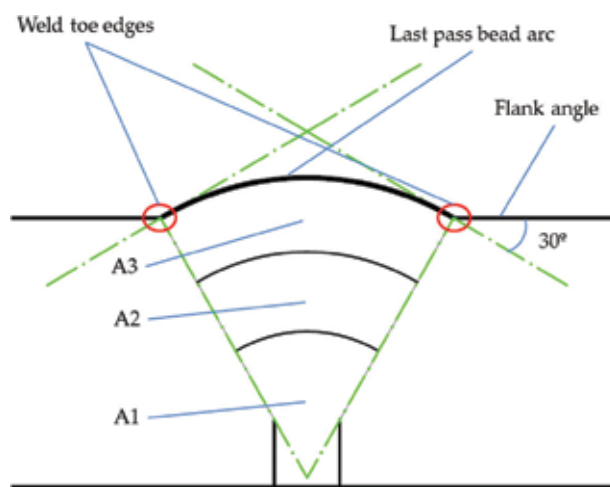


Figure 7. Schematic of the procedure to calculate the weld bead geometry for each pass for a three-pass weld case.

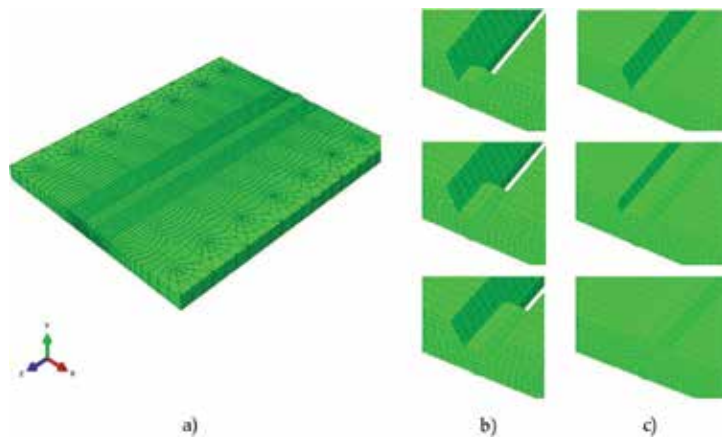


Figure 8. (a) Example of a full geometric model of a multipass butt weld, (b) principle of the addition the weld bead and (c) multipass welding modelling of a three-pass weld case.

2.2.2. Material

Temperature-dependent thermal and thermomechanical properties of both plate material and filler material have to be defined to feed the thermal model and mechanical model, respectively:

- **Modelization of the thermal field:** Density, latent heat, thermal conductivity as well as specific heat are required.
- **Modelization of mechanical field:** Density, Young modulus, Poisson ration, thermal expansion coefficient as well flow stress curves are required.

Regarding phase transformation effects, the aim of the present modelling methodology is to reach to an agreement between the model simplicity and accuracy level. Therefore, even effect of phase transformation in the temperature-dependent properties such as density, thermal expansion or specific heat is considered, the mechanism of phase transformation is not included in the model. Some studies in the literature as the work presented by Payares-Asprino et al. in 2008 [45] have shown that this phase transformation could be significant for low temperature transformation (LTT) filler materials. However, in the present study, a conventional filler material is used, where the expansion that material suffers by martensitic transformation is relatively small and occurs at relatively high transformation temperature range. Consequently, its effect in the generated residual stresses and distortions is not significant [46].

2.2.3. Loads and boundary conditions

- **Modelization of the thermal field:** Based on the previously exposed analytic procedure, heat source is implemented as uniform body heat flux over the elements activated at the rebirth speed corresponding to the welding speed. Natural convection of the free surfaces as well as radiation should be considered.

- **Modelization of mechanical field:** Clamping restraints have to be considered as boundary conditions. In addition, temperature pattern is fed from the previously calculated thermal model considering the rebirth speed corresponding to the welding speed. Once the welding process and cooling down process are completed, clamping restraints are deactivated to obtain final RS pattern.

3. Methodology implementation and experimental validation

The proposed procedure is implemented and validated for a case study of three-pass spray transfer butt weld of 10 mm thick and 200 mm length of two S275JR steel plates (see **Figure 9**). The used filler material is a 1.2 mm wire diameter PRAXAIR M-86 according to the AWS/ASME SFA 5.18 ER70S-6 standard. Stargon 82, with 8% of CO₂, is used as shielding gas.

3.1. Numerical procedure

The heat transfer model as well as the mechanical model used for the simulation of the welding process of the selected case study is implemented in the simulation software ABAQUS™.

3.1.1. Geometric model

A critical activation length per second of 6.12 mm is calculated to ensure temporal discretisation of 1 s for the third pass, which is conducted with the lower welding speed. Consequently, a 5 mm length discretization size, which ensures a temporal discretization <1 s for the three passes, is selected for the presented work. Furthermore, it allows fitting exactly with 40 discretization volumes the 200 mm length of each pass.

3.1.2. Material

Table 1 shows the standard mechanical properties of S275JR structural steel used for the welded plated and the PRAXAIR M-86 filler material at room temperature. As it can be observed, both materials show similar ultimate strain and ultimate strength, but the yield stress of the filler material is 45% higher.

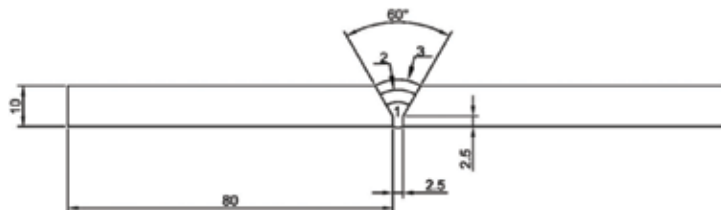


Figure 9. Welding configuration of the analysed case study.

	σ_y (MPa)	σ_u (MPa)	A (%)	E (GPa)
S275JR	275	430–580	23	190–210
Filler M-86	>400	>480	>22	200

Table 1. Standard mechanical properties of S275JR structural steel [47] and PRAXAIR M-86 filler material [48, 49].

Temperature-dependent flow stress curves at a quasi-static strain rate for the filler material are estimated based on S275JR data and considering a 45% higher temperature-dependent yield stress value. The rest of thermomechanical properties as well as thermal properties are considered the same as the base material. This simplification is considered acceptable according to the next statements:

- Considering same thermal properties as will have minor influence in the estimated temperature distribution and thermal expansion as both steels present similar, conductivity, specific heat, latent heat and thermal expansion.
- Same temperature-dependent density and elastic modulus can be considered for both the base material and filler material, as low variations in the content of alloying elements of structural steels have insignificant influence in these parameters [49].
- The temperature-dependent yield stress of the filler material is assumed to be 45% higher than the base material. As the plastic deformation level found in the welding process is low, near the yield stress values, considering the same temperature-dependent tangent modulus will not have significant effect in the predicted RS pattern.
- The cross section of the weld bead is small in comparison with both plates' cross section. For this reason, considering same thermal expansion value as for the base material will generate an insignificant deviation in comparison with the total thermal expansion. Consequently, it is considered that possible error generated from the previous assumptions in the computed transversal residual stress will be negligible.

3.1.3. Thermal properties

Figure 10a shows the utilised temperature-dependent density, thermal conductivity and specific heat data for both filler and plate materials. **Table 2** shows the considered latent heat and solidus-liquidus transition temperature.

3.1.4. Thermomechanical properties

Figure 10b–d shows the temperature-dependent mechanical properties for both the base material and filler material.

3.2. Loads and boundary conditions

3.2.1. Heat transfer model

Heat source and welding speed for the specified case study are obtained with the new methodology exposed in Section 2. First, in order to determine the efficiency of the used welding

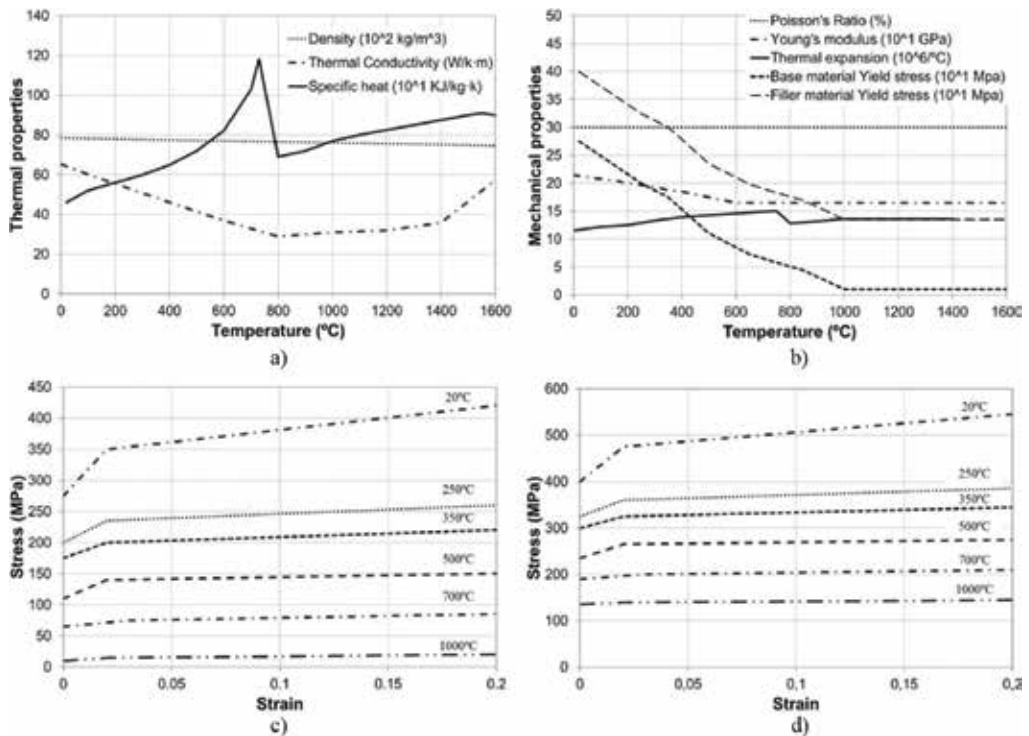


Figure 10. Temperature-dependant material properties. (a) Specific heat taken from [50], thermal conductivity taken from [22, 51] and density taken from [46]; (b) Young's modulus and thermal expansion taken from [52] and yield stress taken from [53, 54]; (c) plastic properties for the base material [22]; and (d) estimated plastic properties for the wire material.

Latent heat (kJ/kg)	Solidus temperature (°C)	Liquidus temperature (°C)
247	1500	1550

Table 2. Latent heat of fusion [36].

facility, simulations for an efficiency range between 0.6 and 1 are conducted. **Table 3** shows the heat source power for each pass calculated with the following parameters:

- **Transition welding intensity for spray transfer:** The use of a 1.2 mm wire diameter and Stargon 82 as shielding gas, which contains 8% CO₂ [55], determines a minimum welding intensity of 245A to ensure proper spray transfer model. Therefore, for the present case study, an intensity value of 275 A, 12% higher than the transition limit, is used.
- **Wire properties:** The resistivity value of the used wire is $R_{arc} = 0.0237 \Omega$ [3]. The parameters a_0 and a_1 are set as 6.3 V and 1.55 V/mm respectively based on [4].
- **Welding torch configuration:** A 9 mm L_{arc} ($> L_{arc_min}$ of 4.5 mm [38]) and a 30 mm L_{CTW} are defined. For carbon steels [1], a $0.2821 \frac{\Omega}{m}$ resistivity of the stick-out material is set.

Efficiency (%)	Power (W)		
	First pass	Second pass	Third pass
1	7755	7755	7755
0.9	6980	6980	6980
0.85	6592	6592	6592
0.8	6204	6204	6204
0.75	5816	5816	5816
0.7	5429	5429	5429
0.6	4653	4653	4653

Table 3. Values of the heat power for different efficiencies.

Welding speed to be implemented as element rebirth rate has been calculated for each pass by using the parabolic model constants $\alpha \approx 0.3 \text{ mmA}^{-1} \text{ s}^{-1}$ and $\beta \approx 5 \cdot 10^{-5} \text{ A}^{-2} \text{ s}^{-1}$ for a 1.2 mm plain carbon steel wire [37]. Thus, the calculated welding speeds for each pass of the case study in the present work are 545.33, 482.53 and 367.79 mm/min.

Finally, a natural convection boundary condition has been assumed in all surfaces exposed to air of both plates and the rebirthed weld bead elements.

3.2.2. Uncoupled thermomechanical model

Temperature pattern at every iteration is fed from the previously run heat transfer simulation results. As a boundary condition, one of the plate end surfaces is assumed to be fully constrained.

3.3. Experimental procedure

Figure 11 shows the CNC milling machined adapted with a Praxair Phoenix 421 welding machine in order to perform the welding process automatically. This enables to control all the

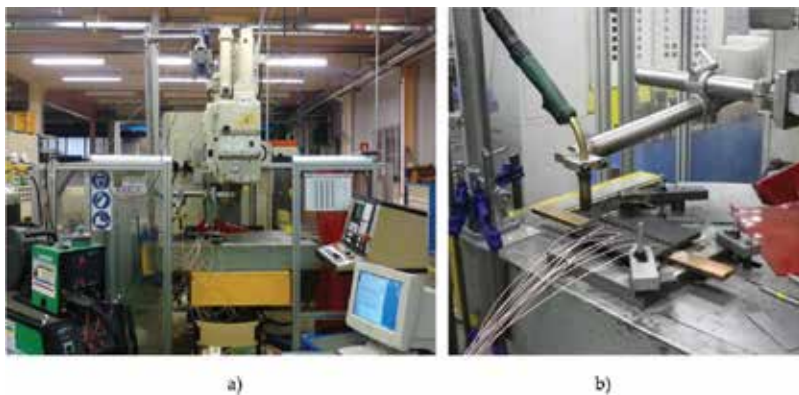


Figure 11. a) Set-up to automatically perform the welding process and b) Detail of the welding configuration.

process parameters such as the arc voltage, the arc length, the contact to workpiece length, the wire feed speed and the welding speed along the whole process. In addition, current intensity and voltage during the whole process are monitored by means of a TPS2024B Tektronix oscilloscope, a PR HAMEG HZ115 voltmeter and a LEM PR 200 ammeter.

In order to conduct the validation of the proposed modelling methodology, temperature pattern evolution during the welding process and the RS pattern of the welded samples are also measured.

3.4. Welding procedure

S275JR plates of 10 mm thick and 200 mm length are butt welded in three passes (**Figure 9**) with a 1.2 mm diameter PRAXAIR M-86 filler material. Stargon 82, with 8% of CO₂ [54], is used as shielding gas.

Welding process parameters for each pass are previously determined with the proposed analytical procedure for spray transfer mode (**Table 4**).

3.4.1. Temperature pattern measurement

Temperature pattern history is acquired along the whole process to determine the welding facility's efficiency and to validate the numerically obtained temperature pattern. For this purpose two methods are used in parallel: (i) 10 N-type thermocouples (up to 1200°C) are positions parallel and perpendicular to the weld bead (**Figure 12a**) and (ii) a Titanium DC01 9 U-E thermographic camera to record the surface temperature pattern evolution.

To ensure proper temperature pattern measurement with the thermographic camera, plates are painted with a black colour high temperature-resistant paint in which temperature-dependent emissivity is already determined [56]. However, for better accuracy, the temperature acquisition data of the thermocouples is used to calibrate the acquired temperature pattern.

3.4.2. Residual stress measurement

In order to validate the numerically obtained RS pattern and, consequently, the proposed modelling methodology, RS measurements are conducted by using the hole-drilling method.

To conduct the measurements, Vishay EA-06-062RE-120 rosette-type gauges are placed parallel to the welding bead, at a 52.5 mm distance from the weld toe at both sides of the weld bead as shown in **Figure 12b**. Then, hole-drilling tests are carried out in a CNC milling machine according to ASTM E837 standard.

Pass	V (V)	I (A)	V _w (m/min)	P (W)	L _{arc} (mm)	L _{ctw} (mm)	V _s (mm/min)
1	28.2	275	9.2	7755	9	30	545.33
2	28.2	275	9.2	7755	9	30	482.83
3	28.2	275	9.2	7755	9	30	367.796

Table 4. Welding process parameters.

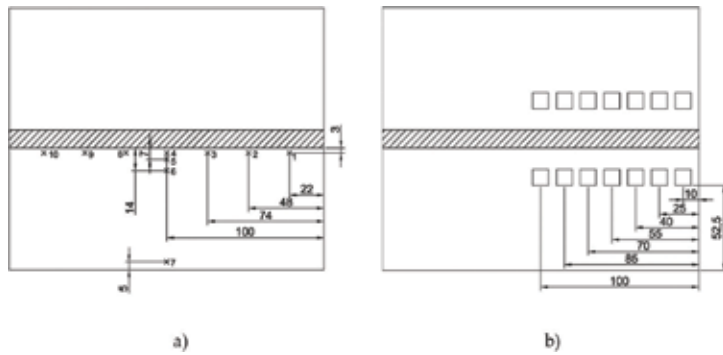


Figure 12. Position of the thermocouples (a) and (b) position of the hole-drilling gauges in the butt weld.

3.5. Results and discussion

In this section, theoretical results and experimental results are compared in order to validate the proposed modelling methodology. For that purpose, first the temperature pattern prediction, which determines the material’s thermal expansion, is compared. Then, RS pattern generated by the thermal expansion is validated.

3.6. Temperature pattern validation

Figure 13 shows the comparison of the experimental temperature evolution along the three passes and the theoretically estimated values for an efficiency value of 1. It can be observed that both curves present same process dynamic, where the temperature peaks when the welding torch is near to the reference thermocouple can be clearly identified, followed by a progressive cooling down related to the heat evacuation. In addition, it can be observed that as the cross section of each pass increases, the heat supply for each pass raises and, consequently,

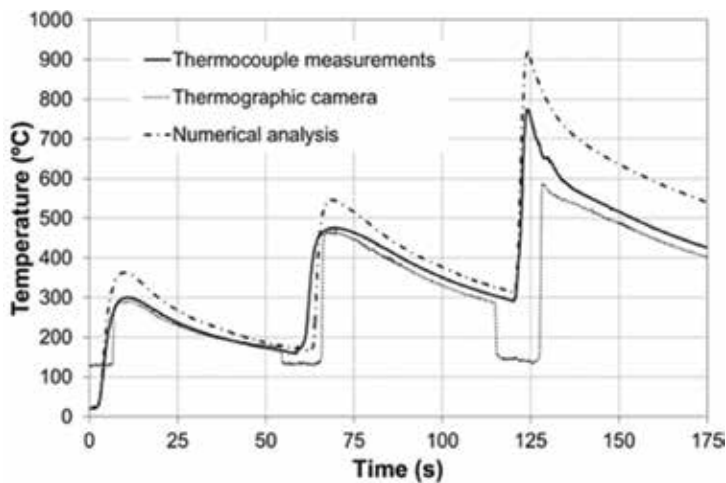


Figure 13. Calculated and measured thermal cycles for thermocouple 1 with an efficiency factor of 1.

the peak temperature value for each pass also increases. From a quantitative point of view, as expected, a theoretical efficiency value of 1 provides higher temperature values than experimentally acquired curves as no power losses are considered.

For this reason, the efficiency of the used welding facility is determined comparing the temperature deviation of all thermocouples at each pass for the simulations conducted in an efficiency range between 0.6 and 1 (**Table 5**). The results show that the highest accuracy is obtained for an efficiency value of 0.8 with an average deviation of 9.16%. Therefore, it is assumed that the efficiency of the facility is 0.8, which is in accordance with the efficiency reference values found in the literature (0.66–0.85) [1].

Figure 14 shows the comparison of the theoretical and experimental temperature evolution for thermocouple 1 for an efficiency of 0.8. An uncertainty attributed to a ± 0.5 mm thermocouple positioning error has been considered in the temperature validation. It can be observed that the temperature evolution present presents a positive quantitative correspondence along the three passes.

In addition, **Figure 15** shows the comparison between the experimental temperature pattern acquired with the thermographic camera and the numerically predicted pattern at the end of each pass for an efficiency value of 0.8. Both temperature patterns show good correspondence in the shape of temperature contours from the high temperature zone over 700°C down to the lower temperature areas at 300°C (limit of the filter use in the thermographic camera).

Considering the low deviation (9.16%) in the temperature evolution prediction together with the positive correspondence found in the temperature pattern contours at each pass, it is concluded that the numerical procedure to predict temperature pattern evolution of multipass spray transfer welding is valid.

3.7. Residual stress validation

Once the performance of the proposed methodology in the thermal field prediction is validated, the RS field is verified to conclude with the model validation.

Efficiency	Error (%)			
	First pass	Second pass	Third pass	Average
1	21.94	20.02	21.77	21.24
0.9	12.8	10.46	16.7	13.33
0.85	8.47	5.82	16.68	10.32
0.8	3.9	5.31	18.26	9.16
0.75	3.45	6.57	19.82	9.95
0.7	6.61	9.97	21.44	12.67
0.6	17.44	20.24	31.17	22.95

Table 5. Calculated error for the peak temperatures at each pass for an efficiency range of 0.6–1.

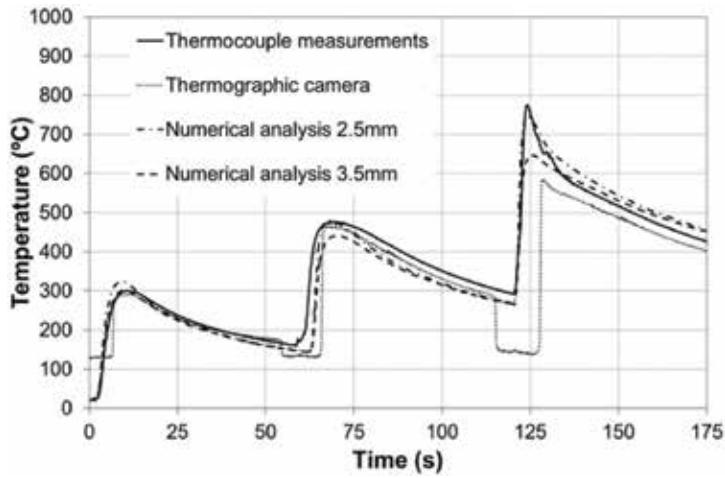


Figure 14. Comparative of experimental versus FEM thermal results for a butt weld with an efficiency factor of 0.8.

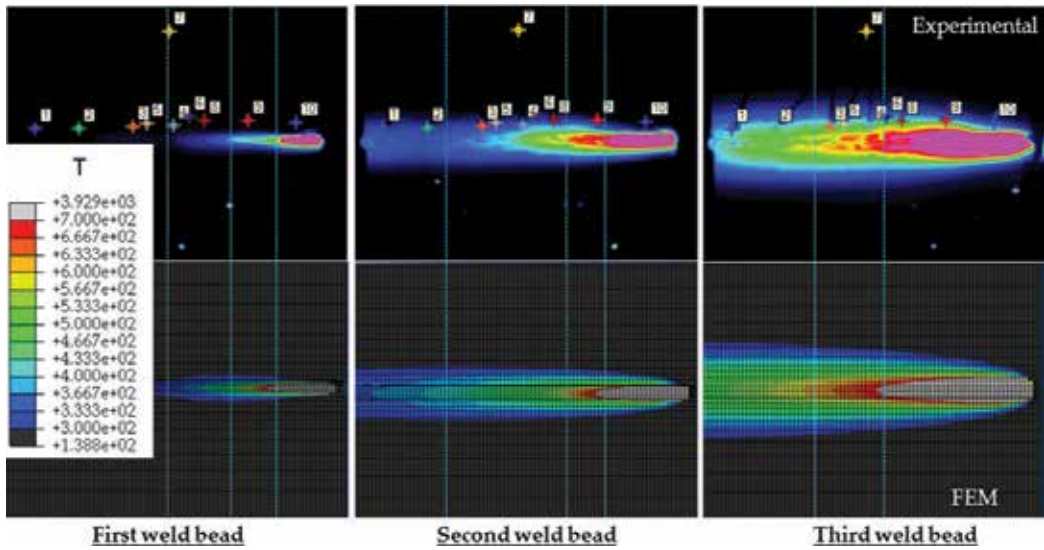


Figure 15. Comparative of experimental versus FEM thermal pattern for a butt weld with an efficiency factor of 0.8 (the points in the upper images are the position of the thermocouples).

Figure 16 shows transverse residual stresses pattern obtained with the FEM uncoupled thermo-mechanical simulation. A high stress concentration in the clamping area where 6 degrees of freedom are fixed is observed (in accordance with the experimental set-up). However, the stress concentration located in the clamping is far enough from the area of interest, and they do not have any effect in the residual stress validation process. Analysing the area of interest, it is observed that even the stress concentration in the clamping area does not affect the area of interest near the weld bead, the asymmetry in the boundary restriction generates a mild asymmetric

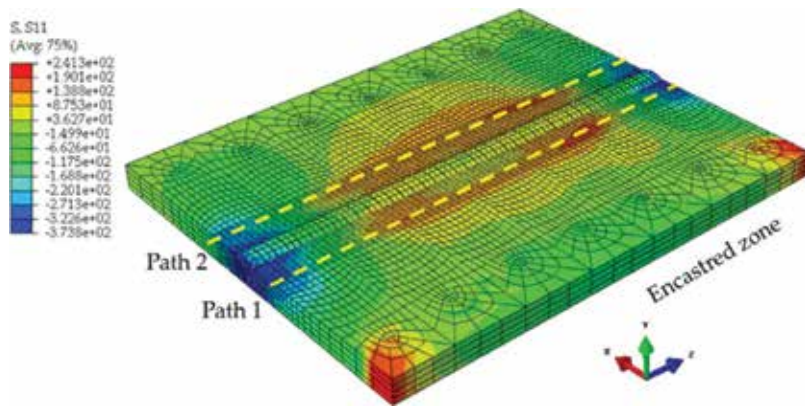


Figure 16. Transversal residual stresses pattern for a butt weld.

stress pattern at both sides of the weld seam. Consequently, stress paths at both sides, path 1 and path 2 located in the maximum stress are at each side, are considered for validation purpose.

Figure 17 shows hole-drilling measurements of the transversal residual stress along half of the length (0–100 mm) for both, path 1 and path 2. The results show three differentiated zones: (i) compression zone (0–30 mm), (ii) transition zone (30–60 mm) and (iii) tensile zone (60–100 mm). Additional measurements are conducted in the full length (at 160 mm and 175 mm) to ensure that the RS path shows quasi-symmetric behaviour.

High scatter among the measurement repetitions, inherent to the measuring technique, is observed, which is in accordance with stress deviations up to ± 50 MPa reported by some authors [57]. Therefore, average hole-drilling results at each position are considered for both paths to perform the RS validation. **Figure 18a** and **b** shows the comparison between the average hole-drilling results with their standard deviation and simulation results for path 1

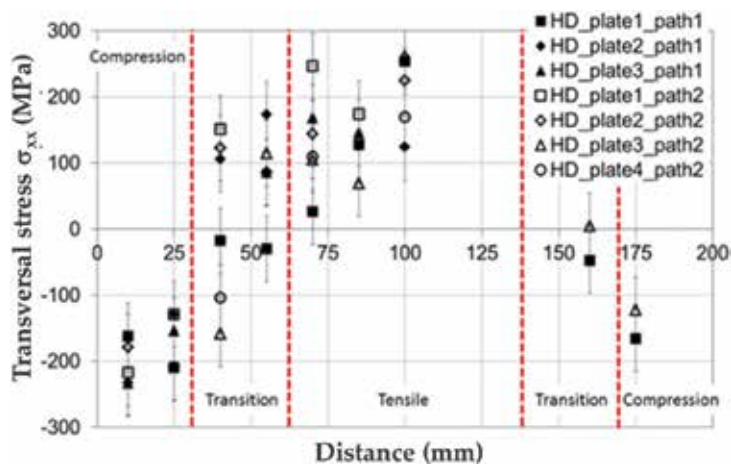


Figure 17. Results of hole-drilling measurements for different plates and for both paths.

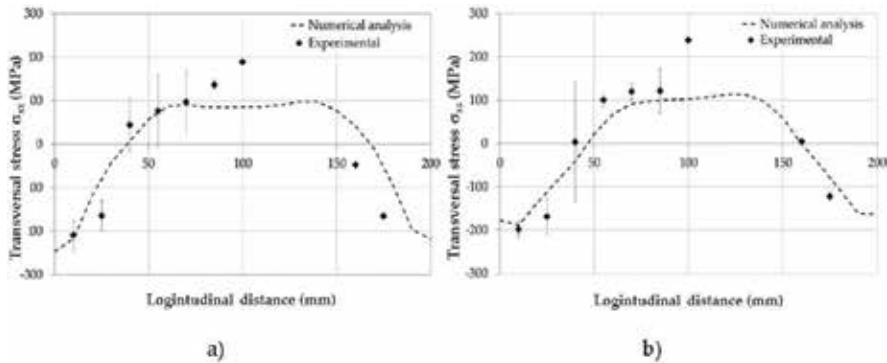


Figure 18. Comparison of the FEM and experimental results for the results of hole.

and path 2, respectively. A positive correspondence is observed between the averaged measurements and the numerical results for both paths where the three zones, compression zone, transition zone and tensile zone, show similar trends. Considering both paths, an average error of 34 MPa, 35 MPa and 57 MPa for each zone, respectively, is calculated with an average total error of 42 MPa. As observed, numerically predicted residual stress values are mostly inside the measurement scatter band (± 50 MPa [57]). Thus, it can be concluded that, considering the inherent error of the RS measuring technique, the proposed methodology to predict RS pattern can be considered valid with an average error of 42 MPa.

4. Theoretical analysis of RS pattern on thick T-joint samples

T-joint welding configurations are one of the most widely used in a wide range of structural applications. Particularly, when building large structures, T-joint of thick plates requires high amount of weld passes, and consequently, the RS pattern varies considerably depending on the plate thickness and the number passes, hence affecting to mechanical performance such as fatigue endurance.

Nowadays, most approaches to dimension-welded structures do not consider RS real value due to the difficulty of estimating them; hence, they tend to be conservative. However, recent works [gure erreferentziak] have demonstrated that considering RS, the error for example in fatigue life prediction can be reduced down to 15%.

In this section, the RS pattern of multipass T-joints at 70% penetration of S275JR plates for a thickness range from 20 to 60 mm is evaluated (see **Figure 19**). Same filler material, 1.2 mm diameter PRAXAIR M-86 filler wire, according to the AWS/ASME SFA 5.18 ER70S-6 standard, and a quasi-constant weld pass section are considered for all cases. **Table 6** shows the studied case configuration data where dimensions (wide and length) have been previously specified to avoid the influence of the edge boundary effects in the RS pattern.

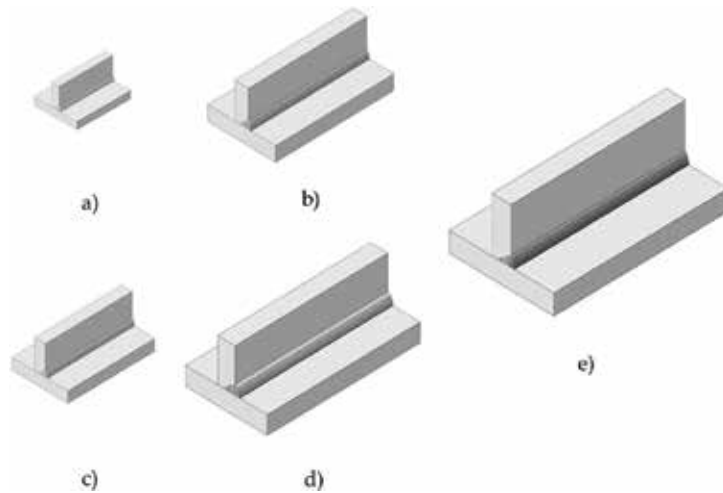


Figure 19. (a) 20 mm-, (b) 30 mm-, (c) 40 mm-, (d) 50 mm- and (e) 60 mm-thick T-joint case studies.

4.1. Numerical procedure

In this section, the modelling procedure presented in Section 2 and validated in Section 3 is used. As in Section 3, the heat transfer model as well as the mechanical model used for the simulation of the welding process of the selected case studies is implemented in the simulation software ABAQUS™.

4.2. Geometric model

In this Section, 10 mm length discretization size is used, which ensures a temporal discretization lower than 2 s in all the passes. **Figure 20** shows the numerical model of a 40-mm thick case study with 14 passes (T-joint_40).

Case study	Dimensions			Number of passes
	Thickness (mm)	Wide (mm)	Length (mm)	
T-joint_20	20	120	150	4
T-joint_30	30	160	250	8
T-joint_40	40	200	350	14
T-joint_50	50	240	450	22
T-joint_60	60	280	550	31

Table 6. Case studies configuration data. Numerical procedure.

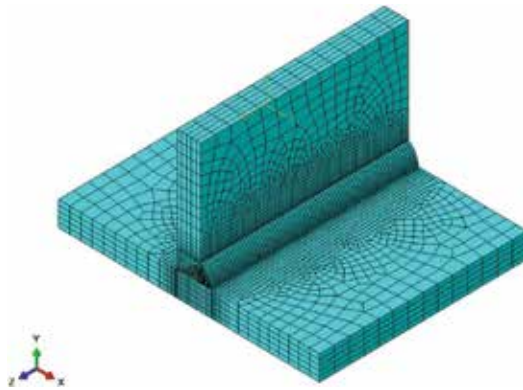


Figure 20. Numerical model of case study T-joint_40.

Case study	Pass cross section (mm ²)	Process parameters		FEM input parameters		
		Welding power (W)	Welding speed (mm/min)	Body heat flux (W/mm ²)	Discret. length (mm)	Kill-rebirth rate (s ⁻¹)
T-joint_20	26.78	7201	388	23.37	10	0.65
T-joint_30	29.20	7310	356	21.82	10	0.59
T-joint_40	29.23	7311	356	21.82	10	0.59
T-joint_50	30.63	7471	345	21.82	10	0.58
T-joint_60	30.15	7567	345	21.93	10	0.58

Table 7. Theoretical welding process parameters and FEM input parameters.

4.3. Material

In this section, same material properties that are used in Section 3 are considered for S275JR plates and the 1.2 mm diameter PRAXAIR M-86 filler wire.

4.4. Loads and boundary conditions

The main input parameters to be implemented in the FEM model, i.e. heat source power and welding speed, have been defined according to the analytical procedure proposed in Section 2. Thus, welding speed to be implemented as element rebirth rate has been calculated for each pass by using the parabolic model constants $\alpha \approx 0.3 \text{ mmA}^{-1} \text{ s}^{-1}$ and $\beta \approx 5 \cdot 10^{-5} \text{ A}^{-2} \text{ s}^{-1}$ for a 1.2 mm plain carbon steel wire as previously specified. Table 7 shows the calculated process parameters and input parameters for the FEM model.

Finally, a natural convection boundary condition has been assumed in all surfaces exposed to air (in both plates and rebirthed weld bead elements).

4.5. Results and discussion

Figure 21 shows the RS pattern in the normal direction to the weld seam for the case of 40-mm thick T-joint as example. It can be observed that maximum stress is generated next to the weld seam.

Figure 22 shows the evolution of maximum equivalent uniaxial RS in the critical plane, which is especially interesting to conduct fatigue assessment [58], for different welded plate thickness. Two different trends clearly are observed:

- For low thickness, maximum uniaxial RS value increases from 85% of the yield stress (235 MPa) for 20 mm thickness plates up to 95% of the yield stress (261 MPa) for 40 mm thickness plates.
- In contrast, for thickness higher than 40 mm, it is observed that RS value decreases down to 66% of yield stress (182 MPa) for 60-mm thick plates.

As temperature gradients are the main responsible for RS generation, these opposite trends are attributed to the fact that when plate thickness is increased, two different phenomena occur: (i) the increase of provided total heat (directly related with the number of passes) and (ii) the increase of the heat absorption capacitance of the welded plates (directly related to the increase of the total volume).

The total supplied heat energy E_{in} can be described as de product of the heat power supplied Q_{in} and the welding time t (8):

$$E_{in} = Q_{in} t \quad (8)$$

The welding time t is dependent on the total welding length L_w and the welding speed v_s (9):

$$t = L_w / v_s \quad (9)$$

The total welding length L_w is the product of the total number of passes n and the weld pass length L_{seam} (10):

$$L_w = n L_{seam} \quad (10)$$

Thus, Eq. (8) can be rewritten as follows (11):

$$E_{in} = Q_{in} \frac{n L_{seam}}{v_s} \quad (11)$$

The number of weld passes n can be calculated based on the total cross section to weld A_w and each weld pass cross section A_s (12):

$$n = A_w / A_s \quad (12)$$

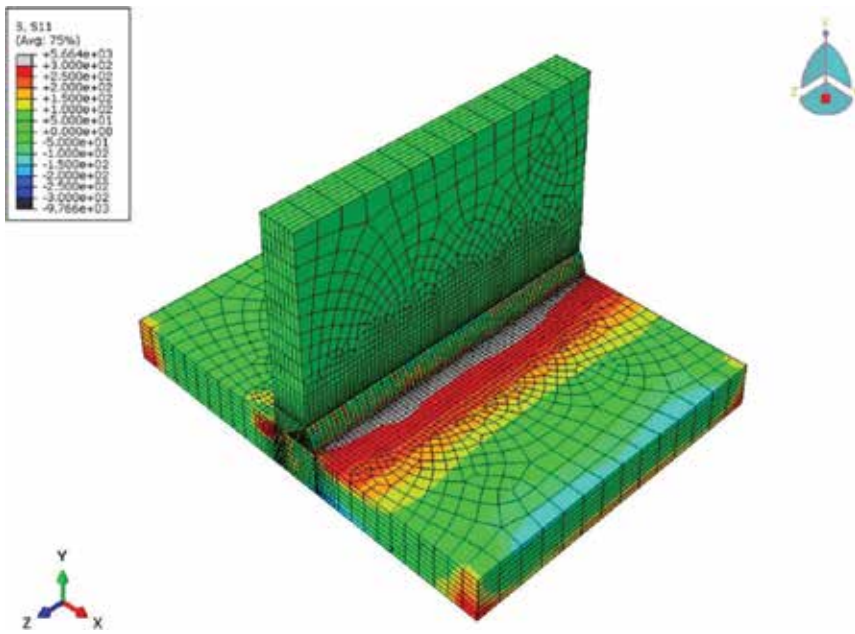


Figure 21. RS pattern of case study T-joint_40.

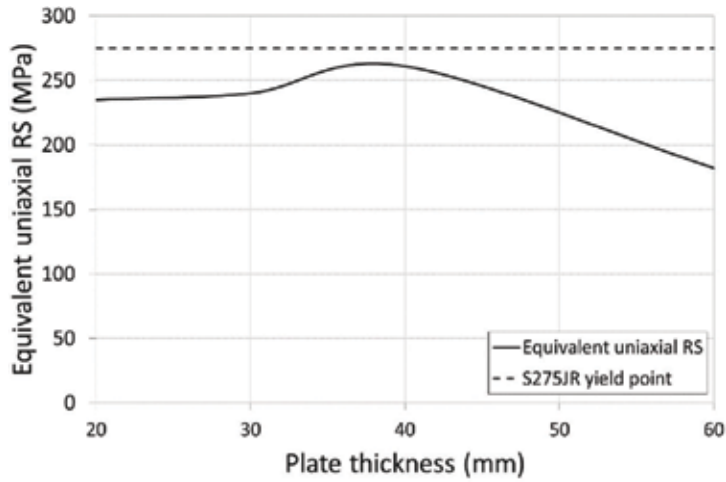


Figure 22. Maximum equivalent uniaxial stress vs. thickness.

Figure 23 shows that number of passes n increases quadratic with the plate thickness th . Consequently, it can be concluded that the total heat energy supplied to the welded plates, which is proportional to the number of passes, also presents a quadratic behaviour.

On the other hand, Eq. (13) describes the heat capacitance C_{plate} of the welded plates:

$$C_{plate} = \rho V_{plate} c_p \tag{13}$$

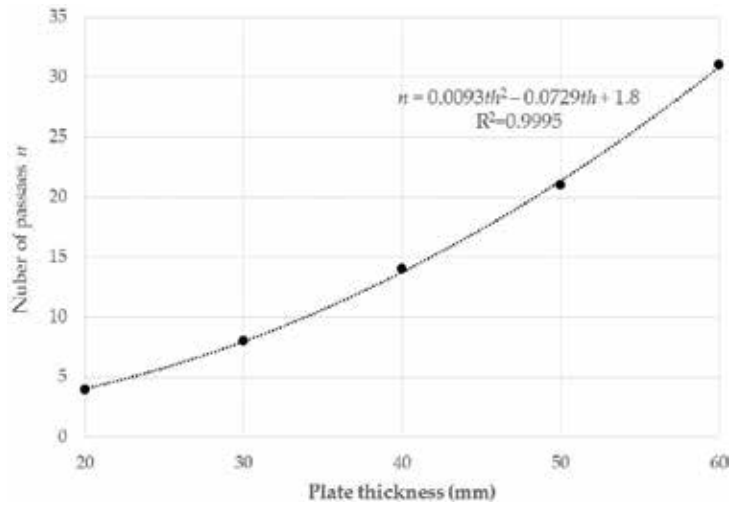


Figure 23. Number of weld passes according to plate thickness.

where ρ is the plate material density, V_{plate} is the volume of the welded plates and c_p is the specific heat of the plate material.

Figure 24 shows the evolution of the supplied total heat energy E_{in} and the heat power supply to plate heat capacitance ratio $Q_{\text{in}}/C_{\text{plate}}$ with the plate thickness increase, which represents the plate average temperature increase rate without considering heat losses through convection. It can be observed that, even the total heat increase presents a quadratic increase, the $Q_{\text{in}}/C_{\text{plate}}$ ratio decreases abruptly with thickness due to plate volume and, consequently, heat

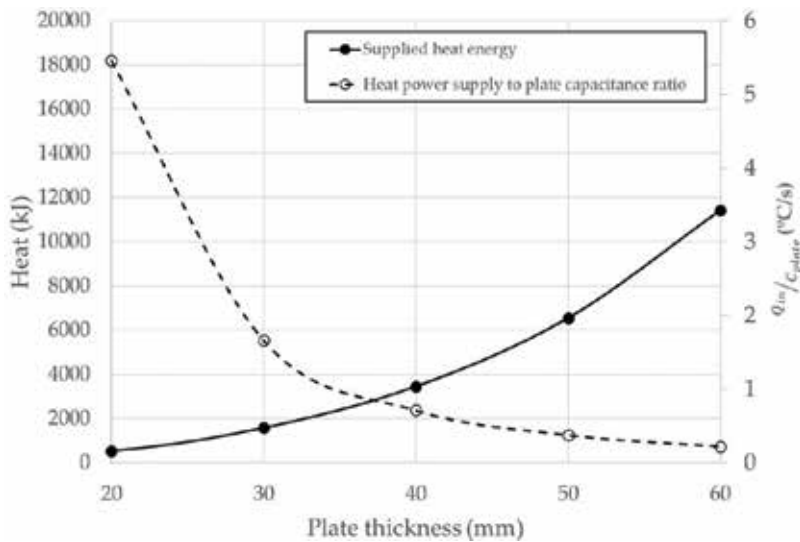


Figure 24. Evolution of total heat supply and heat power supply to plate heat capacitance ration with the plate thickness increase.

capacitance cubic increase. Thus, for plate thickness over 38 mm, the average plate temperature increase ratio is below 1°C/s. Therefore, it is observed that for low plate thickness, the provided total heat is predominant over the heat absorption capacity. In contrast, for high thickness, the heat absorption capacity increase overtakes the provided total heat effect.

5. Conclusions

In the present chapter, a procedure to predict RS pattern in spray transfer multipass welding where the heat source is defined based on the welding physics is described and validated. The procedure does not require any welding experimental characterisation to define FEM input parameters, which enables its use as a predictive tool. Results showed good correlation, with an average deviation of 9.15% in the thermal field and 42 MPa in the RS field.

Following, the influence of plate thickness and number of passes in the RS pattern of thick T-joint welds is conducted. Results have shown that, in the studied range, the assumption of considering RS value as the yield stress (YS) [18,-20] is reasonable for low thickness plates, where RS around 85–95% of YS is observed. However, RS value can decrease down to 66% of the YS for high thickness plate welds.

Author details

Jon Ander Esnaola*, Ibai Ulacia, Arkaitz Lopez-Jauregi and Done Ugarte

*Address all correspondence to: jaesnaola@mondragon.edu

Structural Mechanics and Design, Engineering Faculty, Mondragon Unibertsitatea, Mondragón, Spain

References

- [1] Naidu DS, Moore KL, Ozcelik S. Modelling Sensing and Control of Gas Metal Arc Welding. Kilmington: Elsevier Science Ltd.; 2003
- [2] Gery D, Long H, Maropoulos P. Effects of welding speed, energy input and heat source distribution on temperature variations in butt joint welding. *Journal of Materials Processing Technology*. 2005;**167**(2):393-401
- [3] Mousavi M, Haeri M. Estimation and control of droplet size and frequency in projected spray mode of a gas metal arc welding (GMAW) process. *ISAT*. 2001;**50**(3):409-418
- [4] Murray PE. Selecting parameters for GMAW using dimensional analysis. *Welding Journal*. 2002;**81**(7):125-131

- [5] Maddox SJ. Fatigue strength of welded structures. Woodhead publishing. 1991
- [6] Sattari-Far I, Farahani MR. Effect of the weld groove shape and pass number on residual stresses in butt welded pipes. *International Journal of Pressure Vessels and Piping*. 2009;**86**(11):723-731
- [7] Brickstad B, Josefson BLA. Parametric study of residual stresses in multi-pass butt welded stainless steel pipes. *International Journal of Pressure Vessels and Piping*. 1998;**75**(1):11-25
- [8] Keivani R, Jahazi M, Pham T, Khodabandeh AR, Afshar MR. Prediction of residual stresses and distortion during multisequence welding of large size structures using FEM. *International Journal of Advanced Manufacturing Technology*. 1-11
- [9] Asadi M, Goldak J, Nielsen J, Zhou J, Tchernov S, Downey D. Analysis of predicted residual stress in a weld and comparison with experimental data using regression model. *International Journal of Mechanics and Materials in Design*. 2009;**5**:353-364
- [10] Deng D, Murakawa H. Numerical simulation of temperature field and residual stress in multi-pass welds in stainless steel pipe and comparison with experimental measurements. *Computational Materials Science*. 2006;**37**(3):269-277
- [11] Turski M, Francis JA, Hurrell PR, Bate SK, Hiller S, Withers PJ. Effects of stop-star features on residual stresses in a multipass austenitic stainless steel weld. *International Journal of Pressure Vessels and Piping*. 2012;**89**:9-18
- [12] Philipenko A. Computer simulation of residual stress and distortion of thick plates in multi-electrode submerged arc welding. Their mitigation techniques. PhD thesis, Norwegian University of Science and Technology. 2001
- [13] Radaj D. Heat Effects of Welding. Berlin: Springer; 1992
- [14] Chang P-H, Teng T-L. Numerical and experimental investigations on the residual stresses of the butt-welded joints. *Computational Materials Science*. 2004;**29**:511-522
- [15] Messler RW. Principles of Welding Processes, Physics, Chemistry, and Metallurgy. Troy, NY: John Wiley & Sons; 2008
- [16] Paradowska A, Price JW, Ibrahim R, Finlayson T. A neutron diffraction study of residual stress due to welding. *Journal of Materials Processing Technology*. 2005;**164**:1099-1105
- [17] Navas VG. Optimización de procesos de mecanizado mediante control de tensiones residuales y otros parámetros de integridad superficial. PhD thesis, Campus Tecnológico de la Universidad de Navarra, Spain. 2006
- [18] Sonsino CM. Multiaxial fatigue assessment of welded joints-recommendations for design codes. *International Journal of Fatigue*. 2009;**31**(1):173-187
- [19] Radaj D, Sonsino CM, Fricke W. Fatigue assessment of welded joints by local approaches. Woodhead publishing. 2006

- [20] Lassen T, Recho N. Fatigue life analysis of welded structures. London: Wiley-ISTE; 2006
- [21] Lopez-Jauregi A, Esnaola JA, Ugarte D, Torca I, Larranaga J. Procedure to predict residual stress pattern in spray transfer multipass welding. *International Journal of Advanced Manufacturing Technology*. 2014;**76**:2117-2129
- [22] Hansen JL. Numerical modelling of welding induced stresses. PhD thesis, Technical University of Denmark. 2003
- [23] Rosenthal D. Mathematical theory of heat distribution during welding and cutting. *Welding Journal*. 1941;**20**(5):220-234
- [24] Pavelic V, Tanbakuchi R, Uyehara OA, Myers PS. Experimental and computed temperature histories in gas tungsten arc welding of thin plates. *Welding Journal*. 1969;**48**(7):295
- [25] Goldak J, Chakravati A, Bibby M. A new finite element model for welding heat sources. *Metallurgical Transactions B*. 1984;**15**(2):299-305
- [26] Chen B-Q, Hashemezadeh Guedes Soares C. Numerical and experimental studies on temperature and distortion patterns in butt welded plates. *International Journal of Advanced Manufacturing Technology*. 2014;**72**:1121-1131
- [27] Zhu F, Xu C, Zeng L. Coupled finite element analysis of MIG welding assembly on auto-body high-strength steel panel and door hinge. *International Journal of Advanced Manufacturing Technologies*. 2010;**51**:551-559
- [28] Lidam RN, Manurung YHP, Haruman E. Angular distortion analysis of the multipass welding process on combined joint types using thermo-elastic-plastic FEM with experimental validation. *International Journal of Advanced Manufacturing Technologies*. 2013;**69**:2373-2386
- [29] Price J, Paradowska A, Joshi S, Finlayson T. Residual stresses measurements by neutron diffraction and theoretical estimation in a single weld bead. *International Journal of Pressure Vessels and Piping*. 2006;**83**:381-387
- [30] Barsoum Z, Barsoum I. Residual stress effects on fatigue life of welded structures using LEFM. *Engineering Failure Analysis*. 2009;**16**(1):449-846
- [31] Pichot F, Danis M, Lacoste E, Danis Y. Numerical definition of an equivalent GTAW heat sources. *Journal of Materials Processing Technologies*. 2013;**213**(7):1241-1248
- [32] Wahab MA, Painter MJ. Numerical model of gas metal arc weld using experimentally determined weld pool shapes as the representation of the welding heat source. *International Journal of Pressure Vessels and Piping*. 1997;**73**(2):153-159
- [33] Barsoum Z. Residual stress prediction and relaxation in welded tubular joint. *Weld World*. 2007;**51**(1-2):23-30
- [34] Hu J, Tsai HL. Heat and mass transfer in gas metal arc welding. Part I: The arc. *International Journal of Heat and Mass Transfer*. 2007;**50**(5):833-846

- [35] Hu J, Tsai HL. Heat and mass transfer in gas metal arc welding. Part II: The metal. *International Journal of Heat and Mass Transfer*. 2007;**50**(5):808-820
- [36] Xu G, Hu J, Tsai HL. Three-dimensional modeling of arc plasma and metal transfer in gas metal arc welding. *International Journal of Heat and Mass Transfer*. 2009;**52**(7):1709-1724
- [37] Norrish J. *Advanced welding processes*. Institute of Physics. 1992
- [38] Lesnewich A. Commentary on GMAW. Parameter selection paper. 2003
- [39] Palani PK, Murugan N. Modeling and simulation of wire feed rate for steady current and pulsed current gas metal arc welding using 317L flux cored wire. *International Journal of Advanced Manufacturing Technologies*. 2007;**34**:1111-1119
- [40] Murray PE. Selecting parameters for GMAW using dimensional analysis. *Welding Journal*. 125-131
- [41] Modenesi PJ, Reis RI. A model for melting rate phenomena in GMA welding. *Journal of Materials Processing Technologies*. **189**:199-205
- [42] Palani PK, Murugan N. Selection parameters of pulsed current gas metal arc welding. *Journal of Materials Processing Technologies*. 2006;**172**:1-10
- [43] Zamiri-Akhlaghi F. Welding simulation and fatigue assessment of tubular K-joint in high-strength steel. PhD thesis, École Polytechnique Fédérale de Lausanne, Switzerland. 2014
- [44] Teng TL, Fung CP, Chang PH. Effect of weld geometry and residual stresses on fatigue in butt-welded joints. *International Journal of Pressure Vessels and Piping*. 2002;**79**:476-492
- [45] Payares-Asprino MC, Katsumoto H, Liu S. Effect of martensite start and finish temperatures on residual stress development in structural steel welds. *Welding Journal*. 2008;**87**:279-289
- [46] Deng D. FEM prediction of welding residual stress and distortion in carbon steel considering phase transformation effects. *Materials and Design*. **30**(2):359-366
- [47] APTA (Asociación para la Promoción Técnica del Acero) [Internet]. Available from: <http://apta.com.es/pdf/aceros.pdf> [Accessed: 11-06-2014]
- [48] Electric L. GMAW welding guide [Internet]. Available from: <http://www.oemeyer.com/Media/Default/Industrial/technical/MIG%20welding%20guide-lincoln.pdf> [Accessed: 11-06-2014]
- [49] Ranjabamodeh E, Pouranavari M, Fischer A. Influence of welding parameters on residual stresses in dissimilar HSLA steels welds. Association of Metallurgical Engineers of Serbia. 2013
- [50] Mills KC. *Recommended Values of Thermophysical Properties for Selected Commercial Alloys*. Cambridge, England: Woodhead Publishing; 2002

- [51] Thermal conductivity for carbon steel AISI 1010 [Internet]. Available from: http://www.egunda.com/materials/alloys/carbon_steels/show_carbon.cfm?ID=AISI_1010&show_prop=tc&Page_Title=Carbon%20Steel%20AISI%201010 [Accessed: 11-06-2014]
- [52] Pitz M, Merklein M. FE simulation laser assisted bending. Proceedings of the 11th International Conference: Sheet Metal. 745-752
- [53] Tensile properties at high temperature for S275 steel [Internet]. Available from: http://www.thyssenfrance.com/fich_tech_en.asp?product_id=17930 [Accessed: 11-06-2014]
- [54] EN 1993-1-2: Eurocode 3: Design of Steel Structures-Part 1-2: General Rules-Structural Fire Design. 2005
- [55] Safety data sheet for Stargon 82 [Internet]. Available from: <http://www.cialgas.com/wp-content/uploads/2012/09/STARGON-82.pdf> [Accessed: 11-06-2014]
- [56] Larrañaga J. Geometrical accuracy improvement in flexible roll forming process by means of local heating. PhD thesis, Mondragon Unibertsitatea. 2011
- [57] Withers PJ, Bhadeshia HKDH. Residual stress. Part 1-measurement techniques. *Materials Science and Technology*. 2001;**17**(4):355-365
- [58] Lopez-Jauregi A, Esnaola JA, Ulacia I, Urrutibeaskoa I, Madariaga A. Fatigue analysis of multipass welded joints considering residual stresses. *International Journal of Fatigue*. 2015;**79**:75-85

Numerical Simulation of Residual Stresses in Welding and Ultrasonic Impact Treatment Process

Lanqing Tang, Ayhan Ince and Jing Zheng

Additional information is available at the end of the chapter

<http://dx.doi.org/10.5772/intechopen.72394>

Abstract

Welding technology is considered as a reliable and efficient joining method, which has been widely used in almost all the industry departments. Detrimental factors induced by welding such as micro-cracks/flaws, tensile residual stresses, high stress concentration may degrade the mechanical and fatigue properties of weld joints. Ultrasonic impact treatment (UIT) is considered one of the most efficient post-weld treatment which could improve the fatigue performance of weld joints. In this study, the effect of the UIT on residual stress distribution of 304L weld joints was particularly investigated. FE analysis simulation and the XRD experiment were performed to predict and measure residual stresses of both as-welded and the UIT-treated joints. Compared results show that simulated stresses are in good agreement with the experimental results along various paths, confirming the validity of welding model. The UIT introduces a compressive residual stress layer with depth between 2 and 3 mm near the impacting surface of weld joint.

Keywords: ultrasonic impact treatment (UIT), finite element modeling (FEM), weld residual stress, stress and strain, weld simulation

1. Introduction

Welding technology has been widely applied in the fields of automobile, aviation, nuclear, vessel manufacturing and other industrial sectors due to its low cost, geometrical flexibility and desirable mechanical properties [1]. On the other hand, welding comes with the expense of some detrimental effects on welded structures such as micro-cracks/flaws, high stress concentration and tensile residual stresses. Hence, from the point view of fatigue design, welded areas are deemed as weak structural joints where cracks and tensile residual stresses are easy to be found [2]. A number of numerical techniques have been developed to model the

influence of tensile residual stresses on fatigue strength of welded joints [3–6]. Over the past several decades, numerous post-weld treatment techniques, including grinding, TIG dressing, hammer peening and shot peening, have been developed to address this vexing issue and improve fatigue performance of weld joints [7]. These treatments are generally classified into two different categories: geometry improvement and residual stress modification techniques. Geometry improvement techniques such as TIG dressing and grinding focus on eliminating flaws and reducing stress concentration of welded components. While residual stress modification techniques like hammer peening and shot peening lay emphasis on introducing beneficial compressive residual stresses and improving residual stress distributions of welded joints [8].

Ultrasonic impact treatment (UIT) is a recently introduced treatment technique developed by Statnikov et al. in former Soviet Union [9]. This technique has become increasingly popular for several reasons such as reducing manpower requirements, eliminating the weld induced distortions. The UIT uses needles or hammer-like rods to impact the welding surface/toe at a high ultrasonic frequency of 18,000–27,000 Hz. The UIT, not only reduces the local stress concentration by modifying the weld toe geometry but also introduces compressive residual stresses by eliminating tensile residual stresses and introducing beneficial compressive stresses [10].

In recent years, numerous studies have been carried out to investigate effects of the UIT on the weld residual stresses and fatigue performance of weld joints [11–14]. A number of numerical models have been developed to predict the residual stress distribution and fatigue performance of UIT-treated weld joints [13, 15]. Meanwhile, experimental studies of the UIT have been also conducted [11, 12, 14]. Various measurement techniques such as X-ray diffraction and neutron diffraction were used to obtain experimental data for the validation of simulated residual stresses. In most of the cases, it has been found that the UIT introduces compressive residual stresses along varying depths and improves fatigue performances of weld joints in various extent. Turski et al. [11] found that the UIT produced compressive residual stress fields of about 2 mm in depth for 304 stainless steel. Liu et al. [12] measured residual stresses of UIT-treated high strength steel weld joints. The results indicated that the UIT had the same effect on both longitudinal and transverse stresses and introduced a compressive residual stress layer up to 4 mm in depth. Foehrenbach et al. [13] developed a computationally efficient approach to predict residual stresses induced by the UIT process using a commercial finite element software package. It was found that compressive residual stresses up to a base material yield strength occurred after the UIT treatment. Dekhtyar et al. [14] studied the effect of the UIT on fatigue behavior of Ti–6Al–4V specimens. Based on experimental data, it was reported that the UIT introduced compressive stresses of -570 MPa, achieving two thirds of yield limit of the material. Fatigue strength of as-welded joints increased by 60% at 10^7 cycles and fatigue life was extended 10^2 times at stress amplitude of 300 MPa.

To assess fatigue life improvement by the UIT treatment, it is necessary to accurately estimate residual stress distribution through finite element analysis (FEA). Recent numerical studies emphasized on the influence of mesh type, material properties, boundary conditions, pin tool size, modeling strategy and material hardening rules on computed numerical results

[13, 15, 16]. It was well known that the isotropic hardening model is valid for monotonic loading [9]. However, due to the Bauschinger effect, isotropic hardening model is not suitable for cyclic loadings experienced under of the UIT process [17]. On the other hand, linear kinematic hardening model could be adopted to describe material deformation behavior under cyclic loading conditions, but it could provide reasonable results under small strains loading conditions [18]. Therefore, the combined isotropic-kinematic hardening model, or Chaboche model was applied to the UIT simulation [19, 20]. In addition, in the modeling of the UIT process, regardless the complex components and ultrasonic transducer of the UIT device, the pin impact can be simplified as the movement of the impact pin tool given proper controlling parameters. These parameters consist of impact velocity, the contact force and the pin displacement. Hence, modeling strategies of the UIT can be classified into three categories: velocity-controlled simulation (VCS), force-controlled-simulation (FCS) and displacement-controlled-simulation (DCS) [21–23]. In the VSC strategy, the velocity of the impact pin can be obtained through the approximated motion using a sinusoidal harmonic function, where the first derivative represents the velocity [17]. The FCS strategy defines the pin impact with a given load force while the DCS utilizes the permanent indentation obtained by the UIT to define the displacement of the pin [22, 23].

This paper focuses on effects of the UIT on residual stresses of 304L weld joints. FE analysis was carried out to simulate residual stress distributions of as-welded and the UIT-treated joints. The UIT process was simulated with the pre-existing validated stress field of residual stresses, which considered the effects of the UIT in transverse, longitudinal and through-thickness directions. In addition, the DCS and Chaboche model was introduced to improve both the time efficiency and the preciseness of prediction.

2. Finite element (FE) modeling

2.1. FE modeling of weld joints

FE simulation of both butt and T weld joints have been performed using the Coupled Temperature-Displacement analysis provided by ABAQUS software package. The 3-D finite element models of butt joint and T-joint are depicted in **Figure 1**. As shown in **Figure 2**, to reduce the computation time, the FE models of welded joints were reduced by one-half and one-quarter using the overall symmetry and both models were simplified as the single pass welding. Geometries of both butt and T weld joints were modeled with the C3D8T element. In order to improve computed results, the refined meshes with the minimum element size of $1 \times 1 \times 1$ mm were created in the heat affected zone (HAZ) and the weld area of FE models. The butt joint had 251,585 nodes while the T-joint had 240,692 nodes. Outer surfaces of weld joints were under both radiation and convection condition with emissivity of 0.85 and filming coefficient of $10 \text{ W}/(\text{m}^2\text{C})$. As shown in **Figure 2(a)**, for the butt joint, nodes on symmetry plane Y-Z, line H-I/G-J and line G-H were constrained in X-direction, Y-direction and Z-direction, respectively. For the T-joint, similarly, nodes on symmetry plane Y-Z, line F-I/G-H and line F-G were restricted in X axis, Y axis and Z axis, respectively. As seen in

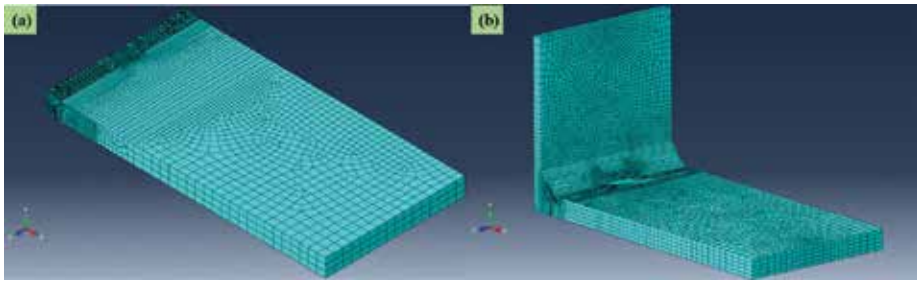


Figure 1. 3-D finite element model: (a) butt joint and (b) T-joint.

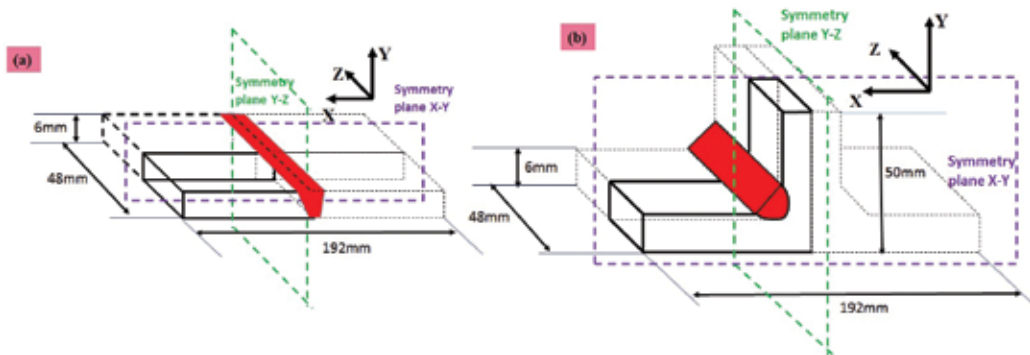


Figure 2. A schematic representation of weld geometry: (a) butt joint and (b) T-joint.

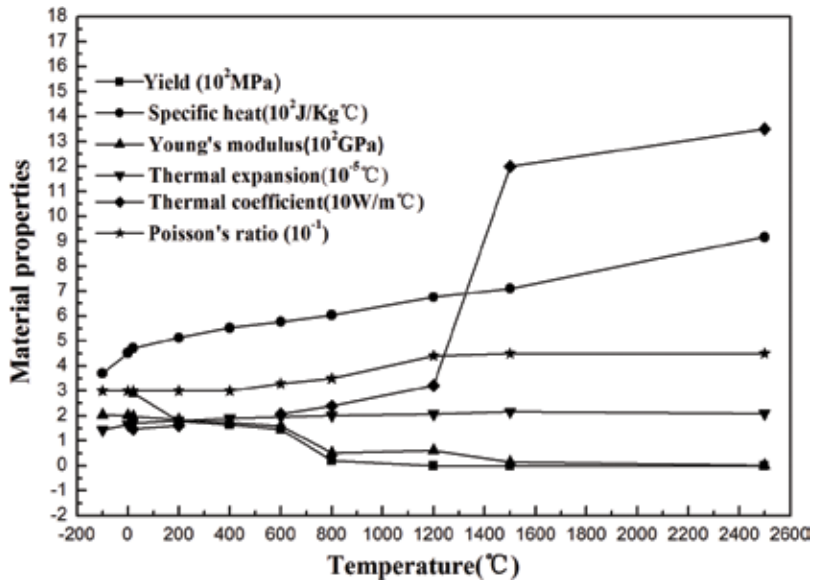


Figure 3. Thermal properties and mechanical properties.

Material	C	Si	Mn	Cr	Ni	S	P	Fe
Base metal (06Cr19Ni10)	0.045	0.45	1.10	17.1	8.00	0.001	0.028	Rest
Electrode (ER308L)	0.03	0.60	1.80	20.0	10.0	0.008	0.015	Rest

Table 1. Chemical composition of base metal and welding electrode (wt%).

Figure 3, temperature dependent properties of 304L were obtained from the literature [24]. A double-ellipsoid heat source model was adopted in numerical simulation of welding process. The actual welding experimental data for welding process and parameters was listed in **Tables 1** and **2**.

2.2. FE modeling of UIT process

In the FE modeling of the UIT process, residual stress results obtained from the welding process were taken as the initial model state. As shown in **Figure 4**, in the middle of the weld zone, an impact area with the minimum element size of $0.1 \times 0.1 \times 0.5$ mm were created in the weld simulation to achieve refined mesh area for the impact simulation so that a re-meshing routine could be avoided to reduce computational time during the UIT simulation. For the material hardening rule, the combined isotropic and kinematic model was used to characterize the material deformation behavior in the FE model of the UIT simulation. The DCS strategy was adopted to control the displacement motion of the pin tool. The pin was set to hit the weld toe at the speed of 2 m/s until it reached the design depth, which was considered as one complete impact. **Figure 5** shows the position and indentation of pin tool for both the butt and T joints. The diameter and the permanent indentation of the pin were 3 and 0.1 mm respectively. The angles of pins in butt joint and T-joint were determined as 75 and 67.5°, respectively. The pin model was modeled as a discrete rigid body and, the pin was traveling along the welding direction and hitting the weld joint every 0.3 mm to ensure a sufficient overlap during the UIT treatment. It was worth noting that in the DCS strategy, the speed of the UIT treatment was considered to be non-essential.

Parameter name	Value
Welding voltage (volts)	24.5
Welding current (amperes)	217
Welding speed (cm/min)	40
Electrode type	ER308L
Welding electrode diameter (mm)	1.2
Shielding gas type	Argon (97%), O ₂ (3%)
Shielding gas flow rate (L/min)	20

Table 2. Welding parameters of MIG welding technology.

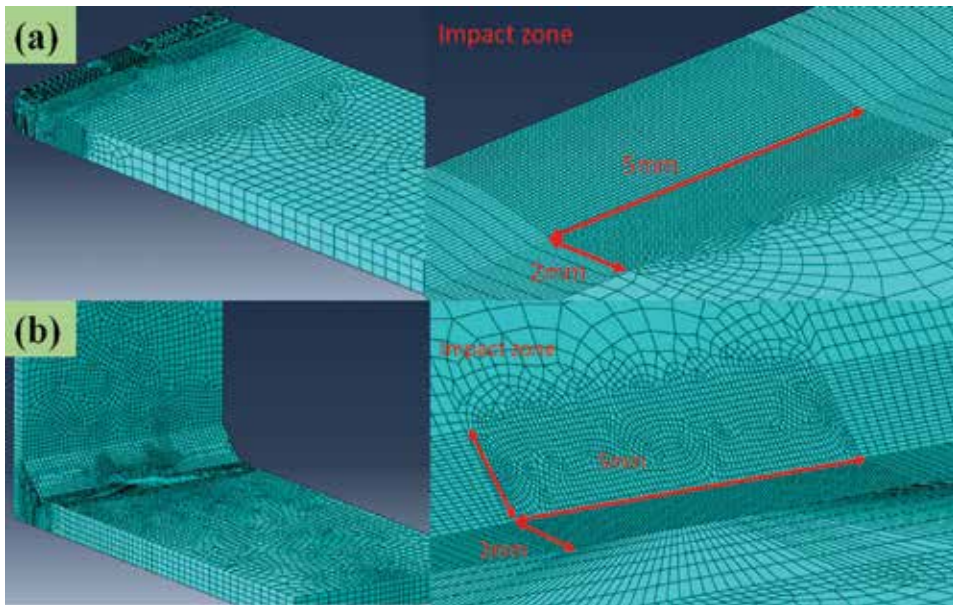


Figure 4. Impact zone of UIT simulation: (a) butt joint and (b) T-joint.

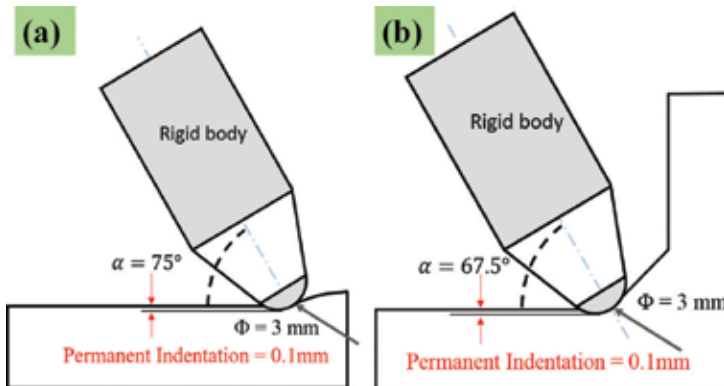


Figure 5. Pin tool position and indentation: (a) butt joint and (b) T-joint.

3. Discussions and results

As shown in **Figures 6–11**, paths A-B, A-C and A-D were selected to evaluate residual stress distributions for the both butt and T joints. Meanwhile, in order to describe residual stresses in directions of X, Y and Z axes, three specific words “transverse,” “through-thickness” and “longitudinal” were introduced. The transverse residual stress, the through-thickness residual stress and the longitudinal residual stress indicated σ_{xx} , σ_{yy} and σ_{zz} , respectively.

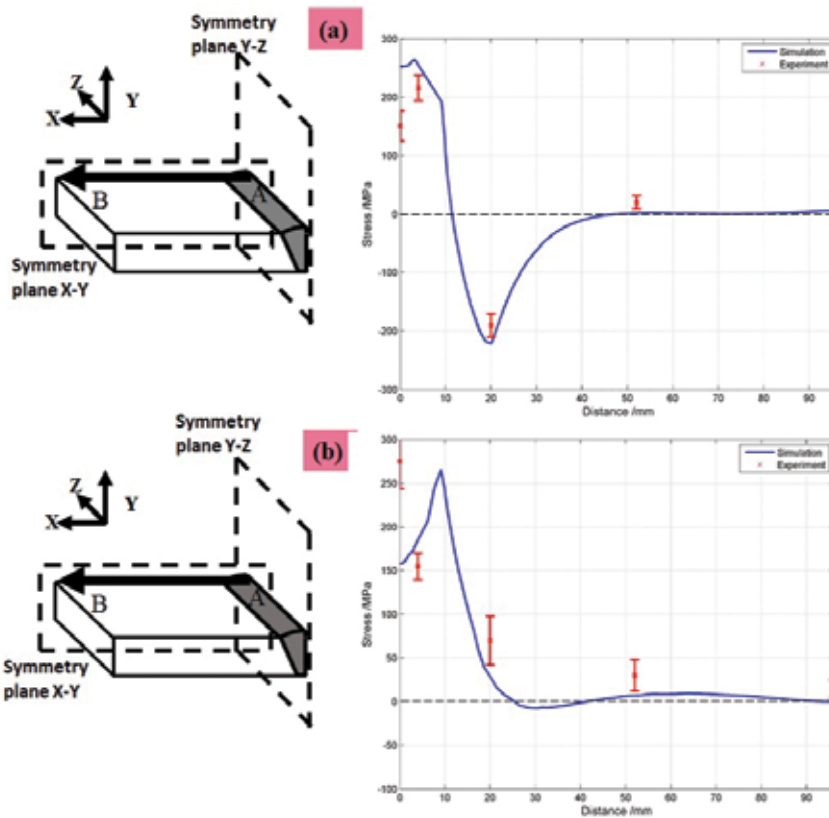


Figure 6. Transverse (a) and longitudinal (b) residual stress distributions along A-B path in butt welded joints.

3.1. Residual stress predictions in weld butt joint

For validating the FE model of welding process, experimental data obtained from previous works [25, 26] were compared with the predicted residual stress results. As shown in **Figures 6** and **7**, predicted and experimental residual stresses of butt joint along paths A-B and A-C are compared, respectively. In particular, the blue lines and the red dots marked in figures demonstrate the predicted residual stresses by FEA and the experimental data obtained by the XRD method, respectively. As depicted in **Figure 6**, both σ_{xx} and σ_{zz} reached their maximum values near the weld zone, then dropped as distance from the point A increased and finally stabilized around the zero value. Additionally, it was found that the simulation results are in good agreement with the experimental results along the A-B path, confirming the prediction capability of welding model.

Figure 7 shows the predicted and measured transverse residual stresses along the A-C path. Obviously, at the point A, the point C and in their vicinity, the residual stresses are compressive stresses. In the middle of the A-C path, the transverse residual stresses converted into tensile stresses with peak value of 275 MPa. It was also indicated that there existed some

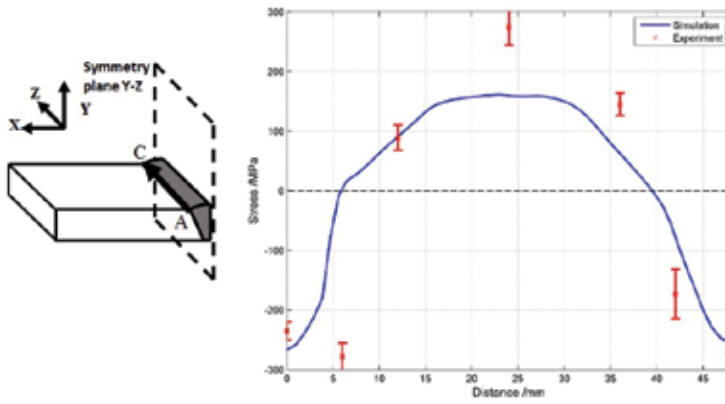


Figure 7. Transverse residual stress distributions along A-C path in butt welded joints.

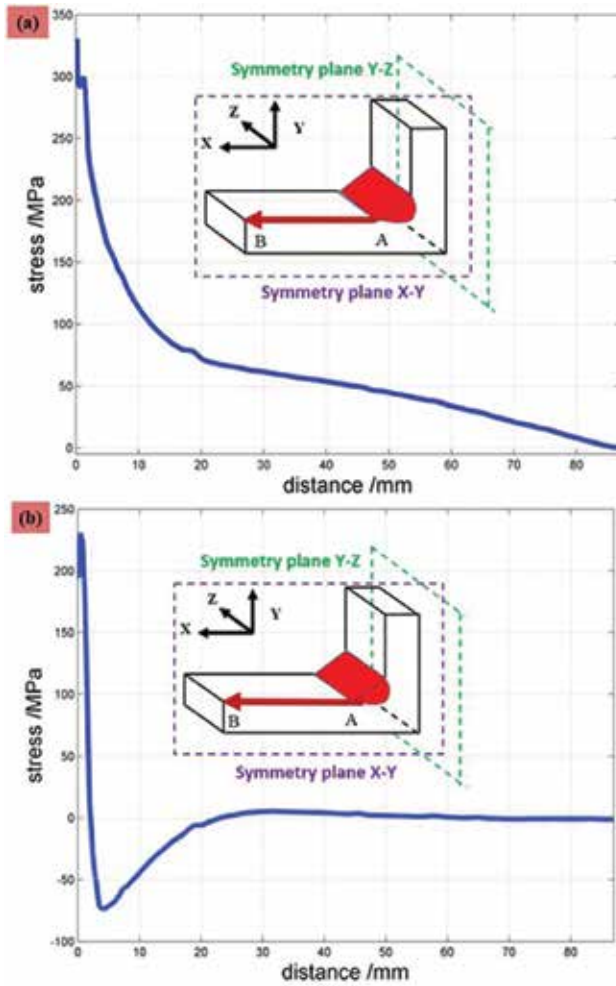


Figure 8. Transverse (a) and longitudinal (b) residual stress distributions along A-B path in T-joints.

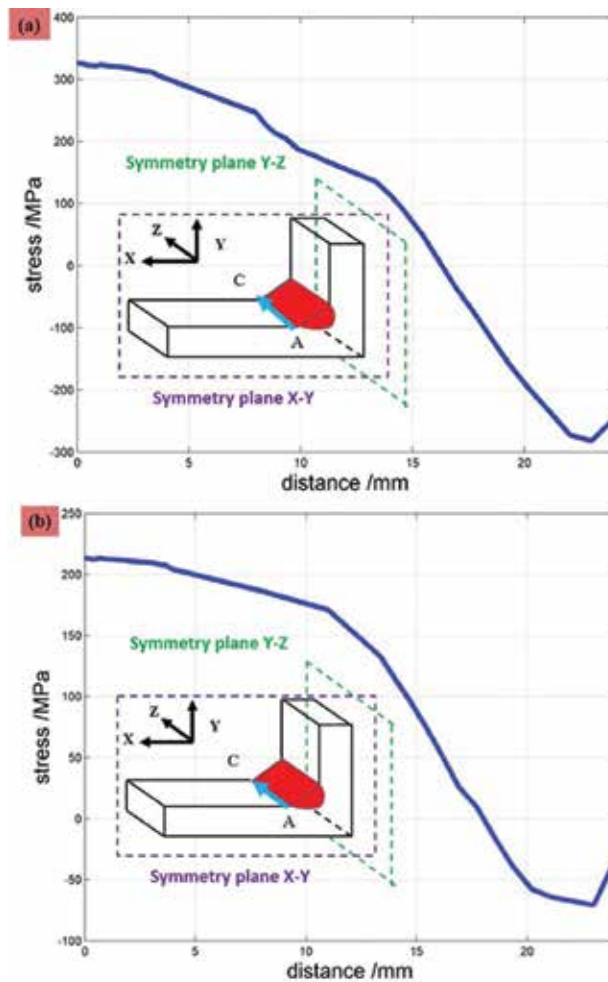


Figure 9. Transverse (a) and longitudinal (b) residual stress distributions along A-C path in T-joints.

errors between the calculated results and the measured ones. The measured residual stresses were higher in the middle of the A-C path but lower at each end of the A-C path. Those errors may be attributed to the measurement error of the XRD method, which was sensitive to the microstructure evolution of welding zone [10].

3.2. Residual stress predictions in weld T-joint

Figures 8 and 9 depict residual stresses of T-joint along the path A-B and path A-C, respectively. As shown in **Figure 8**, along the path A-B, both the transverse residual stress σ_{xx} and the longitudinal residual stress σ_{zz} achieved their peaks in the vicinity of weld area. Nevertheless, with the distance from the point A, transverse residual stresses showed a relatively different trend with the longitudinal residual stresses. Transverse residual stresses decreased as the distance from the point A increased and dropped to the zero value at the point B, shown in **Figure 8(a)**. Unlike the transverse residual stresses, longitudinal residual

stresses first dropped dramatically with the increasing distance from the point A and reached the compressive peak value of -75 MPa at the distance of approximately 5 mm from the point A. Then longitudinal residual stresses increase significantly to zero at the distance of 25 mm from the point and remained stable. Notably, both transverse and longitudinal residual stresses changed into negligible values in the relatively far distant from the weld zone, which was consistent with the results of previous studies [27, 29–31, 34, 35].

Figure 9(a) and **(b)** demonstrate transverse and longitudinal residual stresses along the A-C path of the T-joint, respectively. Obviously, the distribution trend of the transverse residual stresses was in line with that of the longitudinal residual stresses. Both the transverse and longitudinal residual stresses obtained their peak values of 345 and 205 MPa in the middle of the welding line (near point A). With the increasing distance from the point A, transverse and longitudinal stresses dropped, changing from the tensile values into the compressive ones. The maximum compressive value of transverse residual stresses (-285 MPa) were considerably higher than that of longitudinal residual stresses (-70 MPa).

3.3. Effects of UIT on weld residual stresses

In order to evaluate the effects of the UIT on residual stresses along the A-D path (the depth direction), FE simulation residual stresses for the UIT-treated model were analyzed and compared with those for the as-welded model. **Figures 10** and **11** depict residual stresses of butt joint and T-joint, respectively. As shown in **Figure 10**, before the UIT, the transverse, longitudinal and through-thickness residual stresses of butt weld joint remained stable along the A-D path, with the average values of 189, 267 and 9 MPa. After the UIT, near the upper impacting surface of butt weld joint, the transverse, longitudinal and through-thickness residual stresses changed into compressive stresses with peak values of -150 , -355 and -75 MPa. As for the T-joint, before the UIT, high tensile stresses which were close to the yield strength of the base metal appeared near the upper surface of the as-welded joint. The maximum values of the transverse, longitudinal and through-thickness residual stresses were 364, 372 and 151 MPa. Like the butt joint, after the UIT, the transverse, longitudinal and through-thickness residual stresses of T-joint also transformed into the compressive stresses. The peak values of compressive stresses in the transverse direction, the longitudinal direction and the through-thickness direction were -255 , -320 and -70 MPa, respectively. It was noteworthy that the maximum compressive stresses in the longitudinal direction for both butt joint and T-joint were relatively higher than the compressive limit of 304L steel, which implied cold working by the UIT induced plastic deformation of the weld joint. The similar level of compressive residual stresses higher than the material's yield limit was also obtained and reported by previous studies [11, 28, 32].

It was also found that the influence of the UIT decreased with depth. For the butt joint, the depth of compressive stresses in three directions was around 2 mm. Similarly, as for the T-joint, the effective depth of compressive layer in the transverse, longitudinal and through thickness directions introduced by the UIT were 2.5, 2.3 and 3.1 mm, respectively. The depths of compressive residual stresses by UIT were similar with the results of previous studies [33].

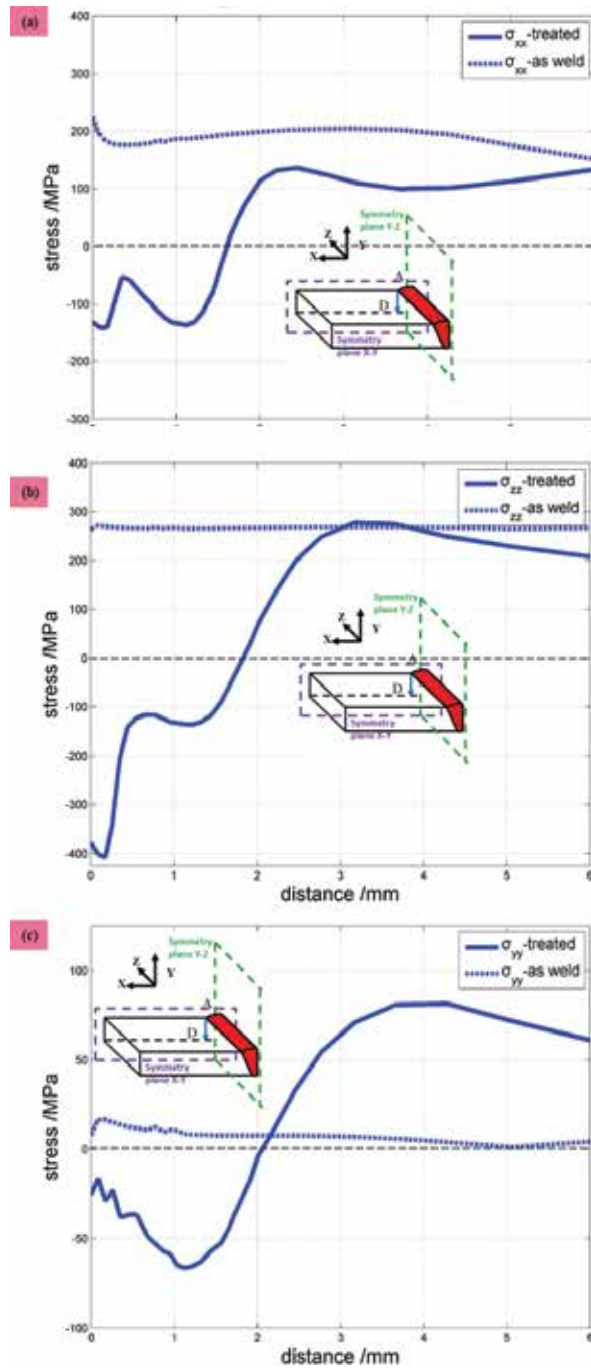


Figure 10. Transverse (a), longitudinal (b) and through-thickness (c) residual stress distributions along A-D path in as-welded and UIT-treated butt joints.

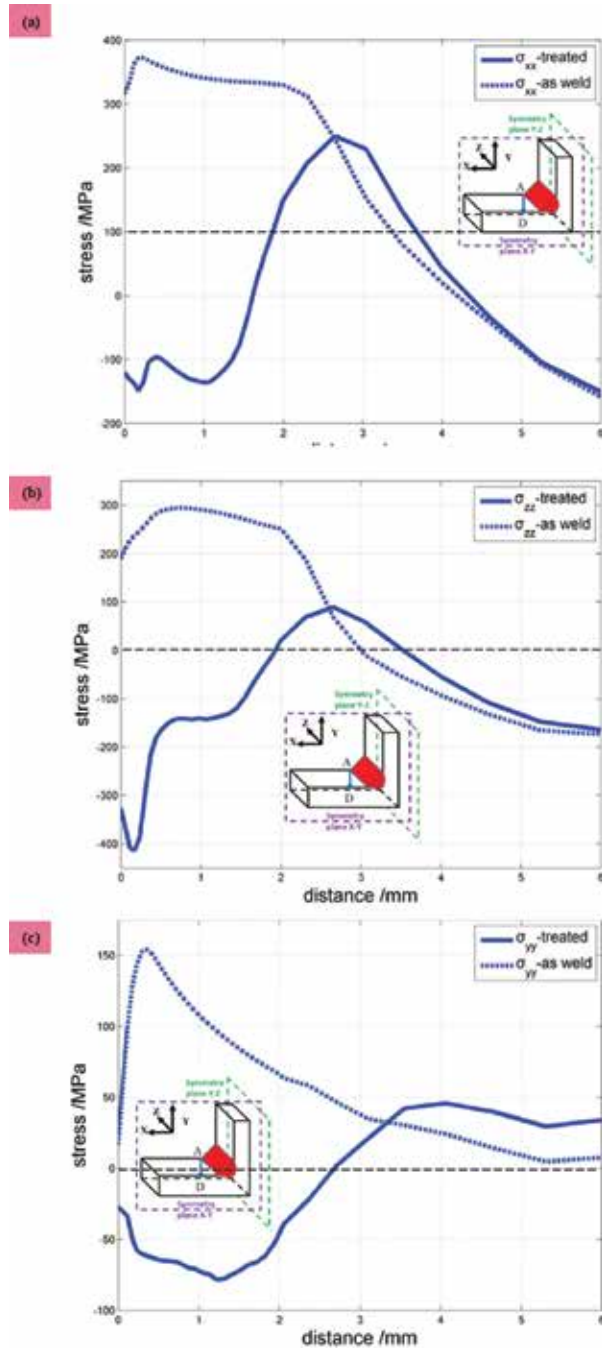


Figure 11. Transverse (a), longitudinal (b) and through-thickness (c) residual stress distributions along A-D path in as-welded and UIT-treated T-joints.

The FE residual stress results in UIT-treated weld joint demonstrated that the UIT introduced compressive residual stress layer with various depth, which brought beneficial effect on fatigue strength of the material [7, 33–38].

4. Conclusions

This study focuses on evaluating effects of the UIT on the residual stresses of 304L butt and T-joints. FEA method was used to simulate both the welding and the UIT processes. To validate the prediction accuracy of the welding model, experimental data were compared with the simulated ones. Based on the results, the following conclusions can be drawn:

1. Both the simulation and the experimental results indicated that residual stresses reached their maximum values near the weld zone, then dropped with the increasing distance from the weld zone and finally stabilized the zero value.
2. The simulation results are in good agreement with the experimental results along the A-B path, confirming the welding model accuracy
3. The UIT introduces a compressive residual stress layer with depth between 2 and 3 mm near the impacting surface of weld joint. The effect of the UIT decreased with depth.

Author details

Lanqing Tang¹, Ayhan Ince^{1,2*} and Jing Zheng¹

*Address all correspondence to: aince@purdue.edu

1 Purdue Polytechnic Institute, Purdue University, West Lafayette, IN, USA

2 Department of Mechanical, Industrial and Aerospace Engineering, Concordia University, Montreal, Quebec, Canada

References

- [1] Teng TL, Fung CP, Chang PH, Yang WC. Analysis of residual stresses and distortions in T-joint fillet welds. *International Journal of Pressure Vessels and Piping*. 2001;78:523-538. DOI: 10.1016/S0308-0161(01)00074-6
- [2] Weich I, Thomas U, Thomas N, Dilger K, Chalandar HE. Fatigue behavior of welded high-strength steels after high frequency mechanical post-weld treatments. *Weld World*. 2009;53:R322-R332. DOI: 10.1007/BF03263475

- [3] Abid M, Siddique M. Numerical simulation to study the effect of tack welds and root gap on welding deformations and residual stresses of a pipe-flange joint. *International Journal of Pressure Vessels and Piping*. 2005;**82**(11):860-871
- [4] Chang KH, Lee CH. Finite element analysis of the residual stresses in T-joint fillet welds made of similar and dissimilar steels. *International Journal of Advanced Manufacturing Technology*. 2009;**41**:250-258
- [5] Ferro P. The local strain energy density approach applied to pre-stressed components subjected to cyclic load. *Fatigue and Fracture of Engineering Materials and Structures*. 2014;**37**(11):1268-1280. DOI: 10.1111/ffe.12211
- [6] Ferro P, Berto F, James NM. Asymptotic residual stress distribution induced by multi-pass welding processes. *International Journal of Fatigue*. 2017;**101**:421-429
- [7] Rakesh R, Ghahremani K, Walbridge S, Ince A. Testing and fracture mechanics analysis of strength effects on the fatigue behavior of HFMI-treated welds. *Weld World*. 2016;**60**:987-999. DOI: 10.1007/s40194-016-0354-4
- [8] Marquis GB, Mikkola E, Yildirim HC, Barsoum Z. Fatigue strength improvement of steel structures by high-frequency mechanical impact: Proposed fatigue assessment guidelines. *Welding in the World*. 2013;**57**:803-822. DOI: 10.1007/s40194-016-0354
- [9] Statnikov ES. Applications of operational ultrasonic impact treatment (UIT) technologies in production of welded joints. *Welding in the World*. 2000;**44**:11-21
- [10] Deng D, Murakawa H. Numerical simulation of temperature field and residual stress in multi-pass welds in stainless steel pipe and comparison with experimental measurements. *Computational Materials Science*. 2006;**37**:269-277. DOI: 10.1016/j.commatsci.2005.07.007
- [11] Turski M, Clitheroe S, Evans AD, Rodopoulos C, Hughes DJ, Withers PJ. Engineering the residual stress state and microstructure of stainless steel with mechanical surface treatments. *Applied Physics A*. 2010;**99**:549-556. DOI: 10.1007/s00339-010-5672-6
- [12] Liu Q, Ge DJ, Chen FG, Zou JS. Residual stress variation in a thick welded joint after ultrasonic impact treatment. *Science and Technology of Welding and Joining*. 2016;**21**:634-631. DOI: 10.1080/13621718.2016.1149932
- [13] Foehrenbach J, Hardenecke V, Farajian M. High frequency mechanical impact treatment (HFMI) for the fatigue improvement: Numerical and experimental investigations to describe the condition in the surface layer. *Welding in the World*. 2016;**60**:749-755. DOI: 10.1007/s40194-016-0338-4
- [14] Dekhtyar AI, Mordiyuk BN, Savvakina DG, Bondarchuk VI, Moiseeva IV, Khripta NI. Enhanced fatigue behavior of powder metallurgy Ti-6Al-4V alloy by applying ultrasonic impact treatment. *Materials Science and Engineering: A*. 2015;**641**:348-359. DOI: 10.1016/j.msea.2015.06.072

- [15] Guo CB, Wang ZJ, Wang DP. Numerical analysis of the residual stress in ultrasonic impact treatment process with single-impact and two-impact models. *Applied Surface Science*. 2015;**347**:596-601. DOI: 10.1016/j.apsusc.2015.04.128
- [16] Mordyuka BN, Iefimovb MO, Prokopenkoa GI, Goluba TV, Danylenkob MI. Structure, microhardness and damping characteristics of Al matrix composite reinforced with AlCuFe or Ti using ultrasonic impact peening. *Surface and Coatings Technology*. 2010;**204**:1590-1598. DOI: 10.1016/j.surfcoat.2009.10.009
- [17] Muránskya O, Hamelina CJ, Smithb MC, Bendeicha PJ, Edwardsa L. The effect of plasticity theory on predicted residual stress fields in numerical weld analyses. *Computational Materials Science*. 2012;**154**:125-134. DOI: 10.1016/j.commatsci.2011.10.026
- [18] Le Pécheura A, Curtitb F, Clavela M, Stephanb JM, Reya C, Bomparda P. Thermo-mechanical FE model with memory effect for 304L austenitic stainless steel presenting microstructure gradient. *International Journal of Fatigue*. 2012;**45**:106-115. DOI: 10.1016/j.ijfatigue.2012.05.016
- [19] Mahmoudi AH, Pezeshki-Najafabadi SM, Badnava H. Parameter determination of Chaboche kinematic hardening model using a multi objective Genetic Algorithm. *Computational Materials Science*. 2011;**50**:1114-1122. DOI: 10.1016/j.commatsci.2010.11.010
- [20] Chaboche JL. A review of some plasticity and viscoplasticity constitutive theories. *International Journal of Plasticity*. 2008;**24**:1642-1693. DOI: 10.1016/j.ijplas.2008.03.009
- [21] Yang XJ, Zhou JX, Ling X. Study on plastic damage of AISI 304 stainless steel induced by ultrasonic impact treatment. *Materials & Design*. 2012;**36**:477-481. DOI: 10.1016/j.matdes.2011.11.023
- [22] Yuan KL. Modelling of ultrasonic impact treatment (UIT) of welded joints and its effect on fatigue strength. *Frattura ed Integrità Strutturale*. 2015;**34**:476-486. DOI: 10.3221/IGF-ESIS.34.53
- [23] Zheng H, Liu DF, Lee CF, Tham LG. Displacement-controlled method and its applications to material non-linearity. *International Journal for Numerical and Analytical Methods in Geomechanics*. 2005;**29**:209-226. DOI: 10.1002/nag.410
- [24] Tang LQ, Li HF, Wang XX, Qian CF. Numerical simulation and experimental investigation of residual stress in 06Cr19Ni10 austenitic stainless steel weld joint with effects of strain-strengthening. *Applied Mechanics and Materials*. 2017;**853**:204-208. DOI: 10.4028/www.scientific.net/AMM.853.204
- [25] Goldak J, Chakravarti A, Bibby M. A new finite element model for welding heat sources. *Metallurgical Transactions B*. 1984;**15**:299-305. DOI: 10.1007/BF02667333
- [26] Zheng J, Ince A. Numerical modeling and simulation of welding residual stresses using finite element method. In: 8th International Conference on Physical and Numerical Simulation of Materials Processing; 2016; Seattle, Washington

- [27] Liang W, Murakawa H, Deng D. Investigation of welding residual stress distribution in a thick-plate joint with an emphasis on the features near weld end-start. *Materials & Design*. 2015;**67**:303-312. DOI: 10.1016/j.matdes.2014.11.037
- [28] Smith DJ, Garwood SJ. Influence of postweld heat treatment on the variation of residual stresses in 50 mm thick welded ferritic steel plates. *International Journal of Pressure Vessels and Piping*. 1992;**51**:241-256. DOI: 10.1016/0308-0161(92)90083-R
- [29] Mitra A, Prasad NS, Ram GDJ. Estimation of residual stresses in an 800 mm thick steel submerged arc weldment. *Journal of Materials Processing Technology*. 2016;**229**:181-190. DOI: 10.1016/j.jmatprotec.2015.09.007
- [30] Xu JJ, Zhu ZQ, Chen LG, Ni CZ. Temperature distribution and residual stresses during multipass narrow gap welding of thick plates. *Materials Science and Technology*. 2006;**22**:232-237. DOI: 10.1179/174328406X83897
- [31] Ji SD, Fang HY, Liu XS, Meng QG. Influence of a welding sequence on the welding residual stress of a thick plate. *Modelling & Simulation in Materials Science & Engineering*. 2005;**13**:553-566. DOI: 10.1088/0965-0393/13/4/006
- [32] Roy S, Fisher JW, Yen BT. Fatigue resistance of welded details enhanced by ultrasonic impact treatment (UIT). *International Journal of Fatigue*. 2003;**25**:1239-1247. DOI: 10.1016/S0142-1123(03)00151-8
- [33] Yuan K, Sumi Y. Simulation of residual stress and fatigue strength of welded joints under the effects of ultrasonic impact treatment (UIT). *International Journal of Fatigue*. 2016;**92**:321-332. DOI: 10.1016/j.ijfatigue.2016.07.018
- [34] Liu Y, Wang DP, Deng CY, Xia LQ, Huo LH, Wang LJ, Gong BM. Influence of re-ultrasonic impact treatment on fatigue behaviors of S690QL welded joints. *International Journal of Fatigue*. 2014;**66**:155-160. DOI: 10.1016/j.ijfatigue.2014.03.024
- [35] Ghahremani K, Ranjan R, Walbridge S, Ince A. Fatigue strength improvement of aluminum and high strength steel welded structures using high frequency mechanical impact treatment. *Procedia Engineering*. 2015;**133**:465-476. DOI: 10.1016/j.proeng.2015.12.616
- [36] Ince A. A novel technique for multiaxial fatigue modelling of ground vehicle notched components. *International Journal of Vehicle Design*. 2015;**67**:294-313. DOI: 10.1504/IJVD.2015.069486
- [37] Ince A. A computational multiaxial model for stress-strain analysis of ground vehicle notched components. *SAE International Journal of Engines*. 2017;**10**:316-322. DOI: 10.4271/2017-01-0329
- [38] Ince A, Bang A. Deviatoric Neuber method for stress and strain analysis at notches under multiaxial loadings. *International Journal of Fatigue*. 2017;**102**:229-240. DOI: 10.1016/j.ijfatigue.2017.05.007

Rapid Calculation of Residual Notch Stress Intensity Factors (R-NSIFs) by Means of the Peak Stress Method

Marco Colussi, Paolo Ferro, Filippo Berto and
Giovanni Meneghetti

Additional information is available at the end of the chapter

<http://dx.doi.org/10.5772/intechopen.73514>

Abstract

The intensity of the residual singular stress distribution can be quantified by the residual notch stress intensity factor (R-NSIF), which might be a useful stress parameter to include in local approaches for fatigue strength assessments of welded joints. In order to calculate the residual stress fields by means of welding process simulations, the mesh adopted in numerical models has necessarily to be very fine. Unfortunately, the nonlinear and transient behavior of the welding simulation makes numerical analyses extremely demanding in terms of computational time, particularly, if large welded structures and/or multipass welds have to be simulated. In this scenario, the use of methods aimed at reducing the computational effort to estimate local stresses and strains in welded structures can be effective. Among these, the peak stress method has been proposed to estimate the notch stress intensity factors (NSIFs) at sharp V-notches, using coarse finite element patterns. In this work, the peak stress method (PSM) has been used to calculate the R-NSIF of a full penetration welded T-joint. It has been shown that the PSM can successfully be used to estimate R-NSIFs values, provided that the stress redistribution induced by plasticity in the zone very close to the notch tip is negligible.

Keywords: residual notch stress intensity factor, residual stress, peak stress method, finite element analysis, coarse mesh

1. Introduction

Residual stresses are induced on fusion-welded joints as a consequence of thermal gradients and nonuniform plastic deformations during the cooling phase. According to clamping conditions, process parameters and kind of alloys to be welded, they can be negative or positive. Positive, or tensile residual stresses, are known to be detrimental for the high cycle fatigue strength joints [1, 2], whereas their effect on low cycle fatigue resistance is found negligible or null, as well. This is because the higher the stress amplitude, the higher the extension of plastic deformation in the fatigue crack initiation sites (weld toe or weld root) that cancels the preexisting residual stress state. On the other hand, negative residual stresses induced by fusion welding have been found to increase the fatigue strength of joints [3] and thus are considered beneficial for the joint itself. Residual stress effect on fatigue strength of welded components is implicitly taken into account by design fatigue curves obtained from experimental data generated by testing welded joints prepared with different process parameters. Despite this current methodology, new design approaches that take into account residual stress explicitly were published in recent literature [4–8]. Hensel et al. proposed a method that replaces the nominal stress ratio with the effective stress ratio to describe the combined effect of mean and residual stresses. Ferro [4], on the other hand, suggested the use of the strain energy density (SED) approach [9] to quantify the residual stress effect on fatigue strength of welded joints through the assessment of residual notch stress intensity factors (R-NSIFs). The analysis of residual stress distribution has been a challenging task since many years. The *a posteriori* assessment of residual stress can be performed by experimental techniques, though they are time-consuming and expensive and provide data at single points (in most cases at the surface) of the joint. *A priori* residual stress determination can be obtained by numerical models, yet they need to be validated. Welding simulations are very complex because fluid dynamics, metallurgical, thermal and mechanical phenomena interact with each other [10]. When residual stress and strain are the major goals of the simulation, fluid dynamics of welding pool is almost always not taken into account. In these cases, the fusion zone is modeled by power density distribution functions whose shape and dimensions depend on welding technology (laser welding, arc welding and so on) and process parameters, respectively. Furthermore, the analysis is transient and nonlinear [11]. Numerical models require high mesh densities in order to capture the severe thermal gradient induced by the welding source. Moreover, in real components, multipass welding is often adopted. Promising approaches are already present in literature, but not yet extensively validated. In the ‘macroweld deposit approach’, the heat is applied in a welding instantaneously, without using a power source. The macrosteps number is chosen a priori based on the experience and real welding speed. The higher the welding speed, the longer is the single macrostep. The heat transferred into the structure is the same as in the real process, but it occurs in another time frame. In contrast to the macroweld deposit methodology, with the local-global method, the welding simulation is carried out on a refined local model (LM), whose geometry is extracted from the global structure (GS). The nodal displacements coming from LM solution are applied to the GS and a linear elastic computation is finally performed to assess the global distortion. The mesh can be locally refined and the refined zone follows the welding source by saving

computational time. Models with coupled 3D and shell elements are also used to simplify the analysis. The bead is modeled with 3D elements, while the plates are modeled with shell elements. Finally, a 2D model can also be used to simplify the simulation. In this case, the welding source is thought to pass across the modeled cross section and melting the alloy. Stress and strain are computed under generalized plain strain condition. In previous works, it has been demonstrated that if the weld toe is modeled as a sharp, zero radius, V-shaped notch, residual stress field near that zone is singular [12–14] and its sign depends on both clamping conditions and metallurgical characteristics of the alloy to be welded [13, 14]. This outcome of numerical simulations allows to treat the asymptotic residual stress field like the load-induced singular stress field by means of the R-NSIF (residual-notch stress intensity factor), i.e., a stress field parameter able to quantify the intensity of the residual stresses near the weld toe. Because, direct R-NSIF calculation from asymptotic local stress fields requires very fine meshes, new strategies are needed to speed up numerical analysis. In this context, the peak stress method (PSM) has been proved to be suitable for the notch stress intensity factors (NSIFs) calculation by means of coarse meshes [15]. Therefore, in the present work, the use of the PSM is validated also for the R-NSIFs assessment.

2. Analytical background of the peak stress method

The peak stress method (PSM) is an engineering, FE-based method to estimate the notch stress intensity factors (NSIFs) at the weld toe and at the weld root of welded joints. The basic idea is to use very coarse meshes, if compared with those required to evaluate directly the asymptotic stress distributions required to apply the NSIFs definitions. The second peculiarity of the method is that the sole linear elastic peak stress evaluated at the sharp V-notch tip is necessary and sufficient to estimate the NSIF: therefore, the singular stress fields do not need to be postprocessed according to the NSIFs definitions (Eqs. (1) and (2)). Both these features of the method make it useful in practical applications.

In plane problems, the local linear elastic stress fields close to the tip of sharp V-notches, like those shown in the welded joint of **Figure 1**, can be expressed as functions of the relevant NSIFs, which quantify the magnitude of the asymptotic singular stress distributions. The asymptotic, singular stress distributions ahead of sharp V-notches under mode I (opening) and mode II (sliding) loadings have been determined by Williams [16]. The mode I and mode II NSIFs can be defined according to Gross and Mendelson [17] by means of Eqs. (1) and (2), respectively.

$$K_1 = \sqrt{2\pi} \cdot \lim_{r \rightarrow 0} [(\sigma_{\theta\theta})_{\theta=\theta} \cdot r^{1-\lambda_1}] \quad (1)$$

$$K_2 = \sqrt{2\pi} \cdot \lim_{r \rightarrow 0} [(\tau_{r\theta})_{\theta=\theta} \cdot r^{1-\lambda_2}] \quad (2)$$

The stress singularity exponents λ_1 and λ_2 depend on the notch opening angle 2α [16] and are reported in **Table 1**. The stress components $\sigma_{\theta\theta}$ and $\tau_{r\theta}$ are calculated along the direction $\theta = 0$, i.e., the notch bisector (see **Figure 1**).

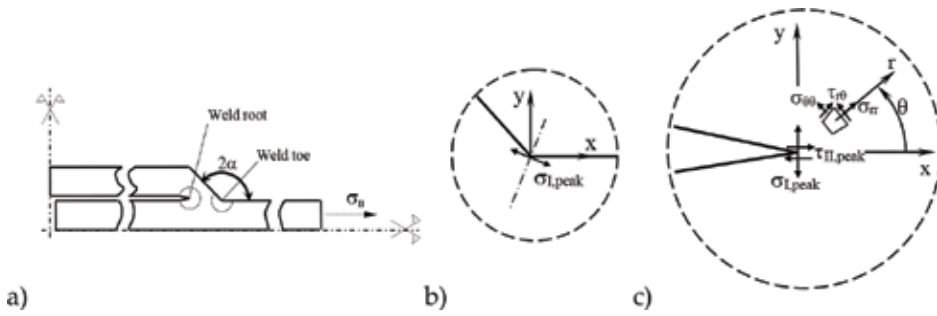


Figure 1. Sharp V-shaped notches in a welded joint (a) at the toe (2α typically equal to 135°) (b) and at the root ($2\alpha = 0^\circ$) (c) sides. Definition of peak stresses $\sigma_{I,peak}$ and $\tau_{II,peak}$ evaluated at the weld toe and the weld root by means of a linear elastic finite element analysis.

2α (deg)	λ_1	λ_2
0	0.500	0.500
90	0.544	0.909
135	0.674	

Table 1. Values of the stress singularity exponents λ_1 and λ_2 .

Notch stress intensity factors (NSIFs) proved to correlate the static strength of components made of brittle or quasi-brittle materials and weakened by sharp V-notches [18–23], as well as the medium and high-cycle fatigue strength of notched components made of structural materials [24, 25]. Concerning welded joints, NSIFs have been used to analyze the fatigue strength both under uniaxial [26–30] and multiaxial cyclic loadings [31]. However, to apply the NSIF approach by means of finite element (FE) analyses in engineering problems, a major drawback arises, because of the very refined FE meshes needed to evaluate the NSIFs on the basis of the definitions reported in Eqs. (1) and (2). In the case of three-dimensional components, the numerical analyses are even more time-consuming.

Recently, a simplified and rapid technique, the so-called peak stress method (PSM), has been proposed in order to speed up the numerical evaluation of the NSIFs by adopting FE models with coarse meshes. Inspired by previous contributions by Nisitani and Teranishi [32, 33] to rapidly estimate the mode I SIF of cracks, the PSM has been theoretically justified and extended to estimate also the mode I NSIF of pointed V-notches [34, 35]; subsequently, it has been formulated for the mode II SIF of cracks [36] and the mode III NSIF of pointed V-notches [37].

Essentially, the PSM allows to rapidly estimate the NSIFs K_1 and K_2 (Eqs. (1) and (2)) from the singular, linear elastic, opening (mode I) and sliding (mode II) FE peak stresses $\sigma_{I,peak}$ and $\tau_{II,peak}$ respectively, which are calculated at the node located at the V-notch tip (see **Figure 1**) by means of an FE analysis in which the following parameters are calibrated:

- the adopted FE code;
- the element type and formulation;

- the FE mesh pattern;
- the criteria for stress extrapolation at FE nodes.

In more detail, the expressions of the PSM are the following [34, 36]:

$$K_1 \cong K_{FE}^* \cdot \sigma_{I,peak} \cdot d^{1-\lambda_1} \quad (3)$$

$$K_2 \cong K_{FE}^* \cdot \tau_{II,peak} \cdot d^{0.5} \quad (4)$$

In previous expressions, d is the so-called global element size parameter to input in the FE software, i.e., the mean size of the finite elements adopted by the free mesh generation algorithm available in the numerical code, while K_{FE}^* and K_{FE}^{**} take into account all calibration parameters mentioned previously.

With reference to plane models, the PSM has been calibrated [34, 36] under the following conditions:

- Adopted FE code: Ansys
- Element types (element library of Ansys code):
 - Two-dimensional, 4-node quadrilateral finite elements with linear shape functions (PLANE 42 or alternatively PLANE 182 with K-option 1 set to 3, i.e., 'simple enhanced strain' formulation activated).
 - Three-dimensional, eight-node brick elements (SOLID 45 or equivalently SOLID 185 with K-option 2 set to 3, i.e., 'simple enhanced strain' option activated).
 - Two-dimensional, harmonic, 4-node linear quadrilateral elements, to analyze axis-symmetric components subjected to external loads that can be expressed according to a Fourier series expansion (PLANE 25).
- There is a standard mesh pattern close to the V-notch or crack tip that is reported in **Figure 2** [34, 36], where it is seen that four elements share the node located at the notch tip if the notch opening angle 2α is equal to or lower than 90° ; conversely, if the notch opening angle is $2\alpha > 90^\circ$, then two elements share the node at notch tip. **Figure 2** shows examples of such mesh patterns in case of symmetric FE models. It should be noted that the mesh patterns according to the PSM are automatically generated by the *free-mesh generation algorithm* of Ansys code, after having input the average FE size d by means of the command 'global element size' available in the software. There are not additional parameters or special settings to input in order to generate the mesh.
- Eq. (3) can be applied to sharp V-notches with an opening angle 2α between 0° and 135° ; while calibration for mode II loading, Eq. (4), is restricted to the crack case ($2\alpha = 0$, $(1 - \lambda_2) = 0.5$).

Under these conditions, the following values have been calibrated: $K_{FE}^* \cong 1.38$ and $K_{FE}^{**} \cong 3.38$. To apply expressions (3) and (4) with $K_{FE}^* = 1.38$ and $K_{FE}^{**} = 3.38$, the average element size d can be chosen arbitrarily, but within a range of applicability defined in the relevant literature

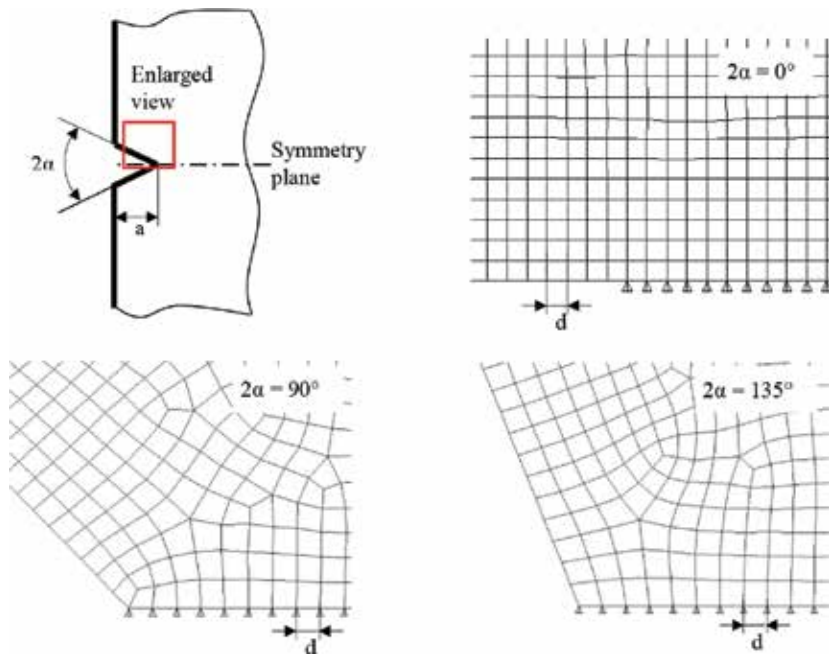


Figure 2. Mesh patterns according to the PSM [34, 36]. Symmetry boundary conditions are applied to the FE model.

[34, 36]: for mode I loading (Eq. (3)), the mesh density ratio a/d that can be adopted in FE analyses must exceed 3 to obtain $K_{FE}^* = 1.38 \pm 3\%$; in case of mode II loading (Eq. (4)), more refined meshes are needed, the mesh density ratio a/d having to be greater than 14 to obtain $K_{FE}^{**} = 3.38 \pm 3\%$. In previous expressions, a is the characteristic size of the analyzed sharp V-notch, i.e., the notch depth in **Figure 2**. In case of welded T-joints analyzed at the weld toe side, a is the main plate thickness ($a = 6$ mm in next **Figure 3**).

Any structural strength assessment criterion, which is based on NSIF parameters, could be reformulated by using the PSM by means of Eqs. (3) and (4). In the recent literature, the PSM has been coupled to the averaged strain energy density (SED) criterion to assess the fatigue strength of welded joints subjected to axial [15, 36, 38, 39], torsion [37, 40] and multiaxial [41, 42] loading conditions.

3. R-NSIFs evaluation by using the peak stress method

The PSM has been recently calibrated in Sysweld[®] finite element environment, to rapidly evaluate the linear elastic notch stress intensity factor (NSIF) under mode I loading [43]. According to such calibration, the mode I NSIF is proportional to a constant K_{FE}^* , which is equal to 1.64 in case of V-notches with opening angle ranging from 90° to 135° and equal to 1.90 in case of cracks (0° opening angle). Provided that the mesh density ratio is equal to or greater than 4, all FE results fall within a scatter band of $\pm 5\%$, regardless of the V-notch depth.

The aim of this section is to show the procedure of R-NSIFs evaluation through the PSM with a practical application. With this purpose, a full penetration welded T-joint has been analyzed using the finite element code Sysweld[®]. Generalized plane strain condition has been assumed, this choice being appropriate to describe the out-of-plane stress values in 2D cross section model of welding process [44]. The welded joint geometry and the assumed dimensions are shown in **Figure 3**.

According to the PSM hypothesis, the weld toe has been modeled as a sharp, zero radius, V-shaped notch. The notch opening angle 2α has been chosen equal to 135° . It has been assumed carbon steel with chemical composition according to the Standard ASTM SA 516 (Grade 65 resp. 70) and the corresponding thermomechanical properties have been taken from Sysweld[®] database. Thermometallurgical and mechanical properties as a function of phase and temperature have been taken into account (Sysweld Toolbox 2011). In the metallurgical analysis, the following phases have been included: martensite, bainite, and ferrite-pearlite. The metallurgical transformations mainly depend on thermal history, according to the continuous cooling transformation (CCT) diagrams, which plot the start and the end transformation temperatures as a function of cooling rate or cooling time. In the present work, the diffusion-controlled phase transformations and the displacive martensitic transformation have been modeled according to Leblond and Devaux [45] and to Koistinen and Marburger [46] kinetic law, respectively. Radiative and convective heat losses have been applied at the boundary (external surfaces) of the plates to be joined—the former by using the Stefan-Boltzman law and the latter by using a convective heat transfer coefficient equal to $25 \text{ W/m}^2 \text{ K}$. The thermal gradient in the out-of-plane direction cannot be taken into account in a 2D cross section model because of its intrinsic formulation. However, it is supposed that the higher the welding speed, the lower the out-of-plane thermal gradient. The thermal history at nodes of the numerical model is the only load applied in welding simulation. Such thermal load is simulated by means of a power density distribution function whose shape depends on welding technology. In this work, the heat source has been modeled using a double ellipsoid power density distribution function [47] described by Eq. (5), which has been widely used in literature for arc welding simulation [10].

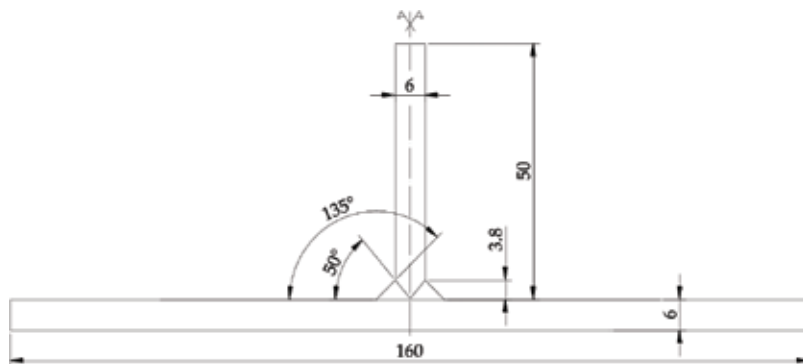


Figure 3. Schematic representation of the T-joint. Dimensions are in mm.

$$q(x, y, t) = \frac{6\sqrt{3} f_{1,2} Q}{\pi\sqrt{\pi} a_0 b_0 c_{1,2}} e^{-\frac{3x^2}{a_0^2}} e^{-\frac{3y^2}{b_0^2}} e^{-\frac{3|z|(\tau-t)^2}{c_{1,2}^2}} \tag{5}$$

The double ellipsoid heat source and the meaning of the symbols used in Eq. (5) are shown in **Figure 4**, whereas the adopted numerical values are summarized in **Table 2**. The power density provided by Eq. (5) has the unit W/m³.

By taking advantage on the symmetry, one-half of the joint has been modeled. In **Table 3**, the very refined mesh pattern used in the calculation of R-NSIF from the local stress field and the

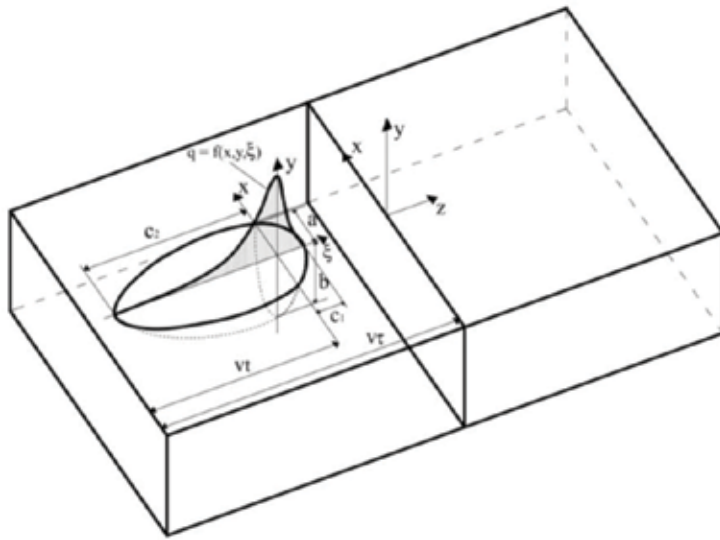


Figure 4. Schematic of Goldak’s heat source with symbols taken from the original paper [45].

Q^*	Power input [W]	11,500
η	Efficiency	0.64
Q	Absorbed power [W]	$\eta \cdot Q^*$
a_0	Molten pool dimensions [mm]	3.5
b_0		11
c_1		2.3
c_2		7.9
f_1	Fractions of heat deposit in the front and rear quadrants, with $f_1 + f_2 = 2$	0.6
f_2	(subscript 1 for $\xi > 0$; subscript 2 for $\xi < 0$)	1.4
v	Welding speed [mm/s]	11
τ	Total time before the welding torch is over the transverse cross section [s]	3

Table 2. Goldak’s source parameters adopted in the present analysis.


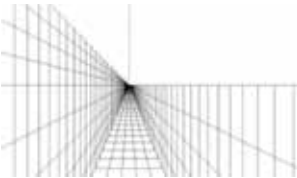

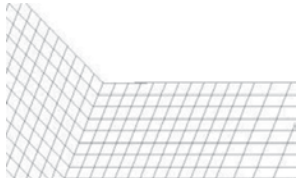
Method	Global FEM model	Detail of mesh refinement near the weld toe	R-NSIF value [MPa mm ^{0.326}]	N° of FE in model	Δ %
Local stress filed calculation			52.4	2500	—
PSM			52.9	1350	0.9

Table 3. Finite element meshes used to directly compute the R-NSIF from local stress and to estimate it by using the PSM.

typical free-generated mesh pattern according to the PSM evaluation are compared. The FE model used to compute R-NSIFs from local stress fields had a minimum element size at the notch tip equal to about 5×10^{-5} mm, according to the literature [27].

The FE models used to estimate the R-NSIFs by means of the PSM were generated by using a mesh pattern as similar as possible to the standard PSM shown in **Figure 2**, according to the PSM calibration rules for Sysweld[®] finite element code listed in the previous section. The mesh generation algorithm provided by visual mesh has been adopted. Four-node 2004 quadrilateral elements from Sysweld library have been used and the numerical integration scheme was set to 2×2 Gauss points. The average finite element size d imposed to the mesh generation algorithm is 0.29 mm, which translates into a mesh density ratio a/d equal to 10. Such FE size was necessary to obtain a temperature field in agreement with that obtained with the very refined mesh pattern. More precisely, to establish the appropriate d value, a difference in nodal temperatures of few percentage points was allowed between the very refined and the PSM coarse meshes. Uncoupled thermomechanical analyses were carried out, where the molten effect was simulated by using a specific function implemented in Sysweld code that cancels the history of an element if its temperature exceeds the melting temperature. Welded plates have been supposed free of restraints, except for the symmetry boundary condition.

4. Results and discussion

The asymptotic nature of the residual stress distribution near a sharp V-notch has been numerically investigated by using Sysweld[®]. **Figure 5** shows the temperature distribution when the melted zone has reached its maximum extension. It has been found that the stress

distribution near the weld toe is linear in a log-log plot (Figure 6) and its slope is equal to 0.326, which corresponds to the analytical solution for open V-notches with zero radius. The intensity of such residual stress field can therefore be given in terms of R-NSIFs.

Concerning the PSM, a peak stress value equal to 48.3 MPa was calculated at the node located at the weld toe. A mesh pattern having element size equal to 0.29 mm was adopted near the weld toe, which corresponds to a mesh density ratio $a/d = 10 \geq 4$, according to the PSM calibration in Sysweld® [43]. Results are summarized in Table 3, where it is possible to notice a good agreement between the K_1 value obtained from the local stress field computed with a very fine mesh and the one estimated by means of the coarse PSM mesh. In the latter case, the PSM calibration constant for $K_{FE}^* = 1.64$, valid for Sysweld®, has been used.

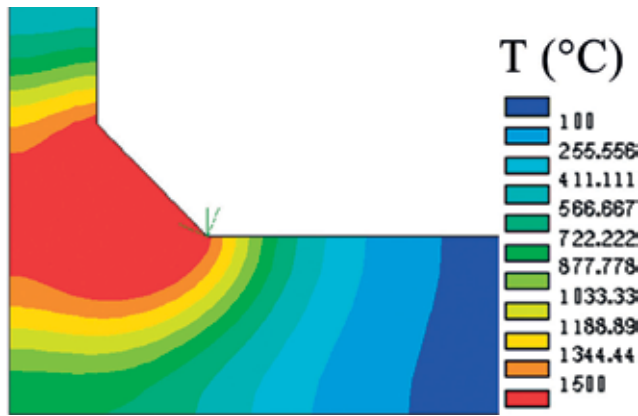


Figure 5. Temperature distribution at the instant of maximum width of the fusion zone (in red).

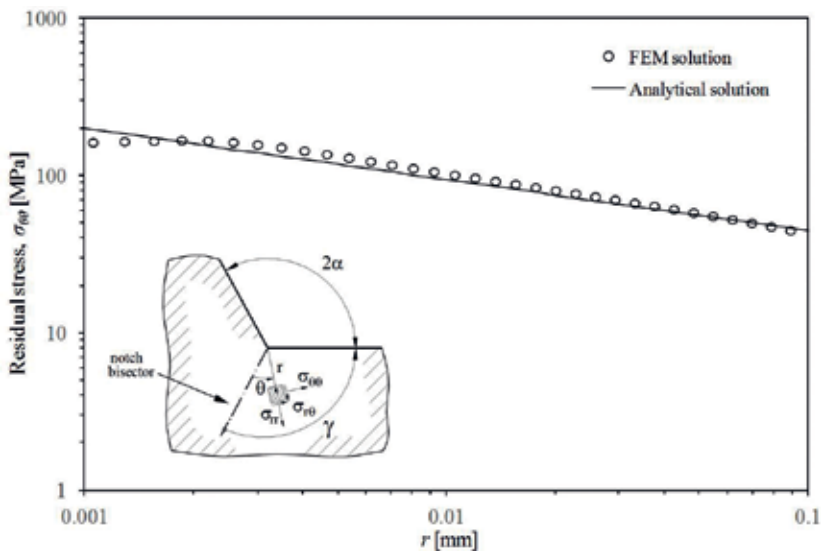


Figure 6. Asymptotic $\sigma_{\theta\theta}$ component of the residual stress field near the notch tip along the notch bisector, i.e., $\theta = 0^\circ$.

This investigation confirms that the PSM can be used for a rapid, engineering R-NSIF evaluation. To illustrate the advantage of the PSM, the solution time associated to the very refined meshes was about 1 min for thermal analyses and 4 min for mechanical analyses, whereas the PSM required few seconds for thermal analyses and a minute for mechanical analyses. Moreover, the following main advantages can be exploited if the R-NSIFs are estimated by means of the PSM rather than directly computed from local stress fields: (a) only one nodal stress value calculated at the point of singularity is sufficient to compute the R-NSIF, the whole stress distribution along the notch bisector being no longer required; (b) four orders of magnitude coarser meshes could be employed by using the PSM, as compared to the very refined meshes required to evaluate the local stress field directly. In the authors' opinion, both reasons make the PSM of easy and fast applicability in industrial and research applications. Finally, the PSM appears also suitable, with further developments and investigation, for the R-NSIF value calculation by using three-dimensional FE models of welding process.

5. Conclusions

In the present contribution, a practical application of the PSM in the residual notch stress intensity factor (R-NSIF) estimation on a full penetration welded T-joint has been given. It has been found that, provided that the stress redistribution induced by plasticity in the zone very close to the notch tip is negligible, the PSM allows the rapid, coarse mesh-based, estimation of the R-NSIF. This result is promising because, in principle, R-NSIFs may be useful parameters to include the residual stress effect in fatigue strength assessments of welded joints.

Author details

Marco Colussi¹, Paolo Ferro¹, Filippo Berto² and Giovanni Meneghetti^{3*}

*Address all correspondence to: giovanni.meneghetti@unipd.it

1 Department of Engineering and Management, University of Padova, Vicenza, Italy

2 Department of Industrial and Mechanical Engineering, Norwegian University of Science and Technology, Trondheim, Norway

3 Department of Industrial Engineering, University of Padova, Padova, Italy

References

- [1] Livieri P, Lazzarin P. Fatigue strength of steel and aluminium welded joints based on generalised stress intensity factors and local strain energy values. *International Journal of Fracture*. 2005;133:247-278

- [2] Gurney TR. *The Fatigue Strength of Transverse Fillet Welded Joints*. Cambridge: Abington Publishing; 1991
- [3] Bertini L, Fontanari V, Straffellini G. Influence of post weld treatments on fatigue behaviour of Al-alloy welded joints. *International Journal of Fatigue*. 1998;**20**:749-755
- [4] Ferro P. The local strain energy density approach applied to pre-stressed components subjected to cyclic load. *Fatigue and Fracture of Engineering Materials and Structures*. 2014;**37**:1268-1280
- [5] Ferro P, Berto F, James MN, Borsato T. Review of recent advances in local approaches applied to pre-stressed components under fatigue loading. In: Iacoviello F, Susmel L, Firrao D, Ferro G, editors. *21st European Conference on Fracture*; 20–24 June 2016; Catania. Elsevier; 2016
- [6] Ferro P, Berto F, James NM. Asymptotic residual stresses in butt-welded joints under fatigue loading. *Theoretical and Applied Fracture Mechanics*. 2016;**83**:114-124
- [7] Ferro P, Berto F. Quantification of the influence of residual stresses on fatigue strength of Al-alloy welded joints by means of the local strain density approach. *Strength of Materials*. 2016;**48**:426-436
- [8] Hansel J, Nitschke-Pagel T, Dilger K. Engineering model for the quantitative consideration of residual stresses in fatigue design of welded components. *Welding in the World*. 2017;**61**:997-1002
- [9] Lazzarin P, Zambardi R. A finite-volume-energy based approach to predict the static and fatigue behavior of components with sharp V-shaped notches. *International Journal of Fatigue*. 2001;**112**:275-298
- [10] Ferro P, Bonollo F, Tiziani A. Methodologies and experimental validations of welding process numerical simulation. *International Journal of Computational Materials Science and Surface Engineering*. 2010;**3**:114-132
- [11] Ferro P. Molten pool in welding processes: Phenomenological vs fluid-dynamic numerical simulation approach. In: Arnberg L, Bonollo F, Montanari R, editors. *Liquid Metals and Alloys: From Structure to Industrial Applications*. Switzerland: Trans Tech Publications Ltd; 2017
- [12] Ferro P, Berto F, Lazzarin P. Generalized stress intensity factors due to steady and transient thermal loads with applications to welded joints. *Fatigue and Fracture of Engineering Materials and Structures*. 2006;**29**:440-453
- [13] Ferro P, Petrone N. Asymptotic thermal and residual stress distributions due to transient thermal loads. *Fatigue and Fracture of Engineering Materials and Structures*. 2009;**32**:936-948
- [14] Ferro P. The influence of phase transformations on the asymptotic residual stress distribution arising near a sharp V-notch tip. *Modelling and Simulation in Materials Science and Engineering*. 2012;**20**:085003

- [15] Meneghetti G, Lazzarin P. The peak stress method for fatigue strength assessment of welded joints with weld toe or weld root failures. *Welding in the World*. 2011;**55**:22-29
- [16] Williams ML. Stress singularities resulting from various boundary conditions in angular corners of plates in tension. *Journal of Applied Mechanics*. 1952;**19**:526-528
- [17] Gross B, Mendelson A. Plane elastostatic analysis of V-notched plates. *International Journal of Fracture Mechanics*. 1972;**8**:267-276
- [18] Seweryn A. Brittle fracture criterion for structures with sharp notches. *Engineering Fracture Mechanics*. 1994;**47**:673-681
- [19] Nui LS, Chehimi C, Pluvinage G. Stress field near a large blunted tip V-notch and application of the concept of the critical notch stress intensity factor (NSIF) to the fracture toughness of very brittle materials. *Engineering Fracture Mechanics*. 1994;**49**:325-335
- [20] Fett T. Failure of brittle materials near stress singularities. *Engineering Fracture Mechanics*. 1996;**53**:511-518
- [21] Dunn ML, Suwito W, Cunningham S, May CW. Fracture initiation at sharp notches under mode I, mode II, and mild mixed mode loading. *International Journal of Fracture*. 1997;**84**:367-381
- [22] Gómez FJ, Elices M. A fracture criterion for sharp V-notched samples. *International Journal of Fracture*. 2003;**123**:163-175
- [23] Planas J, Elices M, Guinea G, Gómez F, Cendón D, Arbilla I. Generalizations and specializations of cohesive crack models. *Engineering Fracture Mechanics*. 2003;**70**:1759-1776
- [24] Kihara S, Yoshii A. A strength evaluation method of a sharply notched structure by a new parameter, The equivalent stress intensity factor. *JSME International Journal Series A Solid Mechanics and Material Engineering*. 1991;**34**:70-75
- [25] Boukharouba T, Tamine T, Niu L, Chehimi C, Pluvinage G. The use of notch stress intensity factor as a fatigue crack initiation parameter. *Engineering Fracture Mechanics*. 1995;**52**:503-512
- [26] Verreman Y, Nie B. Early development of fatigue cracking at manual fillet welds. *Fatigue and Fracture of Engineering Materials and Structures*. 1996;**19**:669-681
- [27] Lazzarin P, Tovo R. A notch intensity factor approach to the stress analysis of welds. *Fatigue and Fracture of Engineering Materials and Structures*. 1998;**21**:1089-1103
- [28] Lazzarin P, Livieri P. Notch stress intensity factors and fatigue strength of aluminium and steel welded joints. *International Journal of Fatigue*. 2001;**23**:225-232
- [29] Atzori B, Meneghetti G. Fatigue strength of fillet welded structural steels: Finite elements, strain gauges and reality. *International Journal of Fatigue*. 2001;**23**:713-721
- [30] Lazzarin P, Lassen T, Livieri P. A notch stress intensity approach applied to fatigue life predictions of welded joints with different local toe geometry. *Fatigue and Fracture of Engineering Materials and Structures*. 2003;**26**:49-58

- [31] Lazzarin P, Sonsino CM, Zambardi R. A notch stress intensity approach to assess the multiaxial fatigue strength of welded tube-to-flange joints subjected to combined loadings. *Fatigue and Fracture of Engineering Materials and Structures*. 2004;**27**:127-140
- [32] Nisitani H, Teranishi T. KI value of a circumferential crack emanating from an ellipsoidal cavity obtained by the crack tip stress method in FEM. In: Guagliano M, Aliabadi MH, editors. *Proceedings of 2nd International Conference on Fracture and Damage Mechanics*; 2001
- [33] Nisitani H, Teranishi T. KI of a circumferential crack emanating from an ellipsoidal cavity obtained by the crack tip stress method in FEM. *Engineering Fracture Mechanics*. 2004;**71**: 579-585
- [34] Meneghetti G, Lazzarin P. Significance of the elastic peak stress evaluated by FE analyses at the point of singularity of sharp V-notched components. *Fatigue and Fracture of Engineering Materials and Structures*. 2007;**30**:95-106
- [35] Meneghetti G, Guzzella C. The peak stress method to estimate the mode I notch stress intensity factor in welded joints using three-dimensional finite element models. *Engineering Fracture Mechanics*. 2014;**115**:154-171
- [36] Meneghetti G. The use of peak stresses for fatigue strength assessments of welded lap joints and cover plates with toe and root failures. *Engineering Fracture Mechanics*. 2012; **89**:40-51
- [37] Meneghetti G. The peak stress method for fatigue strength assessment of tube-to-flange welded joints under torsion loading. *Welding in the World*. 2013;**57**:265-275
- [38] Meneghetti G, Campagnolo A, Berto F. Fatigue strength assessment of partial and full-penetration steel and aluminium butt-welded joints according to the peak stress method. *Fatigue and Fracture of Engineering Materials and Structures*. 2015;**38**:1419-1431
- [39] Meneghetti G, Guzzella C, Atzori B. The peak stress method combined with 3D finite element models for fatigue assessment of toe and root cracking in steel welded joints subjected to axial or bending loading. *Fatigue and Fracture of Engineering Materials and Structures*. 2014;**37**:722-739
- [40] Meneghetti G, De Marchi A, Campagnolo A. Assessment of root failures in tube-to-flange steel welded joints under torsional loading according to the peak stress method. *Theoretical and Applied Fracture Mechanics*. 2016;**83**:19-30
- [41] Meneghetti G, Campagnolo A, Rigon D. Multiaxial fatigue strength assessment of welded joints using the peak stress method—Part I: Approach and application to aluminium joints. *International Journal of Fatigue*. 2017;**101**:328-342
- [42] Meneghetti G, Campagnolo A, Rigon D. Multiaxial fatigue strength assessment of welded joints using the peak stress method—Part II: Application to structural steel joints. *International Journal of Fatigue*. 2017;**101**:343-362

- [43] Colussi M, Ferro P, Berto F, Meneghetti G. The peak stress method to calculate residual notch stress intensity factors in welded joints. *Fatigue and Fracture of Engineering Materials and Structures*. DOI: 10.1111/ffe.12757 (Published online)
- [44] Feng Z. *Processes and Mechanisms of Welding Residual Stress and Distortion*. New York: Woodhead Publishing; 2005
- [45] Leblond JB, Devaux J. A new kinetic model for anisothermal metallurgical transformations in steels including effect of austenite grain size. *Acta Metallurgica*. 1984;**32**:137-146
- [46] Koistinen DP, Marburger RE. A general equation prescribing extent of austenite-martensite transformation in pure iron-carbon alloys and carbon steels. *Acta Metallurgica*. 1959;**7**:59-68
- [47] Goldak J, Chakravarti A, Bibby M. A new finite element model for welding heat sources. *Metallurgical Transactions B*. 1984;**15**:299-305

Edited by Paolo Ferro and Filippo Berto

The ability to quantify residual stresses induced by welding processes through experimentation or numerical simulation has become, today more than ever, of strategic importance in the context of their application to advanced design. This is an ongoing challenge that commenced many years ago. Recent design criteria endeavour to quantify the effect of residual stresses on fatigue strength of welded joints to allow a more efficient use of materials and a greater reliability of welded structures. The aim of the present book is contributing to these aspects of design through a collection of case-studies that illustrate both standard and advanced experimental and numerical methodologies used to assess the residual stress field in welded joints. The work is intended to be of assistance to designers, industrial engineers and academics who want to deepen their knowledge of this challenging topic.

Published in London, UK

© 2018 IntechOpen
© Tanantornanutra / iStock

IntechOpen

